UNIVERSITY OF CALIFORNIA, SAN DIEGO

Modeling of Seismic Anisotropy Near The Hawaiian Mantle Plume

A thesis submitted in partial satisfaction of the
requirements for the degree
Master of Science

in

Earth Sciences

by

Chenghao Shen

Committee in charge:

Professor Gabi Laske, Chair
Professor David T. Sandwell
Professor Peter M. Shearer

2017

The thesis of Chenghao Shen is approved, and it is acceptable in quality and form for publication on microfilm and electronically:

_____

_____

_____

Chair

University of California, San Diego

2017

DEDICATION

This thesis is dedicated to my advisor, Gabi Laske, who offers great help in my research. She encourages me and helps me get through my 2-year study at Scripps.

The thesis is also dedicated to all of my friends here and to my parents who support me.

TABLE OF CONTENTS

LIST OF FIGURES

LIST OF TABLES

ABSTRACT OF THE THESIS

Modeling of Seismic Anisotropy Near The Hawaiian Mantle Plume

by

Chenghao Shen

Master of Science in Earth Sciences

University of California, San Diego, 2017

Professor Gabi Laske, Chair

Seismic anisotropy, the dependence of velocity on direction, is often induced by mantle flow. Here, I studied the influence of a proposed mantle plume beneath Hawaii on the azimuth dependence of Rayleigh wave phase velocity. I used a two-layer forward modeling code to explore how the orientation of a transversely isotropic Pyrolite mantle model controls the fast direction and strength of azimuthal anisotropy. Two layers are assumed because plate motion of the Pacific plate rearranged about 45 Million years ago. It is thought that the fossil spreading direction was frozen into parts of the lithosphere while the asthenosphere below carries the signature of current mantle flow. Depending on how different the horizontal orientation of Pyrolite is in both layers, the strength of

anisotropy can vanish for some frequencies but not others. This can ultimately be used to estimate the thickness of the anisotropic layers and the orientation of Pyrolite.

In the second part, I forward-modeled data collected for the Hawaiian PLUME project. At high frequencies, the overall pattern of azimuthal anisotropy follows the fossil spreading direction while this coherency breaks down at low frequencies. I find that anisotropy in the upper lithosphere is largely intact, but the pattern is incoherent in the lower lithosphere and asthenosphere. These results provide strong evidence for the presence of a mantle plume beneath Hawaii.

Summary

In my thesis, I explored Rayleigh wave azimuthal anisotropy observed during the second deployment for the Hawaiian Plume-Lithosphere Undersea Mantle Experiment (PLUME). The primary goal of this research was to find evidence of plume-related mantle flow that would disturb the Pacific plate moving across the Pacific ocean. In the absence of a plume, Rayleigh wave azimuthal anisotropy should show a frequency dependence that is consistent with the fossil spreading direction of 76° 'frozen' into the lower lithosphere, while current mantle flow in the asthenosphere below occurs at an azimuth of 124°.

In chapters 1 through 3, I provide principal background information on seismic surface wave dispersion and its dependence on structure with depth. Surface waves at increasing frequencies have sensitivity to shallower structure where the sensitivity is a complex frequency-dependent integral over depth. I also provide background information on seismic anisotropy and its causes. The simplest anisotropy model to explain Rayleigh-wave azimuthal anisotropy is a transversely isotropic medium that is tilted away from the vertical. The orientation of the corresponding symmetry axis is then described by two angles, the inclination, θ, and the azimuth, ϕ.

In chapter 4, I analyze Rayleigh wave azimuthal anisotropy from data collected

for PLUME. Azimuthally varying frequency-dependent phase velocity was previously observed from 27 station triangles and made available to me. Using a truncated trigonometric series, I attempted to model observations for triangle 2 using different truncation levels and data weighting schemes. The goal of this effort was to obtain the two principal frequency-dependent observables of azimuthal anisotropy: the fast direction and strength of anisotropy.

Before modeling the observations any further, I performed extensive forward modeling in chapter 5. Here, I used a modeling code that predicts frequency-dependent Rayleigh wave azimuthal anisotropy for a model that has two anisotropic layers in the mantle that are sandwiched between an isotropic crust and uppermost mantle above as well as an isotropic mantle below. In a series of tests, I explored the impacts of varying the layer boundaries as well as the inclination angles and azimuths of the symmetry axes of anisotropy in the two layers. Weak anisotropy at low frequencies but strong anisotropy at high frequencies indicate a thin anisotropic layer at shallow depth. Strong anisotropy at low frequencies but weak anisotropy at high frequencies means that anisotropy has to start at great depth. Anisotropy increases as the incidence angle of the symmetry axis approaches the horizontal (90°). But the strength of anisotropy does not change much once the incidence angle reaches 45°. One of the most important results is that the strength of anisotropy can drop dramatically for certain frequencies as the difference in azimuths becomes larger. The frequency at which this occurs depends on the difference of the azimuths.

In chapter 6, I performed a grid search for four parameters in the two-layer model on the example data of triangle 4. I searched for the bottom of layer 1, the top of layer 2 as well as the fast direction of anisotropy in both layers. Here, I experimented with

different ways of computing the misfit and weighting the two types of data (strength of anisotropy and fast direction). The ultimate goal of this chapter was to obtain modeling results for all 27 triangles.

In chapter 7, I summarize the results from the grid-search modeling. I display the top of layer 2 and the total thickness of upper-mantle anisotropy. I find that to the southeast and west of Hawaii, anisotropy starts at relatively great depth (some 70 km) compared to the area along the islands and toward the north (35 km). The overall thickness of mantle anisotropy seems incoherent though anisotropy tends to be quite thin (less than 40 km) to the southwest of Hawaii. The fast axis of anisotropy is quite coherent in the upper layer and broadly aligns with the fossil spreading direction, as expected. In the low layer, however, this pattern breaks down. Along the islands and to the east, the fast direction aligns with the current plate motion direction, and some directions south are perpendicular to this. The combination of these observations could potentially be consistent with the parabolic mantle flow expected for an ocean plate overriding a mantle plume.

Chapter 1

Surface Waves

1.1 Introduction

Surface waves travel along the great circle path at the surface of the earth and go differently from body waves which are fundamentally traveling inside the earth. Away from the free surface, their amplitude decays exponentially with increasing depth. The observed velocity of surface waves is usually much lower than that of body waves. For shallow earthquakes, the amplitude of surface waves are the largest of all the seismic phases in the seismogram. As a result of geometric spreading, wave energy spreads in two-dimensional space and therefore the energy of the waves attenuates with $1/r$. In contrast, body waves travel in a three-dimensional space and they attenuate with $1/r^2$(Stein and Wysession, 2003). So body waves show smaller amplitudes in seismograms at the same epicentral distance. Typically surface waves excited by very large earthquakes can circle the earth for several times, which is called multiple surface waves. One of the most distinctive property of surface waves is their dispersion, which means velocity varies with frequency. The dispersion of surface waves is regarded as a effective tool to help scientist study earth structure.

1.2 Love Waves

Love waves exist along the free surface of a medium only when the velocity structure varies with depth. This means that Love waves do not exist in a homogeneous half space. However, even in a layer over a half space, Love waves exist only if $\beta_2 > \beta_1$ as shown in figure 1.1. Typically, in this circumstance, full reflection will not occur until the incidence angle of the ray path reaches the critical angle j, which is defined as $sin(j) = \beta_1/\beta_2$. Consequently, Love waves do not form within a critical distance $d = 2htan(j)$, which is also shown in figure 1.1. Love waves are the result of interference of SH polarized waves. One can understand surface waves as a combination of multiple reflected body waves. i.e. the direct S-wave and waves that bounced several times at the free surface. (Such as SS,SSS,SSSS, etc.) As shown in figure 1.2, several multiple reflected phases with different ray parameters propagate in a medium with a vertical velocity gradient. The ray paths bend over to the surface and bounce at several bouncepoints. SH waves at certain frequencies constructively interfere with each other and form Love waves. The frequencies are dominated by the dispersion relation(Stein and Wysession, 2003) which will be introduced in the following parts.

1.3 Rayleigh Waves

Rayleigh waves are formed by interference of P-waves and SV-waves. Taking the situation in Poisson solid as an example(A medium which has a Poisson ratio of 0.25). The particle motion is shown in Figure 1.4. In order to describe the polarization of

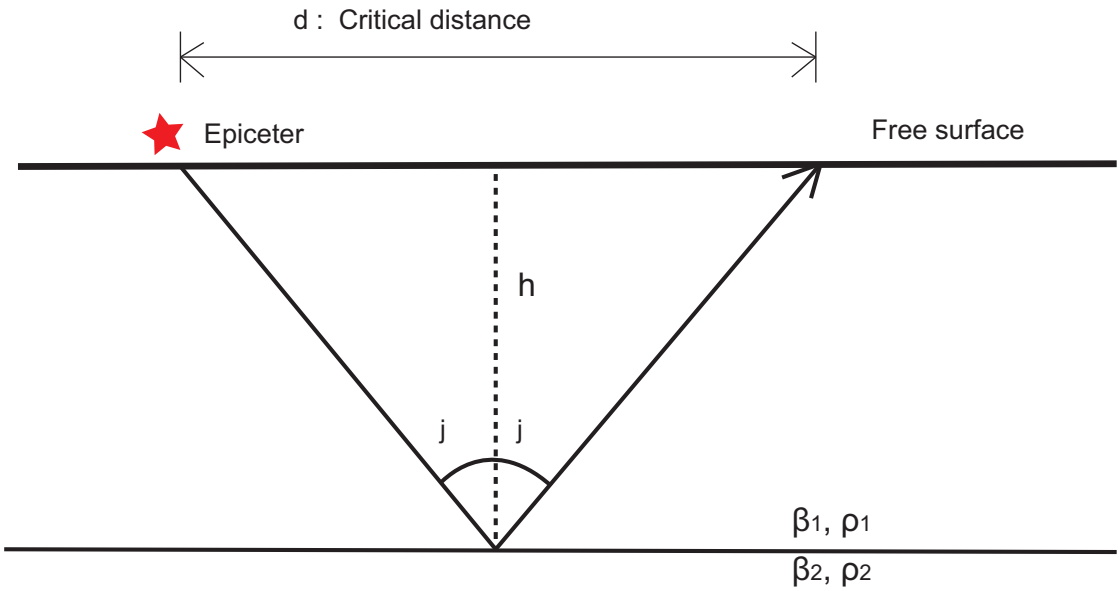

Figure 1.1: Full reflection can only occur when the incidence angle of the ray path is larger than the critical angle j. Thus, there's no Love wave within the critical distance.

Rayleigh waves, the particles move in an elliptical way, which means the motion consists of both radial and vertical motion that are out of phase by $\pi/2$. The way of motion is shown in figure 1.4. At the surface, its motion is retrograde, which means the motion is against the direction of propagation. However, at some specific depth, the motion changes to prograde. The amplitudes of motion decay exponentially with depth. On one hand, when propagating in a homogeneous half space medium, Rayleigh waves show no dispersion and their phase and group velocity are the same. On the other hand when Rayleigh waves propagate in a medium with vertical velocity gradient, both phase and velocity vary with frequency. The phenomenon is termed as dispersion.

1.4 Dispersion

In principle, dispersion means that the velocity of propagation along the surface of medium varies with frequency. The dispersion of Love waves depends on shear

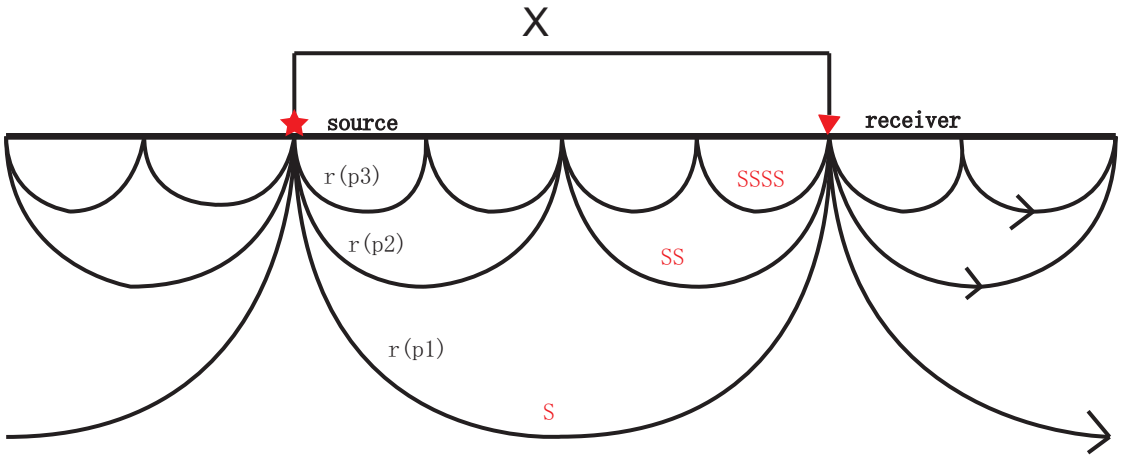

Figure 1.2: Ray paths with different ray parameters to form Love waves. X is the source-receiver distance (epicentral distance). r(p1), r(p2), r(p3) are different ray parameters of the ray paths. S is the direct SH wave, SS is the SH wave that has been reflected for once by the surface. And SSSS has been reflected for three times.

velocity while the dispersion of Rayleigh waves depends on both compressional and shear velocity in the medium. There are two kinds of velocity of surface waves: group velocity and phase velocity, both of which are dispersive. The phase velocity is the velocity of individual wave peaks and troughs(shown in figure 1.6). And the group velocity is the velocity of wave packets with which the energy is transported or the velocity of a point on the envelope. Phase velocity is defined as $c = \frac{\omega}{k}$ and group velocity is defined as $U = \frac{d\omega}{dk}$, where k is the wave number and ω is the angular frequency. In a realistic earth model, wave groups is a combination of various phases. So group velocity is a more complex function of frequency than phase velocity. As illustrated in figure 1.5 and as explained earlier, a surface wave with longer period can penetrate deeper into a medium. Usually the compressional and shear velocity increases with depth in the earth. Thus, the phase velocity of surface waves decreases with increasing frequency(showed in figure 1.7). By contrast, the group velocity curve does not seem to be monotonously increasing or decreasing. Usually, group velocity is smaller than phase velocity. In figure 1.7, both curves of group velocities of Love waves and Rayleigh

waves have some local minimum or maximum points at specific frequencies which are termed as Airy Phase. Energy of surface waves in a small frequency band will arrive at almost the same time to form an Airy phase. When an Airy phase occurs, in the dispersion curves, the group velocity will increase or decrease at both sides of an Airy phase.

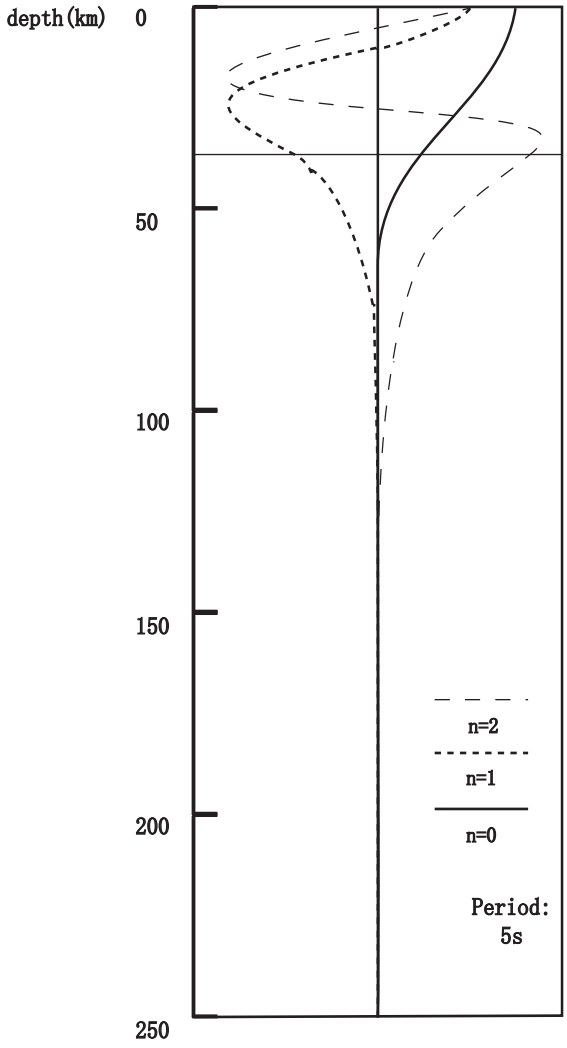

Figure 1.3: Love wave displacement of fundamental mode(n=0) and higher order modes(n>0). At fixed period of 5s, higher modes penetrate deeper into the medium than the fundamental mode.(Modified after Stein and Wysession, 2003)

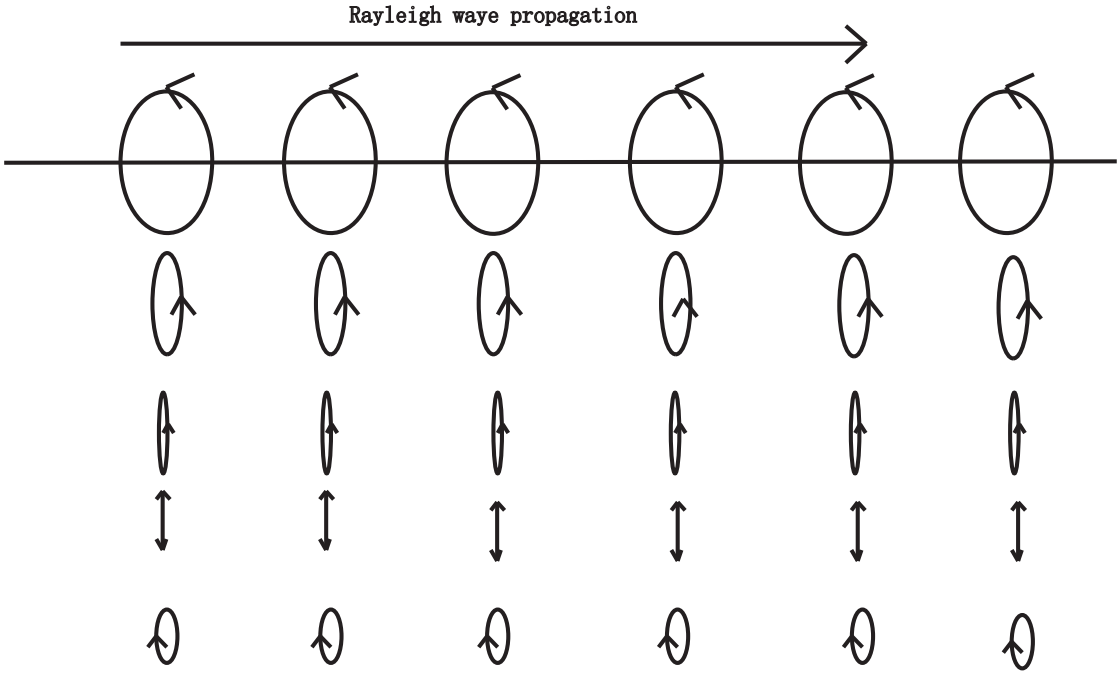

Figure 1.4: Particle motion of Rayleigh waves decays with increasing depth: At the surface particle motion is retrograde; At great depth, particle motion is prograde.(Modified after P. Shearer,2009)

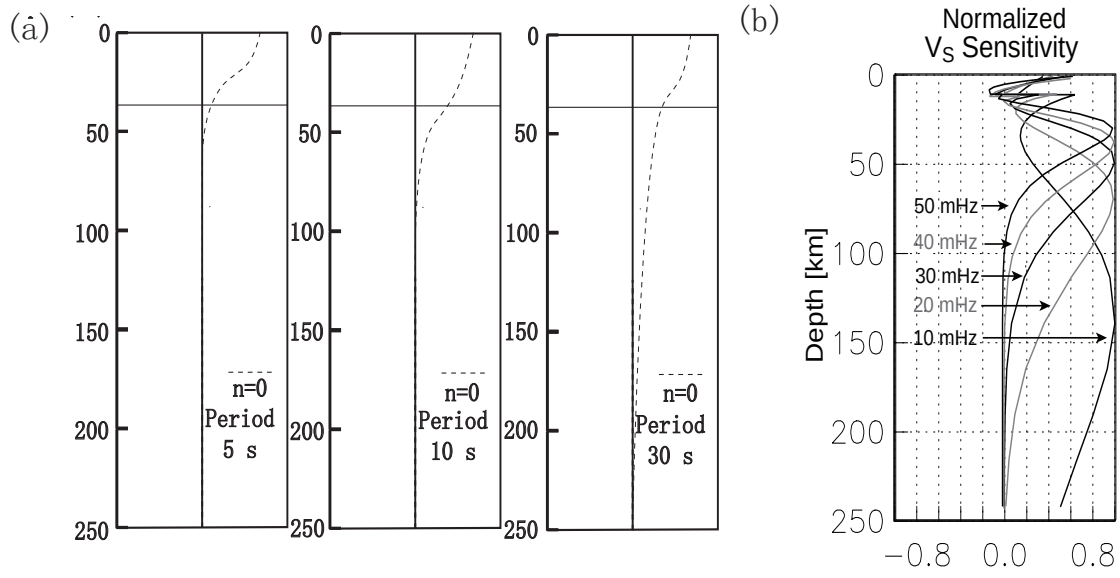

Figure 1.5: Panel (a): Different displacement with depth for different periods of fundamental-mode Love waves. Love waves with longer periods penetrate deeper into the medium.(Modified after Stein and Wysession, 2003) Panel (b): Sensitivity kernels for Rayleigh wave phase velocity to shear velocity structure with different frequencies.(modified from Laske et al., 2011)

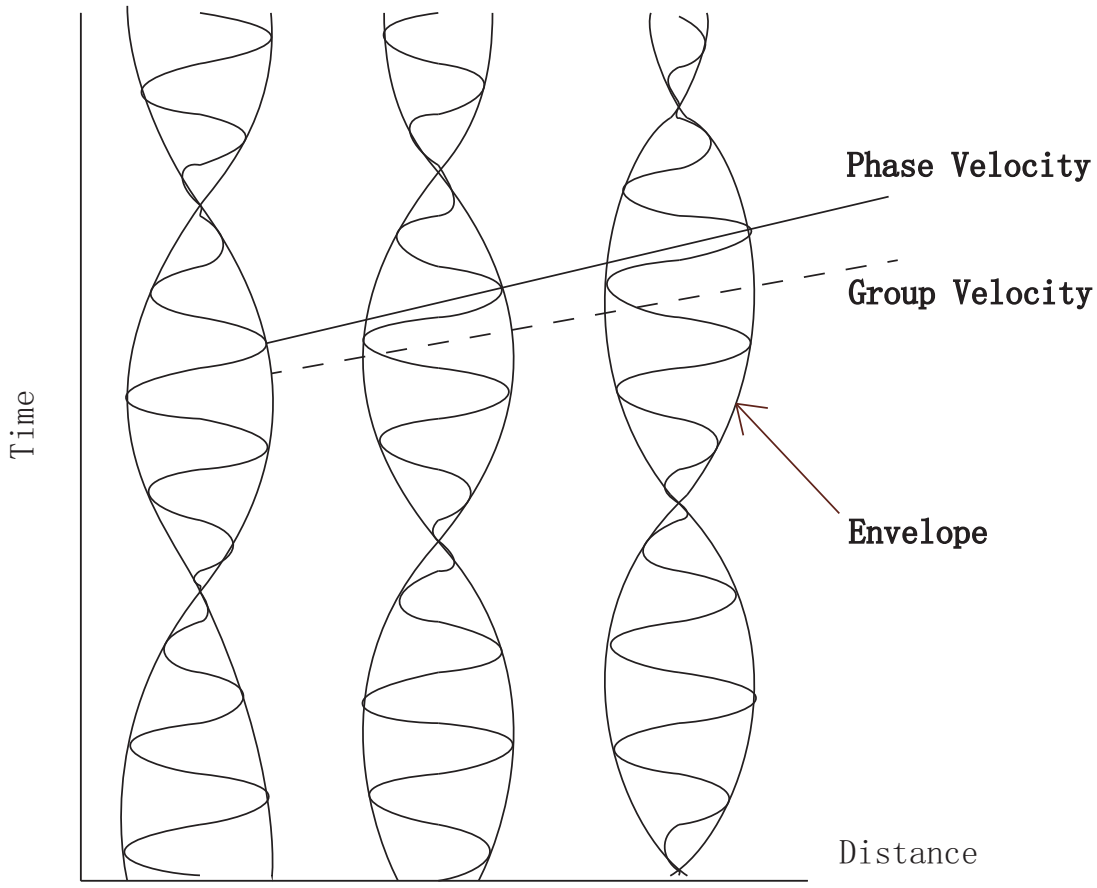

Figure 1.6: Showing difference between group velocity and phase velocity(Modified after P. Shearer, 2009)

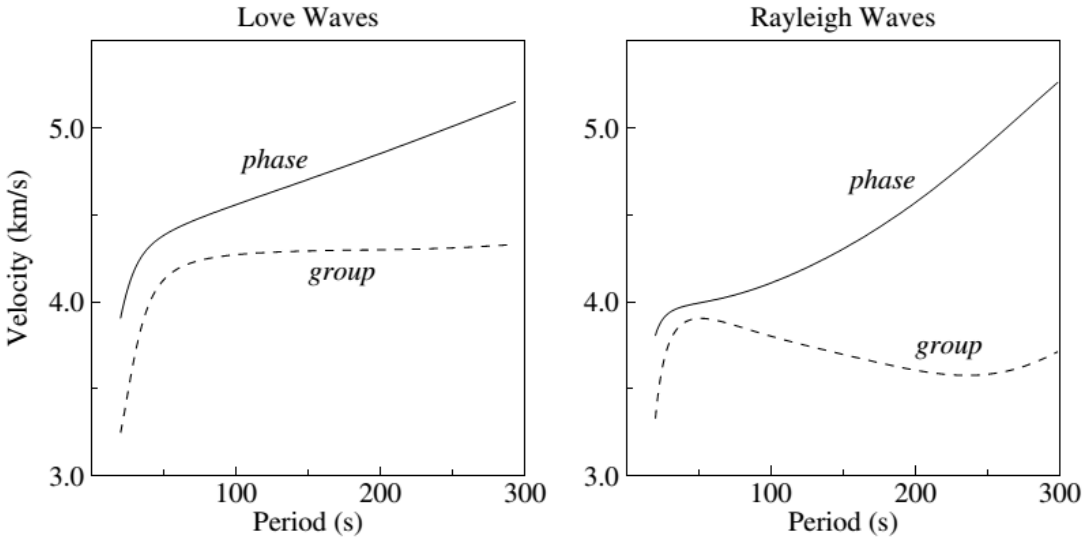

Figure 1.7: Fundamental Love wave and Rayleigh dispersion curves computed from the isotropic PREM model(Figure from Shearer, 2009; courtesy of Gabi Laske)

Chapter 2

Surface Waves Azimuthal Anisotropy

2.1 Theory of Anisotropy

To start with anisotropy, we need to highlight the general concept of anisotropy is that the velocity of a seismic wave traveling in an anisotropic medium is highly dependent on the direction of propagation. As an example, S-wave birefringence is one of the most common consequence of anisotropy.

Anisotropy is common in Earth's medium when specific structures(i.e. layering and cracks with adequate scales) and lattice-preferred orientation of mineral(i.e. Olivine give rise to the anisotropy in mantle) occurs.

In principle, an anisotropic medium can be viewed as special case of heterogeneity. At a microscopic scale, anisotropy can be the consequence of crystal structure. For instance, olivine in the mantle is made of $(MgFe)_2SiO_4$, which is anisotropic because of the way the element are arranged in the crystal lattice. A single Olivine crystal has an orthorhombic structure. A sketch of a olivine crystal is plotted in figure 2.1. Whereas

at a larger scale, anisotropy can also be caused by a whole range of structures such as cracks and layering. In order to explain that, figure 2.2 is plotted to show the concept of how cracks and layering contribute to anisotropy. What distinguishes anisotropy from heterogeneity is the relative scale of heterogeneous with respect to the wavelength of a seismic wave. If the wavelength of a seismic wave is large enough to meet the scale of heterogeneity caused by layering or cracks, then this anisotropy can be seen by the seismic wave. In our study, The wavelength of surface waves are as large as several hundreds of kilometers, which exceed the dimension of geological structures far and away.

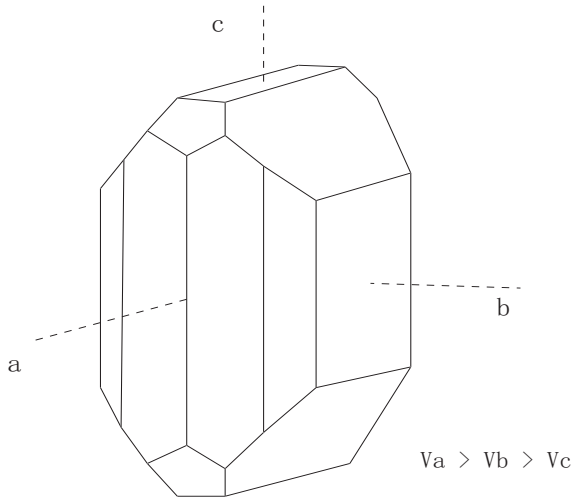

Figure 2.1: The figure shows a sketch of a olivine crystal and its a, b and c axis. The crystal has an orthorhombic structure. V_a, V_b, V_c are the velocity with respect to a, b and c axis(modified after Stein and Wysession, 2002)

An elastic wave propagates through a medium when a perturbation is exerted on it. In case of an elastic medium, a linear expression describe the relationship between the stress tensor τ_{ij} and the strain tensor e_{kl}:

$$\tau_{ij} = c_{ijkl} e_{kl} \tag{2.1}$$

where c_{ijkl} is the elastic constant. Considering the symmetry of some of the stress and

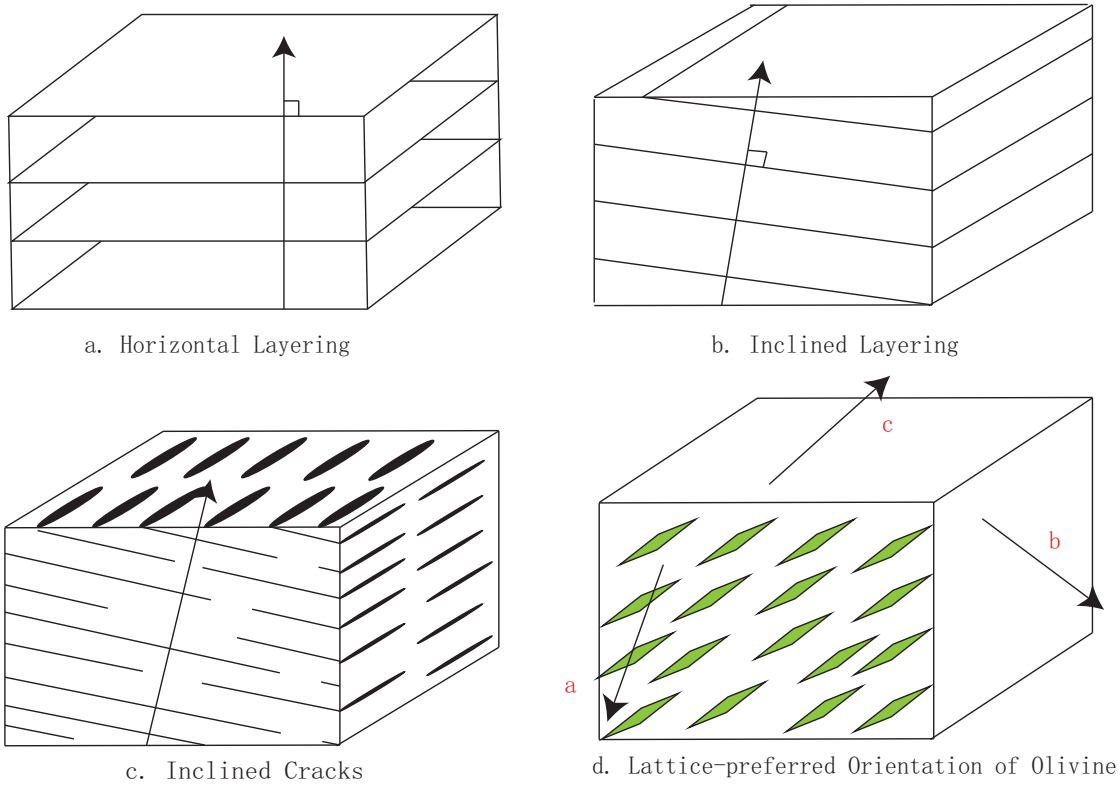

Figure 2.2: panel (a) shows the simplest model of horizontal layering in the case of horizontal transverse isotropy(HTI) which will be introduced in the following paragraphs. No anisotropy presents at (a), if the ray paths are assumed to be horizontal. panel (b) shows a more realistic model, the symmetrical axis inclines and the layers are no longer horizontal. Anisotropy occurs in the horizontal plane. Panel (c) shows a medium with a whole set of cracks. It cause anisotropy in the similar way as (b). Panel (d) shows how lattice-preferred orientation(LPO) give rise to anisotropy.

strain components, the 81 components of c_{ijkl} has been simplified to as much as 21 independent components:

$$c_{ijkl} = c_{ijlk} = c_{jikl} = c_{klij} \tag{2.2}$$

When further simplification applied, which means even more symmetrical components exist at specific conditions, the amount of independent components can be even smaller. Usually, when the number of independent elastic constants is larger than two(the case of two independent elastic constants stands for isotropic medium), the elastic medium responds to a elastic wave differently with various directions of wave propagation. There-

fore, our observation shows that the wave velocity changes with various direction of wave polarizations.

Diagram (a) in figure 2.3 shows the wavefronts and propagation directions of phase and group velocity respectively in isotropic medium. Diagram (b) in figure 2.3 shows the case in anisotropic medium. In homogeneous isotropic medium, the wave velocity is the same in all direction and the wavefront is spherical. The group and phase velocity travel in the same path from the source to the wavefront. In homogeneous anisotropic medium, the group velocity also follows a straight path from the wave source to the wavefront. The difference between the directions of phase and group velocity depends on the curvature of the wavefront through the relation:

$$V = C + \frac{\partial C}{\theta} \tag{2.3}$$

where θ is the azimuth angle and $C = c\vec{n}$, c is the phase velocity. The vector $\vec{n}$ defines the direction of the phase propagation, and is perpendicular to the wavefront. Wave energy travels in another direction, defined by the group velocity direction V.

For weak anisotropy, the waves can be separated into a quasi-P wave, with the highest velocity and a polarization close to the propagation direction, and two quasi-S waves, which are labeled as quasi-SH waves and quasi-SV waves. quasi-SH waves and quasi-SV waves have different velocities with two polarization directions perpendicular to each other. The direction of wave propagation are not generally perpendicular to their respective wavefront, except for the propagation direction with symmetry of elasticity. As for strong anisotropy, P-wave and S-waves with two polarizations perpendicular to each other can not be labeled explicitly due to a high level of hybridization. In our study,

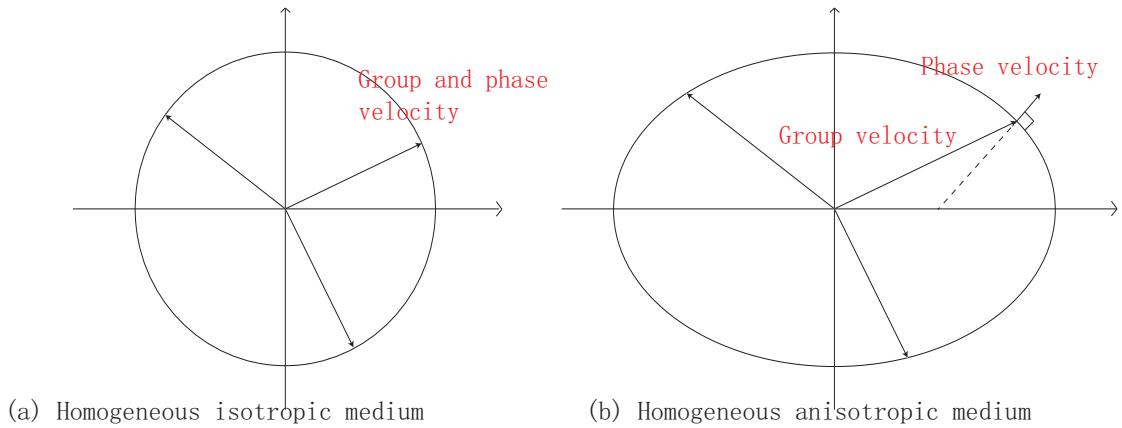

(a) Homogeneous isotropic medium (b) Homogeneous anisotropic medium

Figure 2.3: The figure illustrates a concept of group and phase velocity in both homogeneous isotropic medium and homogeneous anisotropic medium. The direction of group velocity is pointed from wave source to wavefront while the phase velocity is always perpendicular to the wavefront. (a) shows the wavefront in a homogeneous isotropic medium in which the waves travel at the same velocity in all direction. Diagram (b) shows the wavefront in a homogeneous anisotropic medium and the wavefront is elliptical.

we would focus on weak anisotropic medium.

Assuming a first-order approximation about the differences between the isotropic and anisotropic elastic constants, the azimuthal variation of the velocity of quasi-P waves, quasi-SV waves and quasi-SH waves within the X_1-X_2 plane are expressed as follows(Crampin, 1977). The formulas are expressed in the form of trigonometric series which has been truncated to second order.

$$\begin{aligned} \rho V_p^2 &= A + B_c\cos(2\psi) + B_s\sin(2\psi) + C_c\cos(4\psi) + C_s\sin(4\psi) \\ \rho V_{SH}^2 &= D - C_c\cos(4\psi) - C_s\sin(4\psi) \\ \rho_{SV}^2 &= F + G_c\cos(2\psi) + G_s\sin(2\psi) \end{aligned} \tag{2.4}$$

where

$$
\begin{aligned}
A &= \frac{3(C_{11}+C_{22})+2C_{12}+4C_{66}}{8} \\
B_c &= \frac{C_{11}-C_{22}}{2} \\
B_s &= C_{16}+C_{26} \\
C_c &= \frac{C_{11}+C_{22}-2C_{12}-4C_{66}}{8} \\
F &= \frac{C_{44}+C_{55}}{2} \\
G_c &= \frac{-C_{44}+C_{55}}{2} \\
G_s &= C_{45}
\end{aligned} \tag{2.5}
$$

ρ is the density and ψ is the azimuth measured from the X_1 axis to the X_2 axis, V_P, V_{SH}, V_{SV} are phase velocity of quasi-P waves, quasi-SH waves and quasi-SV waves. Further more,

$$
\begin{aligned}
C_{11} &= c_{1111} \\
C_{22} &= c_{2222} \\
C_{33} &= c_{3333} \\
C_{44} &= c_{2323} \\
C_{55} &= c_{1313} \\
C_{66} &= c_{1212} \\
C_{12} &= c_{1122}
\end{aligned} \tag{2.6}
$$

The second order approximation of Azimuthal dependence of surface waves also has similar form with the case in body waves shown above.

2.2 Transverse Isotropy

Anisotropy with a cylindrical symmetry is termed as transverse isotropy(TI). Figure 2.4 gives a concept of transverse isotropy(TI). Suppose in a medium with only one symmetric axis, the anisotropy is only depended on the incidence angles of seismic waves with respect to the axis. The symmetrical axis of a general TI medium can be in any directions including horizontal direction(HTI) or vertical direction(VTI). Fine-layering and a range of uniformly distributed cracks can be approximately regarded as transverse isotropy(TI). Moreover, the most important cause of TI in this study is the olivine crystallization, which is the major factor that cause the transverse isotropy(TI) in the mantle.

One of the most common notation for transverse isotropy(TI) is expressed as follows: five independent elastic coefficients are introduced A, C, F, L, N. When the symmetry axis is along axis x_3(VTI), we show the matrix c_{ij} as:

$$\begin{pmatrix} \text{A} & \text{A-2N} & \text{F} & 0 & 0 & 0 \\ \text{A-2N} & \text{A} & \text{F} & 0 & 0 & 0 \\ \text{F} & \text{F} & \text{C} & 0 & 0 & 0 \\ 0 & 0 & 0 & \text{L} & 0 & 0 \\ 0 & 0 & 0 & 0 & \text{L} & 0 \\ 0 & 0 & 0 & 0 & 0 & \text{N} \end{pmatrix} \tag{2.7}$$

where

$$
\begin{aligned}
A = \rho V_{PH}^2 &= \frac{3}{8}(c_{11}+c_{22}) + \frac{1}{4}c_{12} + \frac{1}{2}c_{66} \\
C = \rho V_{PV}^2 &= c_{33} \\
F &= \frac{1}{2}(c_{13}+c_{23}) \\
L = \rho V_{SV}^2 &= \frac{1}{2}(c_{44}+c_{55}) \\
N = \rho V_{SH}^2 &= \frac{1}{8}(c_{11}+c_{22}) - \frac{1}{4}c_{12} + \frac{1}{2}c_{66}
\end{aligned}
\tag{2.8}
$$

where ρ is density of the medium, V_{PV} is horizontal P-wave velocity, V_{PV} is vertical P-wave velocity, V_{SH} is horizontal S-wave velocity, and V_{SV} is vertical S-wave velocity (Montagner and Nataf, 1988).

In the isotropic case, A and C reduce to $\lambda + 2\mu$, F reduces to λ, and L and N reduce to μ.

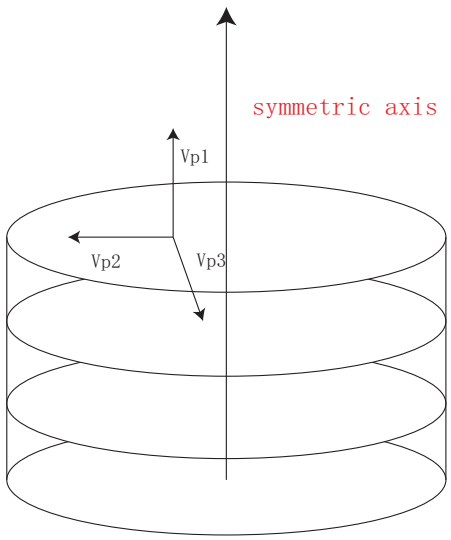

Figure 2.4: A concept of transverse isotropic(TI) model. $V_{P1} \neq V_{P2}, V_{P3}$ and $V_{P2} = V_{P3}$

2.3 Surface wave azimuthal anisotropy

Figure 2.5 shows the simplified models of azimuthal anisotropy by tilting the transverse isotropy, where θ is the inclination and ϕ is the azimuth. Especially, in case of $\theta = 0^\circ$, the medium is transversely isotropic. In case of $\theta = 90^\circ$, the medium gets to the strongest anisotropy.

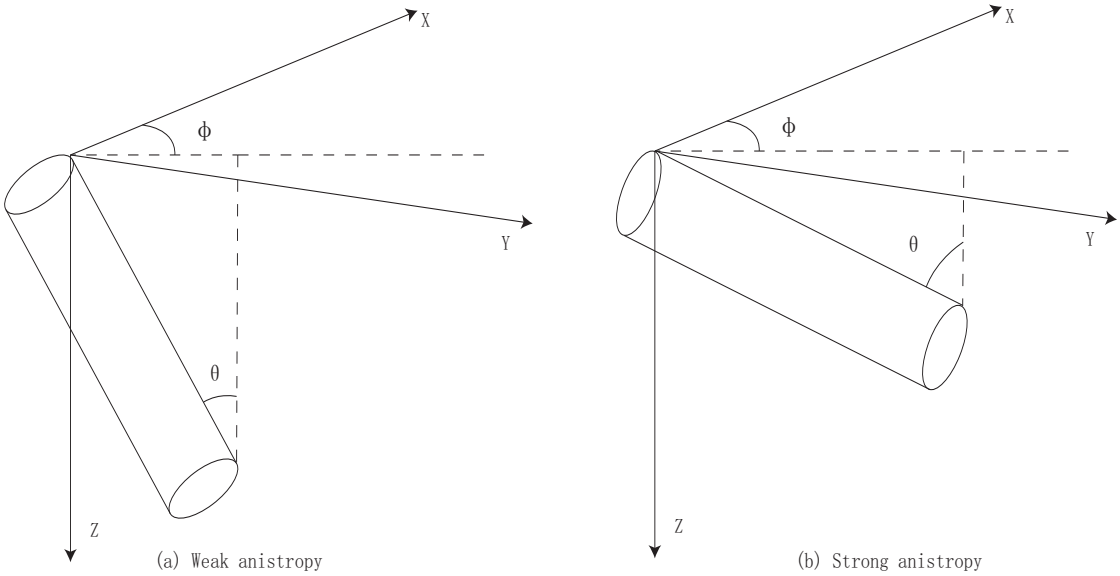

Figure 2.5: A comparison of azimuthal anisotropy with different tilting angle θ. Panel (a) shows a relatively weak anisotropy while panel (b) shows a strong anisotropy.

According to Smith and Dahlen's research(1973), the azimuthal dependence of both Love and Rayleigh phase velocity can be expressed in the same form:

$$c(\psi,\omega) = a_1(\omega) + a_2(\omega)\cos 2\psi + a_3(\omega)\sin 2\psi + a_4(\omega)\cos 4\psi + a_5(\omega)\sin 4\psi \quad (2.9)$$

where $c(\psi,\omega)$ is phase velocity, ω is angular frequency, ψ is azimuth, and a_1,a_2,a_3,a_4,a_5 are depth integral functions that depend on the elastic parameters of the medium through which the seismic waves are traveling.

Figure 2.6 shows the conceptual plots of phase velocity $c(\psi)$ with various values of a_2, a_3, a_4, a_5. a_1 is set to 5%, which is the average level of phase velocity variation. As shown in panel (a), a_2, a_3 are an order of magnitude larger than a_4, a_5, then the 2ψ terms dominate. If we neglect the 4ψ term, then the phase velocity can be expressed as:

$$c(\psi) = 5 + 2\cos 2\psi + 2\sin 2\psi \tag{2.10}$$

The phase velocity is a periodic function with a period of 180 degrees. In the plot, the curve gets to its first maximum at 22 degrees and 23 degrees. Since the trigonometric function is symmetric, it has a phase shift of 22.5 degrees. For panel (b), $a_4, a_5 = 2\%$ are larger than $a_2, a_3 = 0.1\%$, then the 4ψ terms are the dominant terms. The dominant period becomes 90 degrees but still shows some slight 180-degree periodicity because $a_1, a_3 \neq 0$. Analogous to (a), the phase velocity can be written as:

$$c(\psi) = 5 + 2\cos 4\psi + 2\sin 4\psi \tag{2.11}$$

The first maximum of the curve is at 9 degrees. Due to a smaller weight of 2ψ terms, the nearby maximums and minimums are uneven. In panel (c) a_2, a_3, a_4, a_5 are equal, azimuthal anisotropy is composed of 2ψ terms and 4ψ terms but the 180-degree periodicity dominates. In each period, it has two non-equal maximums as well as two non-equal minimums. The first maximum is at 13 degrees and the first minimum is at 62 degrees. In panel (d), if we assume a different a_2 and a_3 compared with (a), this plot has a 180-degree periodicity but a phase shift of 35.8 degrees. Derivation is shown as following:

$$c(\psi) = 5 + \cos(2\psi) + 3\sin(2\psi) \tag{2.12}$$

In order to transform from $\cos(2\psi) + 3\sin(2\psi)$ to $A\sin(2\psi+\beta)$

$$c(\psi) = 5 + \sqrt{10}\left[\frac{1}{\sqrt{10}}\cos(2\psi) + \frac{3}{\sqrt{10}}\sin(2\psi)\right] \tag{2.13}$$

Assume $\frac{1}{\sqrt{10}} = \sin(\beta)$ and $\frac{3}{\sqrt{10}} = \cos(\beta)$

$$c(\psi) = 5 + \sqrt{10}\,[\sin(2\psi+\beta)] \tag{2.14}$$

where $\beta = \arccos(\frac{3}{\sqrt{10}}) = 18.4$

$$c(\psi) = 5 + \sqrt{10}\,[\sin(2(\psi+9.2))] \tag{2.15}$$

This curve has a phase shift of 9.8 degrees, and its first maximum is at 35.8 degrees. In panel (e), if we set different a_2, a_3 and a_4, a_5, the amplitude of the 4ψ term change significantly comparing with panel (c) while the periodicity of both 2ψ term and 4ψ term remain the same. The first maximum shows up at 12 degrees.

a_1, a_2, a_3, a_4, a_5 of each panel are shown in table 2.1

Table 2.1: Parameters from a1 to a5

panel	a1(%)	a2(%)	a3(%)	a4(%)	a5(%)
a	5	2	2	0.1	0.1
b	5	0.1	0.1	2	2
c	5	1	1	1	1
d	5	1	3	0.1	0.1
e	5	1	1	3	3

In real case, we use several data points to recover the curve of azimuthal anisotropy. According to Nyquist sampling criterion, the sampling frequency should be twice the frequency of a sinusoid. As for panel (a) of figure 2.6, we need at least 3 data

points(which is plotted as red dot in panel (a)) at nearby maximums and minimums to resolve the plot of 2ψ terms. However, the data points may not be evenly distributed at each maximums and minimums. Thus, more data points are needed to resolve the curve. For 4ψ terms, we need a higher sampling frequency to avoid aliasing which means more data are used to resolve the azimuthal anisotropy of Love waves. Sometimes we can't get enough density of distribution of data.

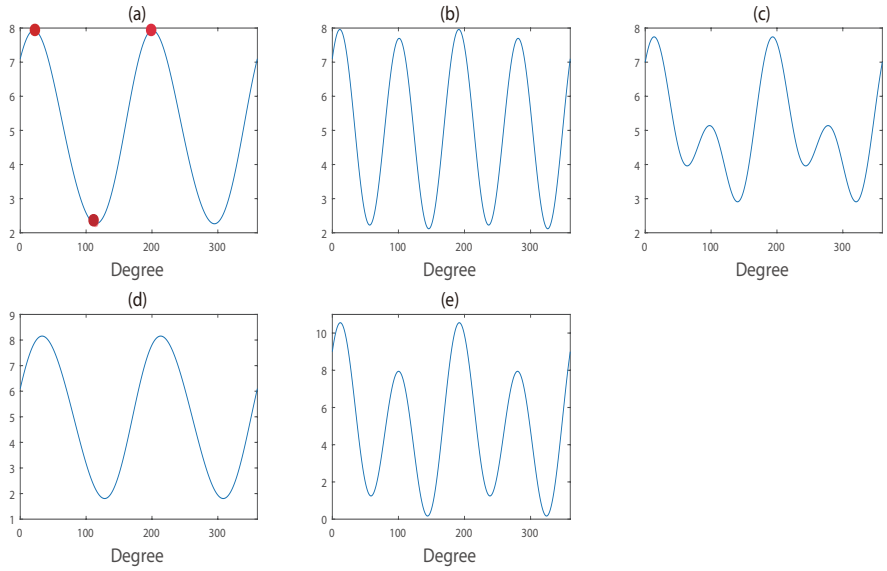

Figure 2.6: For panel (a), $a_1 = 5\%, a_2 = a_3 = 2\%, a_4 = a_5 = 0.1\%$; For panel (b), $a_1 = 5\%, a_2 = a_3 = 0.1\%, a_4 = a_5 = 2\%$; For panel (c), $a_1 = 5\%, a_2 = a_3 = a_4 = a_5 = 1\%$ are of the same order; For panel (d), $a_1 = 5\%, a_2 = 1\%, a_3 = 3\%, a_4 = a_5 = 0.1\%$; For panel (e), $a_1 = 5\%, a_2 = a_3 = 1\%, a_4 = a_5 = 3\%$

Figure 2.7 shows a concept of how we measure the azimuthal anisotropy of phase velocity. Each network consists of several stations. We assume the a constant velocity within each network. And then we fit a spherical wavefront to the travel time data at each station by using a least-square method. In this way, we calculate the phase velocities with respect to different propagating directions.

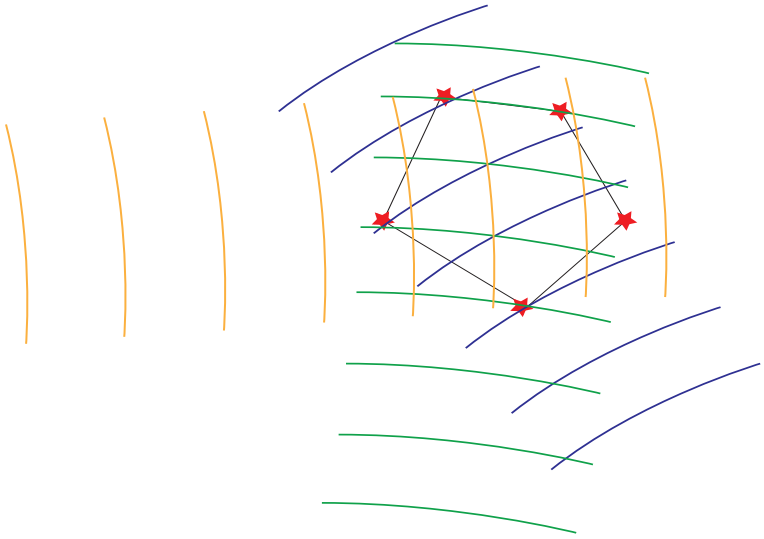

Figure 2.7: A conceptual map of station network: red stars are the stations. orange, blue and green curves stand for different wave phases

2.4 Surface Dispersion and Structure at Depth

In a transversely isotropic medium, the integral function $a_1(\omega)$ for Love waves can be formulated as:

$$a_1(\omega) = a_0(\omega)\left[\int_0^a K_N(z,\omega)N(z)dz + \int_0^a K_L(z,\omega)L(z)dz + \int_0^a K_\rho(z,\omega)\rho(z)dz\right] \tag{2.16}$$

where $a_0(\omega)$ is a normalization factor and a is the Earth radius. In case of no azimuthal dependence, $a_1(\omega)$ is the phase velocity in either an isotropic medium or in a transversely isotropic medium. Note that Loves waves are related to both L and N, or v_{SV} and v_{SH} respectively. But usually sensitivity to v_{SV} is ignored because it is much smaller (shown in figure 2.8).

For Rayleigh waves, we have

$$a_1(\omega) = a_0(\omega)[\int_0^a K_A(z,\omega)A(z)dz + \int_0^a K_c(z,\omega)C(z)dz + \int_0^a K_L(z,\omega)L(z)dz + \int_0^a K_g(z,\omega)g(z)dz] \quad (2.17)$$

Figure 2.9 shows the sensitivity Kernels for Rayleigh waves of 40s. Note that Rayleigh waves have no sensitivity to N (V_{SH}).

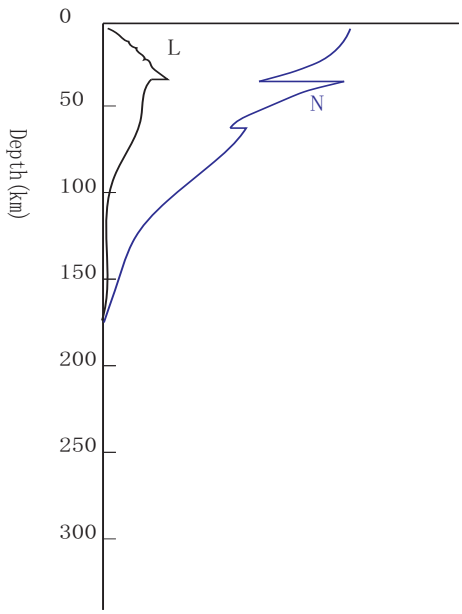

Figure 2.8: Conceptual drawing of sensitivity kernels of Love wave phase velocity at a period of 40s. L is related to V_{SV}. N is related to V_{SH}. (modified after Gerald Schubert, 2015)

Montagner and Nataf(1986) introduced several constant terms independent of azimuth in addition to A, C, F, L, N.

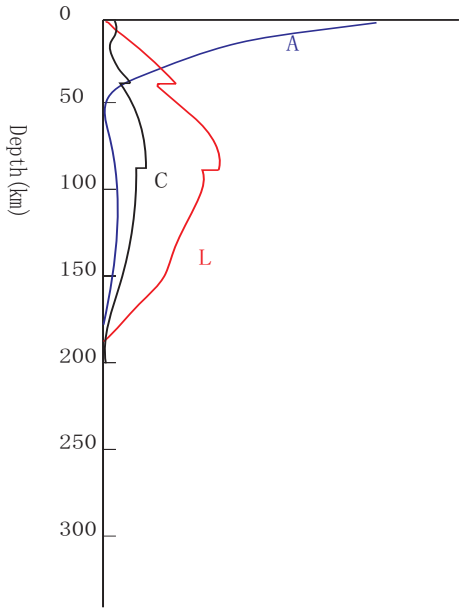

Figure 2.9: Conceptual drawing of sensitivity kernels of Rayleigh wave phase velocity at a period of 40s. A is related to V_{pH}. C is related to V_{pV}. L is related to V_{SV}. (modified after Gerald Schubert, 2015)

2ψ terms:

$$\begin{aligned} B_C &= \frac{1}{2}(c_{11} - c_{22}) \\ B_S &= c_{16} + C_{26} \\ G_C &= \frac{1}{2}(c_{55} - c_{44}) \\ G_S &= c_{54} \\ H_C &= \frac{1}{2}(c_{13} - c_{23}) \\ H_S &= c_{36} \end{aligned} \tag{2.18}$$

4ψ terms:

$$\begin{aligned} C_C &= \frac{1}{8}(c_{11} + c_{22}) - \frac{1}{4}c_{12} - \frac{1}{2}c_{66} \\ C_S &= \frac{1}{2}(c_{16} - c_{26}) \end{aligned} \tag{2.19}$$

First, the partial derivatives of the constant terms with respect to the elastic coefficient (A, C, F, L, N) are equal to the the partial derivatives of the azimuthal terms with respect to the other elastic coefficients $(B_C, B_S, G_C, G_S, H_C, H_S, C_C, C_S)$. Panel (a) in figure 2.10 shows the partial derivatives for Love waves. The partial derivative with respect to L (related to SV-velocity) is equal to the partial derivative with respect to $-G_C$ in the 2ψ term. The partial derivative with respect to N (related to SH-velocity) is equal to the partial derivative with respect to $-C_C$ in the 4ψ term. Since Love waves are dominated by SH-velocity, C_C is dominant for Love wave. On the contrary, for Rayleigh waves, the derivatives with respect to C_C only have small value except in very shallow zone. Therefore, at the depth we are interested in, G_C dominates just as panel (b) shows.

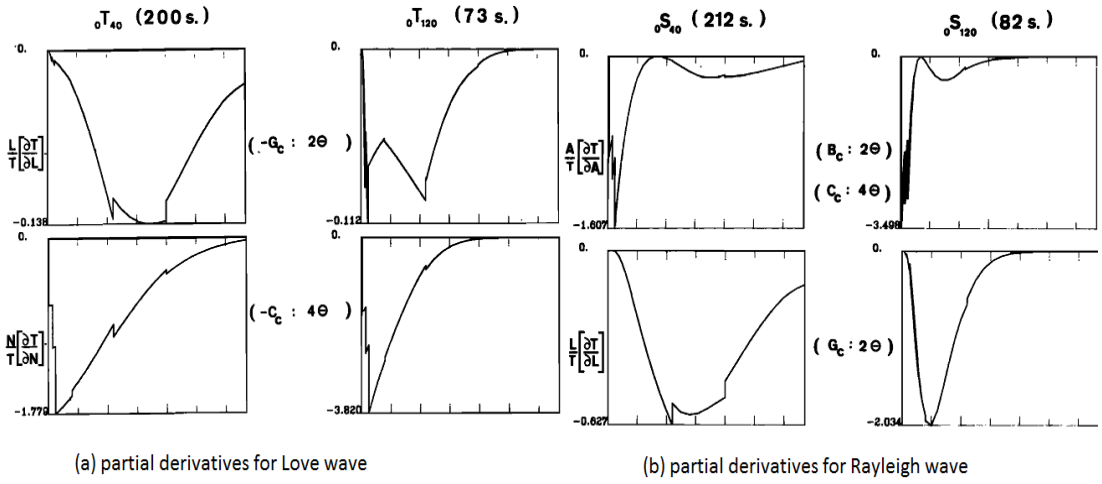

Figure 2.10: A sketch of partial derivatives for both Love waves and Rayleigh waves(Montagner and Nataf, 1986)

Chapter 3

Case Study Hawaii

3.1 Reviews of Plate Tectonics

The lithosphere is a thin shell made of the crust and the uppermost mantle. Figure 3.1 shows a concept of a spreading and cooling lithosphere. It has a lower temperature relative to the asthenosphere beneath. The lithosphere is assumed to be rigid while the asthenosphere is soft and can deform in response to stresses and mantle drag. The boundary of the lithosphere and the asthenosphere is an isotherm of approximately 1600(K) according to Turcotte and Schubert, 2014. An oceanic lithosphere is formed at the mid ocean ridge and disappears at the subduction zone. Due to the rigidity of the lithosphere, the dragging force from the subduction zone and the pulling force from the mid ocean ridge can be transmitted to the whole lithosphere, which accounts for the dynamics of plate motion. Hot asthenosphere rises up to fulfill the gap between two pieces of lithosphere which are called plates. When the oceanic lithosphere moving away from the ocean ridge, it gets cooler. Then the mantle rocks from the asthenosphere are added to the bottom of the oceanic lithosphere, which means the lithosphere is thickening when the distance from the mid ocean ridge gets larger. As the oceanic lithosphere gets cooler, it

also gets denser and lose its gravitational buoyancy. Finally it descends at the subduction zone where it gets melted into the asthenosphere again. This makes up a cycle of a whole life span of oceanic lithosphere.

Anisotropy is formed is this process. When the mantle rocks are being added to the bottom of the lithosphere, they are also being driven to flow with the spreading of lithosphere. Pyrolite in the asthenosphere is anisotropic because of flowing. As the mantle flow is ”frozen”, it causes an increase in the anisotropy in the lithosphere. Figure 3.2 shows a concept figure about that.

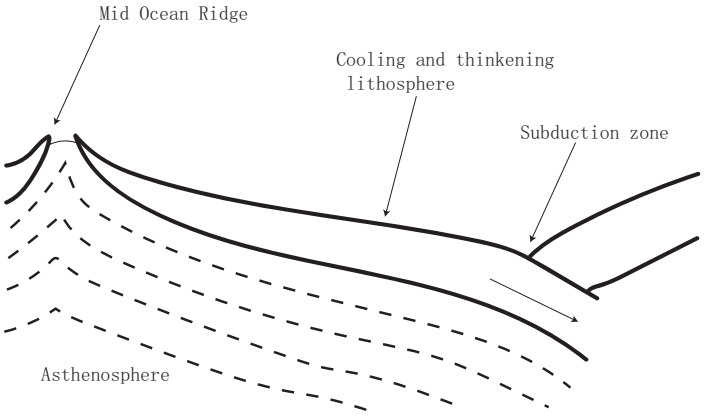

Figure 3.1: A concept figure of the spreading lithosphere over the asthonesphere. The Oceanic lithosphere is generated at the mid ocean ridge and melted at the subduction zone. As the lithosphere moves towards the subduction zone and gets cooler, it gets thicker. When the density of the lithosphere reach a certain point, it descends into the subduction zone.

3.2 Present-day and Fossil Spreading Directions

Hotspots lie in the interior of a plate, usually far away from the plate boundaries. It causes swelling and volcanism at the surface of oceanic lithosphere. Hawaii-Emperor seamount chain is the track of a hotspot with the motion of the Pacific plate. Figure

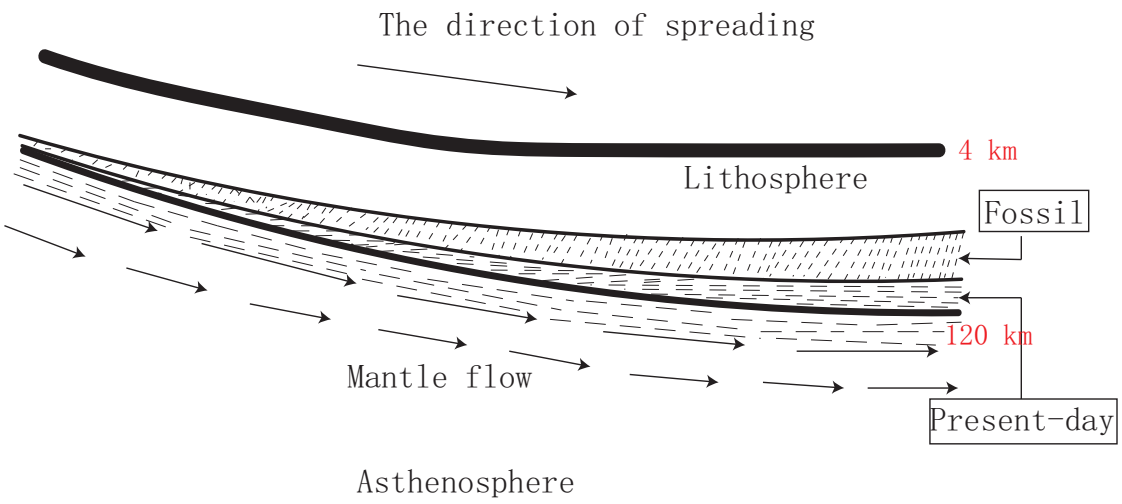

Figure 3.2: A concept figure of how anisotropic mantle rocks are formed: As the lithosphere cools down, the anisotropic mantle flows are added to the bottom of the lithosphere. We assume that the olivine in the mantle flow has a certain pattern of anisotropy. When the asthenosphere gets solidified, such anisotropy is "frozen" at the lithosphere. The lowest layer represents for the present-day anisotropy and the layer above that is formed at an earlier time.

3.3 is a concept figure to show the geography of the seamount chain. Hawaii-Emperor seamount chain starts at Kilauea volcano on the island of Hawaii and ends up near Aleutian Islands. The geological age of the chain of seamount increases linearly with distance from Kilauea volcano. At around 43 Myrs ago, the direction of plate motion shifted suddenly, which accounts for the turning point in the seamount chain. The oldest age in Emperor seamount chain is 82 Myrs.

The current direction of the Pacific plate motion is around $-56.6°$ or $123.4°$ according to Gripp and Gordon(2002), with an error of $6.3°$. The fossil direction of the Pacific plate motion is around $76°$ according to Searle et al.(1993). Searle et al. figured out the fossil plate motion by measuring the orientation of Molokai Fracture Zone near Hawaii. Here we can also measure the direction of these fracture zones near Hawaii in google Earth. We use the ruler tool in Google Earth to measure the azimuth of each

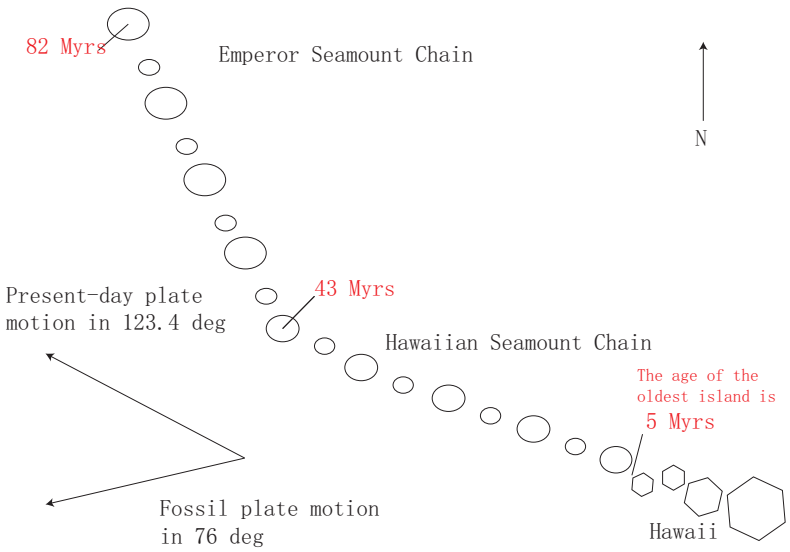

Figure 3.3: A concept figure of Hawaiian-Emperor seamount chain: the hexagons in the right bottom corner shows the islands in Hawaii. The age of the oldest island is around 5 Myrs. At the kink of Hawaiian-Emperor seamount chain, the age is 43 Myrs. The oldest age in Emperor seamount chain is 82 Myrs.

single fracture and take the average of seven to ten fractures to get the value of fossil plate motion direction.

The direction of plate motion changed at 43 Myrs ago. As illustrated before, the mantle flow that is driven by plate motion can give rise to anisotropy in the lithosphere. However, the pattern of anisotropy was changed at 43 Myrs ago when the direction of plate motion shifted. Thus the shallow layer represents the fossil spreading direction and the deeper layer indicates the present-day spreading direction(From 43 Myrs ago to present). Figure 3.4 shows how the layer of fossil spreading direction and the layer of present-day spreading direction are formed in the lithosphere. Without considering the effect of mantle plume, this medium only has two anisotropic layers. Above the anisotropic layer, there is a isotropic layer which is consist by the crust and the isotropic upper mantle. The first anisotropic layer is formed by ancient mantle flow. The present-day anisotropic layer is consist of lower lithosphere with a different orientation of anisotropy

and a layer of asthenosphere. The asthenosphere right beneath the lithosphere is dragged by plate spreading. So it is also anisotropic but the thickness of this layer still needs to be studied. Surface waves with high frequencies are sensitive to relatively shallow anisotropic medium which correlates to fossil spreading directions. Surface waves with low frequency are sensitive to deeper anisotropic medium(associated with the present-day spreading direction) but they can also be influenced by shallow medium as well. In a lateral homogeneous medium, we can expect that the parameters of fast direction and the strength of anisotropy change gradually from the values in the fossil mantle flows to the values in present-day mantle flows. That is the origin of the frequency dependency of the fast direction and the strength of anisotropy.

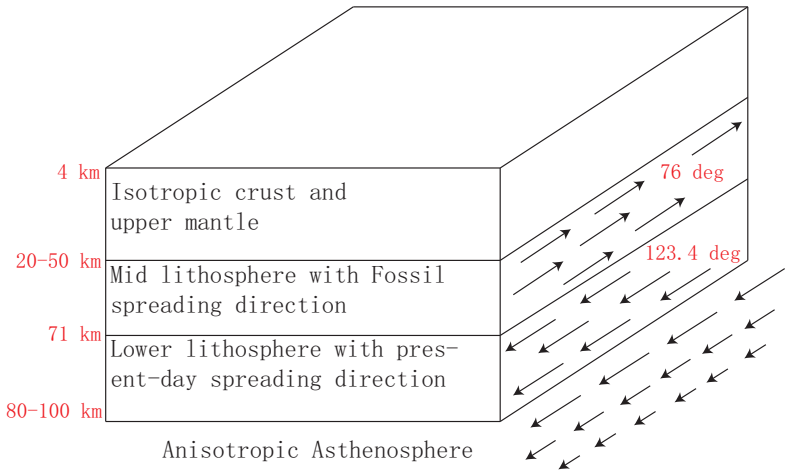

Figure 3.4: Geometrical relationship of the layer of fossil plate motion and the layer with present-day plate motion.

Before forward modeling, we need to identify a model in which only two layers are anisotropic. Figure 3.5 shows a concept of this model. This model is consist of six layers. The two layers for fossil spreading direction and present-day spreading direction are anisotropic. And the rest of four layers are all isotropic. We use a Fortran program to model the frequency dependency of fast direction and the strength of anisotropy. Then

we can compare the results with the data in Chapter 4.

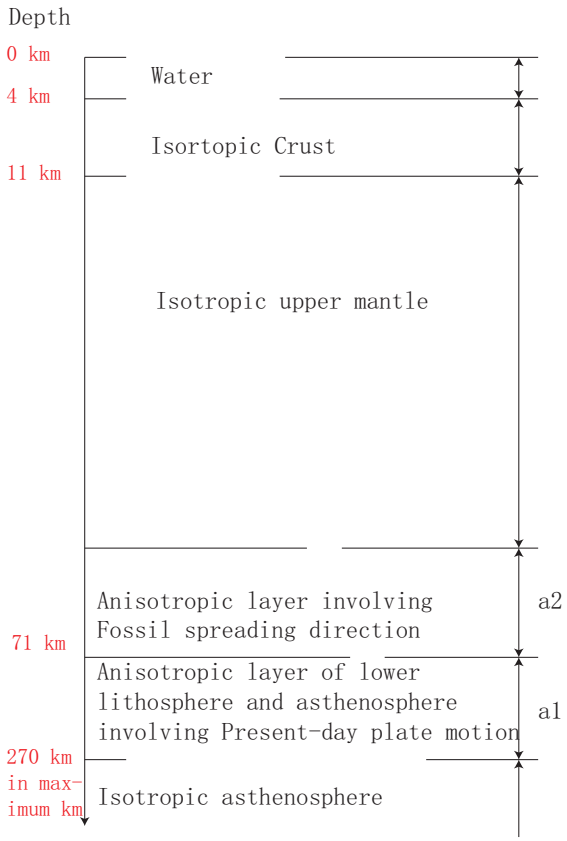

Figure 3.5: A concept figure of a six-layer model. Only the layer a1 and a2 are anisotropic.

3.3 The Hawaiian Mantle Plume

Hawaiian mantle plume is isolated from any plate boundary and it is less complex to studying the cause of the hotspot volcanism in Hawaii than in other places. Since it is located in the middle of the Pacific Plate, we are able to collect seismic arrivals in all directions surrounding it. However, the deep ocean floor around Hawaiian are regarded as the most significant obstacle for any previous studies in the collection of seismic observation.

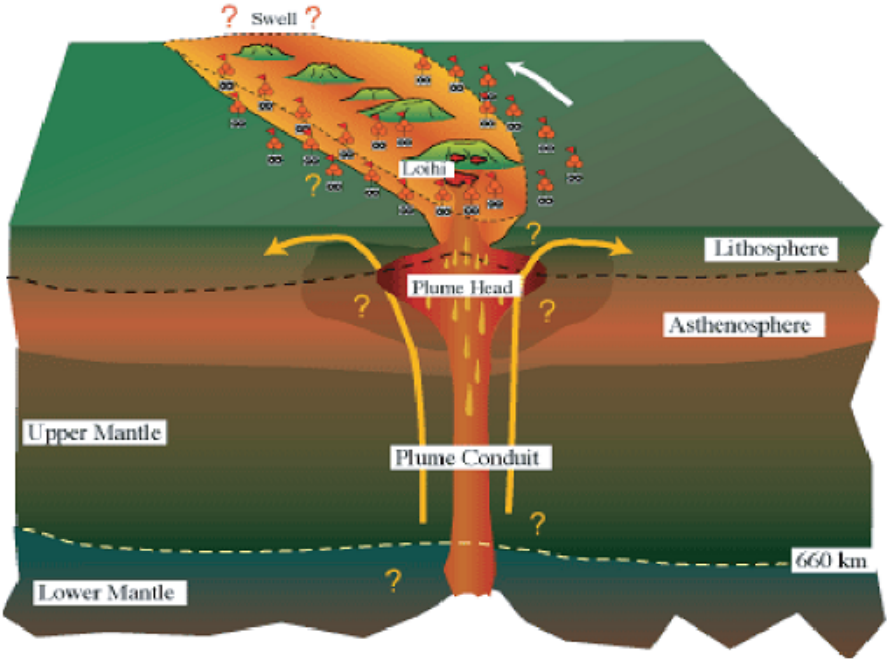

Figure 3.6: This Diagram shows a concept of mantle plume hypothesis with a conduit rising through the mantle and lithosphere, causing volcanism and forming the island. (https://igppweb.ucsd.edu/∼gabi/plume.html)

There are two models explaining the origin of hotspots. The plume theory (Wilson, 1963; Morgan, 1971) proposes that Hawaiian volcanism is the consequence of hot buoyant mantle flow that rises to the rigid lithosphere. Some hypothesis indicate that the mantle plume might originates from the core-mantle boundary. When approaching the surface, the mantle flow cause swelling on the lithosphere as well as volcanism in Hawaii. The location of the mantle plume is stationary but the plate is moving steadily. During this process, a chain of islands is formed with the motion of the plate. Figure 3.6 shows a concept of how this works. The other theory about hotspot is the Propagating crack theory (Jackson and Shaw, 1975). Propagating crack theory hypothesizes a crack in the lithosphere that allows mantle flows go through. In this theory, the hotspots only occur where there is a crack on the plate. And the mantle has a passive role in hotspot

dynamics with respect to a initiative role in the Plume theory.

A heterogeneity of anisotropy can be modeled by the plume theory (Wilson, 1963; Morgan, 1971) since the fast directions of anisotropy are always determined by the spreading direction of mantle. As shown in figure 3.7, the fast directions of anisotropy at different locations have a parabolic shape. This model is explained by figure 3.8 which provides a concept about how the orientations of fast directions of a plume interact with that of a spreading plate. The model of anisotropic medium is expected to be verified by the azimuthal anisotropy we measured.

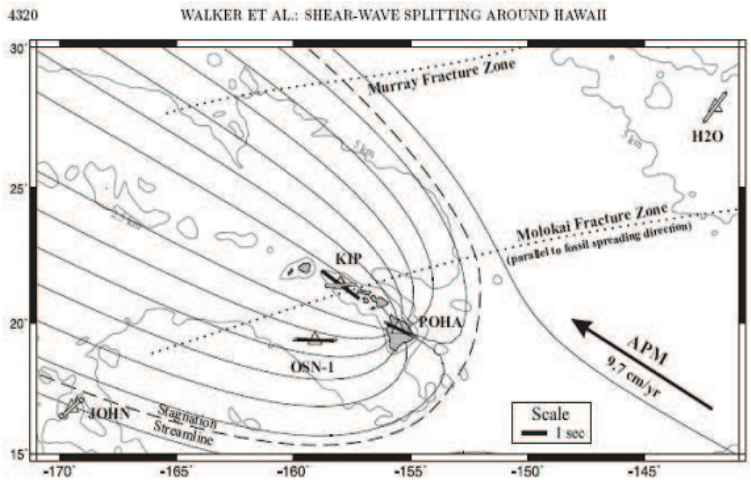

Figure 3.7: The figure shows the shear wave splitting around Hawaii as well as flows lines in the mantle.(Walker et al., 2001)

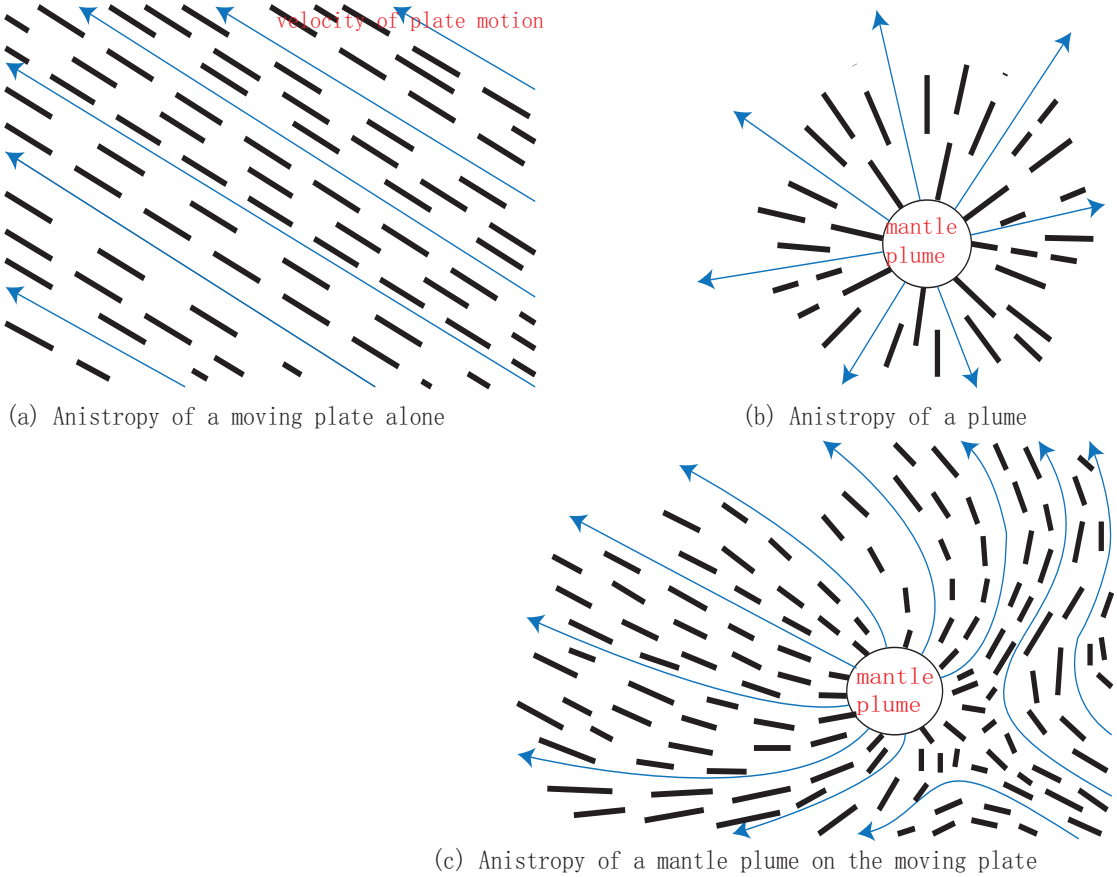

(a) Anistropy of a moving plate alone

(b) Anistropy of a plume

(c) Anistropy of a mantle plume on the moving plate

Figure 3.8: The blue lines with arrows are the flow lines, the black short lines shows the fast directions of anisotropic medium. Panel (a) shows a homogeneous anisotropic medium in a plate spreading with a steady velocity. Panel (b) shows the anisotropy caused by a mantel plume in a stationary plate. Panel (c) shows a realistic model of mantle plume. It is a mantle plume with a stationary location, which is dragged by a moving plate.

Chapter 4

Rayleigh Wave Azimuthal Anisotropy at Hawaii

4.1 The PLUME Project

The Hawaiian Plume-lithosphere Undersea Mantle Experiment(PLUME) is a multidisciplinary program. Data are collected from a large network of four-component broadband ocean bottom seismometers(OBS) and three-component portable broadband land stations. Figure 4.1 shows the locations of all seismic stations. Because of a wide range of seismic observation covering the sea floor around the Hawaiian mantle plume, the PLUME project is able to provide a 3-D tomographic image of Hawaiian plume in the lower and upper mantle. And a full range of seismic techniques has been applied in land-deployed experiments.

However, in this study, we only use the WHOI OBS stations. Figure 4.2 shows the 38 stations we are using and the 27 triangles formed by them.

We use Rayleigh waves to study Hawaiian mantle plume in the upper mantle. Since surface waves have a strong frequency dependence, a specific frequency is sensitive to a range of depth. As stated in Chapter 1, surface waves in different frequencies can be used to retrieve information at different depths. According to Chojnacki and Laske's study (2011), the velocity differences can be as small as 2% when measuring anisotropy. Surface waves are also the strongest arrivals on seismograms. Thus, it is easier to be distinguished from background noise and provided higher signal to noise ratio.

4.2 PLUME Instrument

Since the wave length of Rayleigh wave we are measuring is 10-60 mHz, we use a network of four-component broadband ocean bottom seismometers(OBSs) and three-component portable broadband land stations. The OBS network included 72 sites occupied in two phases by 73 instruments that were provided by the Woods Hole Oceanographic Institution (WHOI) and the Scripps Institution of Oceanography (SIO), both of which are institutional operators of OBSIP. The Carnegie Institution of Washington (CIW) operated the 10 land stations. An inner OBS network of 35 sites was deployed around the island of Hawaii and recorded continuously from January 2005 through January 2006 (phase 1). An outer OBS network of 37 sites covered the entire swell around the island chain and recorded from April 2006 through June 2007 (phase 2).

WHOI instruments were equipped with Güralp CMG-3T sensors (orthogonal components; $-$3-decibel corner period of the instrument response is at 120 seconds). The SIO instruments featured a Nanometrics Trillium-40 (symmetrical triaxial components, $-$3-decibel corner period at 40 seconds) during phase 1 and a Trillium-240 ($-$3-decibel

corner period at 240 seconds) during phase 2.

4.3 Rayleigh Wave Azimuthal Anisotropy

In this chapter, we first introduce a least square method to fit the azimuthal dependent data to equation 9 in chapter 2. The least square fit is applied to a set of synthetic data to test the effectiveness of this method. Then we simply apply the least square fit to a set of data recorded at 50 mHz regardless of the error bars. We test the impact of small errors after introduce a weighted least square fit. A few different ways to optimize the over weighing of small errors are discussed from section 4.5 to section 4.7. Finally we apply the most favorable method to other sets of data recorded at 10 mHz, 15 mHz, 20 mHz, 25 mHz, 30 mHz, 35 mHz, 40 mHz and 45 mHz. This chapter is aimed at processing the data of azimuthal dependent phase velocity and find out an appropriate method to be used.

Assuming we have a set of data with phase velocity c with respect to azimuth ψ, we fit the data set with a linear equation which express an azimuthal dependence of phase velocity:

$$c = A_1 + A_2\cos(2\psi) + A_3\sin(2\psi) + A_4\cos(4\psi) + A_5\sin(4\psi) \tag{4.1}$$

In order to solve the linear equations:

$$c_1 = A_1 + A_2\cos(2\psi_1) + A_3\sin(2\psi_1) + A_4\cos(4\psi_1) + A_5\sin(4\psi_1)$$

$$\ldots\ldots\ldots\ldots\ldots\ldots\ldots\ldots\ldots\ldots\ldots\ldots$$

$$c_j = A_1 + A_2\cos(2\psi_j) + A_3\sin(2\psi_j) + A_4\cos(4\psi_j) + A_5\sin(4\psi_j)$$

$$\ldots\ldots\ldots\ldots\ldots\ldots\ldots\ldots\ldots\ldots\ldots\ldots$$

$$c_{113} = A_1 + A_2\cos(2\psi_{113}) + A_3\sin(2\psi_{113}) + A_4\cos(4\psi_{113}) + A_5\sin(4\psi_{113}) \quad (4.2)$$

we use a least square method to find out a set of coefficients A_1, A_2, A_3, A_4, A_5, and now we denote them as a model vector **m**. Assume **d=Gm**, where **d** is a M dimensional vector, **m** is a N dimensional vector. **G** is a $M \times N$ matrix.(In this case, M=113, N=5)

$$\mathbf{d} = [c_1, \ldots, c_j, \ldots, c_{113}]^T \quad (4.3)$$

$$\mathbf{G} = \begin{bmatrix} 1 & \cos(2\psi_1) & \sin(2\psi_1) & \cos(4\psi_1) & \sin(4\psi_1) \\ \ldots\ldots\ldots\ldots\ldots\ldots\ldots\ldots & & & & \\ 1 & \cos(2\psi_j) & \sin(2\psi_j) & \cos(4\psi_j) & \sin(4\psi_j) \\ \ldots\ldots\ldots\ldots\ldots\ldots\ldots\ldots & & & & \\ 1 & \cos(2\psi_{113}) & \sin(2\psi_{113}) & \cos(4\psi_{113}) & \sin(4\psi_{113}) \end{bmatrix} \quad (4.4)$$

$$\mathbf{m} = [A_1, A_2, A_3, A_4, A_5] \quad (4.5)$$

In a least square fit, we find a solution of **m** to minimize the sum of the square of every modeled misfit.

The misfit of the i-th equation is defined as: $d_i - \sum_{j=1}^{N} G_{ij} m_j$

Our objective function is:

$$E = \sum_{i=1}^{M} (d_i - \sum_{j=1}^{N} G_{ij} m_j)^2 \quad (4.6)$$

To minimize the objective function, we calculate the model vector as:

$$\mathbf{m} = [\mathbf{G^T G}]^{-1}\mathbf{G^T d} \tag{4.7}$$

The Matlab script is shown as following:

```
m=[G'*G]\G'*d;
%where "\" means inversion of a matrix on the left side of this symbol.
%symbol " ' " means the transpose of a matrix.
```

4.4 Exploring Equation 20

Before using real data, this method is first applied to a set of synthetic data, it is a blind test. We use a set of synthetic data generated by an unknown model vector **m**. Then a linear inversion as equation 4.7 is applied to the synthetic data. The result of a least square fit is shown in table 4.1:

Table 4.1: results of the inversion of synthetic data

parameter	4ψ	2ψ
A_1	2.0000	2.0000
A_2	3.0000	3.0000
A_3	4.0000	4.0000
A_4	0.5000	No
A_5	0.5000	No
MF	0	0.25
VR	100%	98%

Where misfit is denoted as MF,

$$MF = \frac{1}{N}\sum_{N}(d_{oi} - d_{pi})^2 \tag{4.8}$$

d_{oi} is the observed datum, d_{pi} is the predicted datum. Variance reduction is denoted as VR,

$$
\begin{aligned}
VR &= (1 - \frac{Var_2}{Var_1}) \times 100\% \\
Var_2 &= \frac{1}{N-1} \sum_i (d_{oi} - d_{pi})^2 \\
Var_1 &= \frac{1}{N-1} \sum_i (d_{oi} - \bar{d})^2
\end{aligned} \tag{4.9}
$$

d_{oi} is the observed datum, d_{pi} is the predicted datum, $\bar{d}$ mean of observed data.

Misfit measures how well the data are fitted to a predicted curve, the smaller the misfit is, the better a inversion is. Variance reduction is a percentage which also shows how well fit a inversion has done. A 100% variance reduction means the predicted data after inversion is perfectly fitted to the observed data.

We compare the results with the initial input model vector of synthetic data and find that: (1) The result of 4ψ fit is consistent with the input model vector which shows the validity of this method(all the five parameters are the same). Figure 4.3 shows a plot of synthetic data and its least square fit. The curve of 4ψ fit perfectly modeled the synthetic data since the misfit(MF) is 0. The variance reduction(VR) of the inversion is 100% because the synthetic data and modeled data are exactly the same. (2) Obviously the result of 2ψ fit can not match the synthetic data because the input model vector has two more parameters. The curve of 2ψ fit is inconsistent with synthetic data and the misfit is 0.25. The variance reduction is 98% though is does not have much meaning as we have already known the synthetic data has a 4ψ term.

4.5 An inversion Using Real Data (assuming no data error)

This sample data is an azimuthal dependency of Rayleigh wave phase velocity including 113 data points. We get the data from triangle 2 (see figure 4.4) and the data is recorded at 50 mHz(Courtesy of Gabi, 2016). We apply the same technique with the example of synthetic data in last section assuming no data error. The result are shown in table 4.2

Table 4.2: Results of the inversion for real data (assuming no data error)

parameter	4ψ	2ψ
A_1	3.9662	3.9698
A_2	-0.0465	-0.0495
A_3	0.0641	0.0675
A_4	0.0017	No
A_5	-0.0386	No
MF	0.0312	0.0320
VR	12.62%	10.55%
SA	4.74%	4.22%
DIR	67°	63°

Two major parameter in this experiment that we are really interested are strength of anisotropy and fast direction. These two parameter measure the characteristics of an anisotropic medium. We define the strength of anisotropy as: $SA = \frac{C_{max} - C_{min}}{C_0} \times 100\%$, where C_{max} is the maximum phase velocity and C_{min} is the minimum phase velocity, and $C_0 = A_1$ is an average of phase velocity. The parameter DIR is the fast direction of anisotropy. Fast direction is the azimuth at which degree the predicted curve goes to its summit. Note that the azimuth should be from 0° to 90°. We calculate phase velocity at different azimuth with an increment of 1° before manually picking up one azimuth which maximizes the phase velocity. We get a fast direction at 67° in 4ψ fit

and at 63° in 2ψ fit. Also, the strength of anisotropy in 4ψ fit (4.74%) is stronger than that in 2ψ fit (4.22%). To estimate the effectiveness of inversion of 4ψ fit and 2ψ fit, we compare the misfit(MF) and the variance reduction(VR) of the 4ψ and 2ψ fit. We find that a 2ψ fit has a slightly larger MF but smaller VR than 4ψ fit, which means 4ψ fit should be more effective. The result of the least square fit is shown in figure 4.4, a 2ψ fit roughly depicts the trend of data point and the 4ψ fit does not seem to be a better fit.

4.6 An Inversion Using Real Data (weighted by error bars)

In this section, we weight the data with its error bar before apply an inversion. Specifically, every row of matrix G and vector d are multiplied by their corresponding one over error bar. For example,

$$[G_{11}, G_{12}, G_{13}, G_{14}, G_{15}] \times \frac{1}{error_1} \text{ and } d_1 \times \frac{1}{error_1}$$

The result are shown in table 4.3:

Table 4.3: Results of the weighted least square fit (weighted by error bars)

parameter	4ψ	2ψ
A_1	4.0087	4.0099
A_2	-0.1333	-0.1381
A_3	0.0806	0.0661
A_4	0.0349	No
A_5	-0.0084	No
MF	41.2	45.2
VR	77.85%	75.69%
SA	8.28%	7.63%
DIR	80°	77°

In a weighted least square fit, the expression for MF and VR changes a little:

$$MF = \frac{1}{N}\sum_{N}(\frac{d_{oi}-d_{pi}}{\sigma_i})^2 \tag{4.10}$$

d_{oi} is the observed datum, d_{pi} is the predicted datum, σ_i is the error.

$$\begin{aligned} VR &= (1-\frac{Var_2}{Var_1})\times 100\% \\ Var_2 &= \sum_{N}(\frac{d_{oi}-d_{pi}}{\sigma_i})^2/(\sum_{N}\frac{1}{\sigma_i^2}) \\ Var_1 &= \sum_{N}(\frac{d_{oi}-\bar{d}}{\sigma_i})^2/(\sum_{N}\frac{1}{\sigma_i^2}) \end{aligned} \tag{4.11}$$

σ_i is the error, Var_1 is the initial variance, Var_2 is the modeled variance.

Figure 4.5 shows the result of the least square fit. The MF of 4ψ fit is 41.2 and the MF of 2ψ fit is 45.2. However, VR of 4ψ fit is 77.85% ans VR of 2ψ fit is 75.69%. The MF of 4ψ fit is smaller and the VR of 4ψ fit is larger. Consequently, in a weighted least square fit, a 4ψ fit is slightly more effective. It is reasonable that we get a little different fit if we add two more parameters. The strength of anisotropy are 8.28% for 4ψ fit and 7.63% for 2ψ fit, which are almost twice the value of least square fit without error bar. The fast directions are 80° and 77° for 4ψ fit and 2ψ fit respectively, which are also different from the previous least square fit. Both the fast direction and the strength of anisotropy have significant difference with the values obtained from the last section(assuming no data error). This means both results are not convincing before further evaluation. In the next step, we explore how small errors influence the results, and distort the inversion.

In the form of matrix, we also apply a weighted least square fit using the same method. Then a $M \times M$ weight matrix $\mathbf{w}$ is introduced. The weight matrix $\mathbf{w}$ only has none-zero value at its diagonal components which are defined by $\frac{1}{error^2}$.

$$\mathbf{w} = \begin{pmatrix} \frac{1}{error1^2} & & & \\ & \frac{1}{error2^2} & & \\ & & ..... & \\ & & & \frac{1}{error113^2} \end{pmatrix} \tag{4.12}$$

Analogous to the formula previously used, the a weighted least square fit is expressed as:

$$\mathbf{m} = [\mathbf{G^T w G}]^{-1}\mathbf{G^T w d} \tag{4.13}$$

The Matlab script is:

```
m=[G'*w*G]\G'*w*d;
```

The result are identical.

4.7 An Experiment with 12 'best' data

(a) Only use 12 data with smallest error, the plots of 2ψ and 4ψ fit are shown in figure 4.6 and the results are also shown in table 4.4:

With only 12 data, the misfit of 4ψ fit is 253.99 and the misfit of 2ψ fit is 290.99. Both misfits are much more larger than weighted least square fit, which means the 12 data can not be regarded as 'best' data at all though they have relatively small data error. One

Table 4.4: Results of the inversion using 12 data

parameter	4ψ	2ψ
A_1	4.0205	4.0170
A_2	-0.1542	-0.1511
A_3	0.0755	0.0664
A_4	0.0403	No
A_5	-0.0018	No
MF	253.99	290.07
VR	83.76%	81.45%
SA	9.12%	8.22%
DIR	84°	79°

possibility is that the small numbers of error bars are not convincing and we can't take the error bars as the only evidence to weight the data. Moreover, the results of variance reduction and strength of anisotropy are both close to those from weighted least square fit, which indicates that a few data points with relatively smaller error can dominate the weighted least square fit. Since we weight the data with $1/error$, if the some of the data points are not as precise as we expected, these data can dominate the inversion. Consequently, most of the other data with relatively larger error bars are meaningless in an inversion. As we need to take advantages all the data and prevent ourselves from wasting any useful informations, we will improve this least square fitting.

(b) Using the rest of 101 data, a plot of 2ψ fit and 4ψ fit is shown in figure 4.7 and the results are shown in table 4.5:

Compared with 12-data fit, the misfit gets smaller, and even smaller than weighted least square fit in section 4.3. If we remove the differences in algorithm of non-weighted and weighted least square fit, the misfit of this test without 12 data is very close to the result from non-weighted least square fit. That further convinces us that the small errors dominate the inversion and cause higher misfit. The rest of 101 data points do not have

Table 4.5: Results of the inversion using 101 data

parameter	4ψ	2ψ
A_1	3.9941	3.9911
A_2	-0.0735	-0.0782
A_3	0.0670	0.0573
A_4	0.0327	No
A_5	-0.0056	No
MF	11.41	11.87
VR	47.43%	45.32%
SA	5.77%	4.86%
DIR	80°	73°

much impact on the inversion compared to the 12 data with smallest error. In this test, the fast directions of 4ψ fit and 2ψ fit are still larger than non-weighted least square fit in section 4.2 though we expect they should not be. Most importantly, the strength of anisotropy is close to the results in section 4.2. Additionally, even we remove some of the data with smallest error, we still can not make every data point fit the curve. Because there some data which have the same azimuth but different phase velocity. Those data are called internally inconsistent data.

4.8 A Test With Various Threshold of Minimum Data Errors

In the previous sections, we learn that small errors can highly influence the results of an inversion. Now we introduce a threshold to constrain the minimum available errors. Practically, if an error is smaller than the threshold, then we replace the error with the threshold. The results are shown as MF, VR, SA, DIR as functions of various thresholds. Figure 4.8 and table 4.6 show the results for the 4ψ fit.

Figure 4.9 and table 4.7 show the results for the 2ψ fit.

Table 4.6: A test with different threshold for the 4ψ fit

threshold	0.01	0.02	0.05	0.1	0.15	0.2	0.5	1.0	1.5
MF	20.48	12.35	5.41	2.33	1.19	0.74	0.14	0.04	0.03
VR	61.62	46.43	25.94	12.43	11.16	10.49	11.13	12.48	12.62
SA	7.46	6.63	5.07	4.30	4.11	4.15	4.21	4.68	4.74
DIR	79	74	69	62	63	63	65	67	67

	threshold of 0.01	weighted with no error threshold	omit 12 'best' data	12 'best' data
MF	20.48	41.2	11.41	253.99
VR	61.62	77.85	47.43	83.76
SA	7.46	8.28	5.77	9.12
DIR	79	80	80	84

Table 4.7: A test of different threshold for 2ψ fit

threshold	0.01	0.02	0.05	0.1	0.15	0.2	0.5	1.0	1.5
MF	21.98	13.02	5.50	2.35	1.20	0.76	0.14	0.04	0.03
VR	58.82	43.55	24.70	11.97	10.25	8.86	9.39	11.46	10.54
SA	6.96	6.28	5.12	3.90	3.66	3.49	3.87	4.19	4.21
DIR	76	71	68	66	65	64	64	64	64

	threshold of 0.01	weighted with no error threshold	omit 12 'best' data	12 'best' data
MF	21.9809	45.2	11.87	290.07
VR	58.82	75.69	45.32	81.45
SA	6.96	7.63	4.86	8.22
DIR	76	77	73	79

In figure 4.8, the misfit keeps declining as the threshold grows. However, in the plot of variance reduction, strength of anisotropy and fast direction, there is an unexpected trend that the curves decline when the threshold is smaller than approximately 0.2. After that, the curves appear to approach the results from the non-weighted least square fitting in section 4.2 (plotted in red lines). For comparison, results from the 2ψ fit of the non-weighted least square fit are plotted as green lines. As what we can see from table 4.6, SA is 7.46% for the 4ψ fit when we set a small threshold as of 0.01. The value is smaller than the case of no error threshold(8.28%) and the case of 12 'best'

data(9.12%). The fast direction is 76°, which is also smaller than the case of no error threshold(80°) and the case of 12 'best' data(82°). However, the fast direction of "omit 12 'best' data"(80°) is close to the result of no threshold(80°). But SA of "omit 12 'best' data"(5.77%) is close to the result of small threshold(5.07%). Such inconsistency may occur due to the involvement of a few erroneous data with unrealistically small error bars. One small error may not necessarily means a high accuracy. Since the fast direction and SA change significantly as the threshold increases, we need to guarantee the stability of these two parameter as we select the minimum error threshold. The range of practical thresholds is plotted as shadowed box in figure 4.8. We chose a threshold of 0.2 for example. In this condition, DIR stays within 2° to 3°. Likewise, the change of SA is around 0.1%.

4.9 A Test With Different Means of Definition of The Weight

Previously we use $w = \frac{1}{error}$ as the weight for an inversion. But we found that this type of the weight overemphasizes data with vary small error. Here explore a way to even out the the impact of changing error bars. We replace our weight $w = \frac{1}{error}$ with $w = \frac{1}{\sqrt{error}}$. The results for an inversion with no error threshold are in table 4.8.

Compared with the results from no error threshold in section 4.5, we get a smaller fast direction and smaller SA. That means a different weight function does contribute to down weigh the effect of small error bars. Nonetheless, we still can not remove completely the effect of some data with extremely small errors because we still do not get the results that we obtained for our 'best' choice of minimum error threshold. Thus,

Table 4.8: Results of the inversion (different definition of the weight)

	new weight		no error threshold		error threshold of 0.02	
parameter	4ψ	2ψ	4ψ	2ψ	4ψ	2ψ
A_1	3.9813	3.9900	/	/	/	/
A_2	-0.0908	-0.1067	/	/	/	/
A_3	0.0898	0.0756	/	/	/	/
A_4	0.0110	No	/	/	/	/
A_5	-0.0298	No	/	/	/	/
MF	11.41	11.87	41.2	45.2	0.74	0.76
VR	51.33%	48.99%	77.85%	75.69%	10.49%	8.86%
SA	6.61%	6.55%	8.28%	7.63%	4.15%	3.49%
DIR	70°	72°	63°	77°	63°	64°

setting a threshold of error is necessary.

4.10 Making a new data set by taking average of data in each 10°-bins

We divide the azimuth from 0° to 360° into 36 equal 10°-bins. In each bin, we take the value in center as the azimuth of this bin. We calculate the average of phase velocities in every bin as the phase velocity of the bin. And we calculate the standard deviation of phase velocities in each bin as the error of the bin. For some bins, there may be less than 3 data points, which should be abandoned from our experiment. We get one datum for each bin and perform a weighted least square fitting as stated before. The results are shown in table 4.9 and figure 4.10.

The result of SA for the 4ψ fit is 5.64%, which is larger than the shadowed box area(4%-5%) in figure 4.8 as we choose. SA for the 2ψ fit appears to be more reasonable since it stays in consistency with the results of the test using different threshold. DIR

Table 4.9: results of the inversion using 10°-bins

parameter	4ψ	2ψ
A_1	3.9718	3.9779
A_2	-0.0463	-0.0380
A_3	0.0899	0.0743
A_4	-0.0297	No
A_5	-0.0353	No
MF	1.175	1.345
VR	70.81%	66.59%
SA	5.64%	4.19%
DIR	58°	59°

for the 4ψ fit(58°) and the 2ψ fit(59°) is also a little smaller than the shadowed box area($60° - 65.5°$) in figure 4.8. But it should be acceptable.

4.11 The Inversion of Data Recorded At Different Frequencies

In this section, we apply the inversions to a few sets of data recorded at 10 mHz, 15 mHz, 20 mHz, 25 mHz, 30 mHz, 35 mHz, 40 mHz, 45 mHz. According to the previous sections, we select a minimum error threshold of 0.2 to conduct a weighted least square fit, we obtain a table(table 4.10) showing how FM, VR, SA, DIR change with respect to frequency. Also, figure 4.11 shows SA and DIR as functions of frequency. Results of 4ψ fit (red line) and 2ψ fit (blue line) are plotted in different colors.

It is of our expectation to see that the fast directions at low frequencies reach around 123.4°, which reflects the present-day direction of plate motion. It is acceptable that fast direction values at the lowest frequency from both the 4ψ fit and the 2ψ fit are smaller than present spreading direction because shallower medium also have a little

Table 4.10: Results of the inversion of data recorded at different frequencies

frequency(mHz)	10	15	20	25	30	35
MF(4ψ)	1.826	1.988	11.934	1.917	3.716	1.308
MF(2ψ)	182.6	234.6	1456	237.7	431.0	153.0
VR(4ψ)	22.51%	24.48%	31.20%	29.60%	28.03%	34.29%
VR(2ψ)	16.68%	23.51%	28.93%	23.96%	25.80%	31.86%
SA(4ψ)	5.76%	4.18%	4.83%	5.42%	4.92%	4.64%
SA(2ψ)	3.78%	4.31%	4.55%	4.66%	4.56%	4.75%
DIR(4ψ)	116°	94°	91°	96°	98°	82°
DIR(2ψ)	100°	90°	78°	84°	89°	78°

frequency(mHz)	40	45	50
MF(4ψ)	11.153	1.285	0.744
MF(2ψ)	1294	149.1	84
VR(4ψ)	33.56%	25.29%	10.49%
VR(2ψ)	27.61%	23.50%	8.87%
SA(4ψ)	5.07%	4.51%	4.15%
SA(2ψ)	4.89%	4.46%	3.49%
DIR(4ψ)	74°	73°	62°
DIR(2ψ)	74°	70°	63°

impact on fast direction at the lowest frequency. And the fast direction declines as the frequency increases. At the largest frequency, the value is around 60°. However, the fossil direction of plate motion is 76°. This is beyond our expectation. As for strength of anisotropy, the result of 4ψ fit varies between 5.7% to 4.2%. The curve of 2ψ fit is between 3.5% to 5%. Both of the parameters of SA and DIR have a strong dependency on frequency.

We process the data for all the other triangles (from 10 mHz to 60 mHz) in a similar way. Results of all the triangles (10 mHz, 20 mHz, 40 mHz, 50 mHz) are shown in figure 4.12. The results at 40 mHz on the top right panel and 50 mHz on the top left panel seem to be sort of coherent. Generally all the fast directions align with the fossil plate motion. At the north of the islands, the fast direction is particularly coherent and the strength of anisotropy is relatively large. In the south west, the strength

of anisotropy is relatively smaller. Both panels for 10 mHz and 20 mHz show strong incoherence. Lower frequencies can see current plate motion with shallower depth. At 20 mHz, the fast direction in the north of the islands aligns with the fossil plate motion. In contrast, the fast direction in the north of the islands is more similar to the current plate motion when the frequency is 10 mHz. The panel for 10 mHz shows increasing sensitivity to deeper structures. It shows strong anisotropy near the islands which is close to the current plate motion. In the south east, the symbols are coherent with the fossil plate motion which means the fossil anisotropic layer at here is deeper than anywhere else.

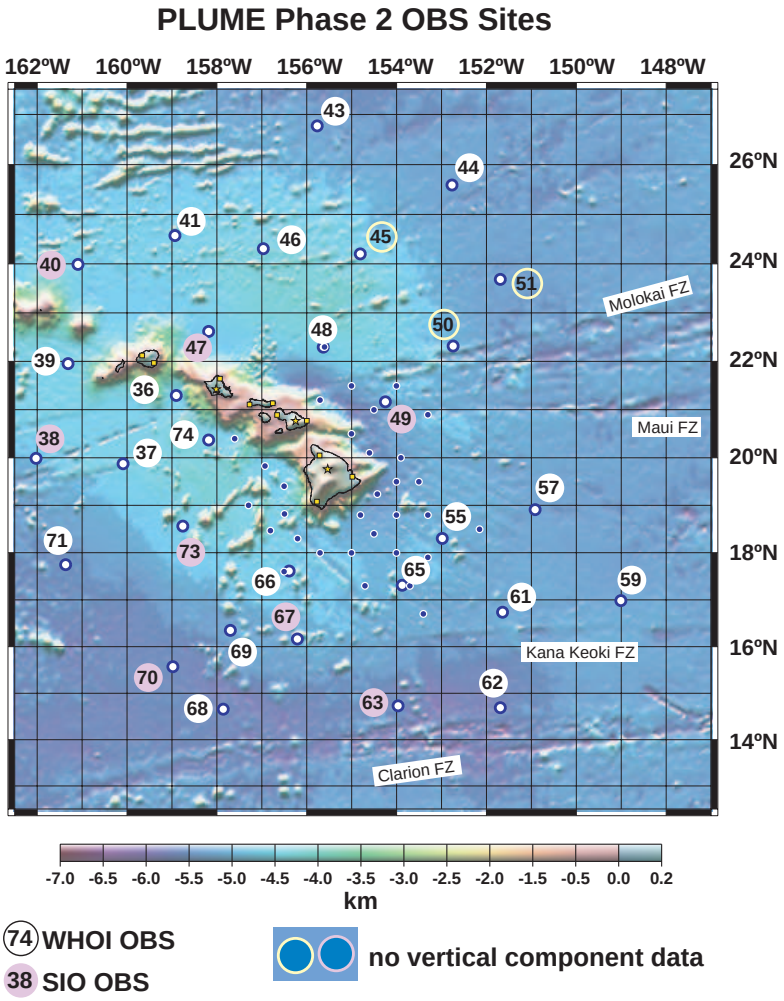

Figure 4.1: Site locations of the Hawaiian PLUME phase 2 deployment from April 2006 through May 2007 (Laske et al. 2011). Thirty OBSs were recovered. Of these, 8 OBSs from the Scripps Institution of Oceangraphy (SIO) and 19 OBSs from the Woods Hole Oceanographic Institute (WHOI) delivered data. In this study, we analyze the WHOI data only.

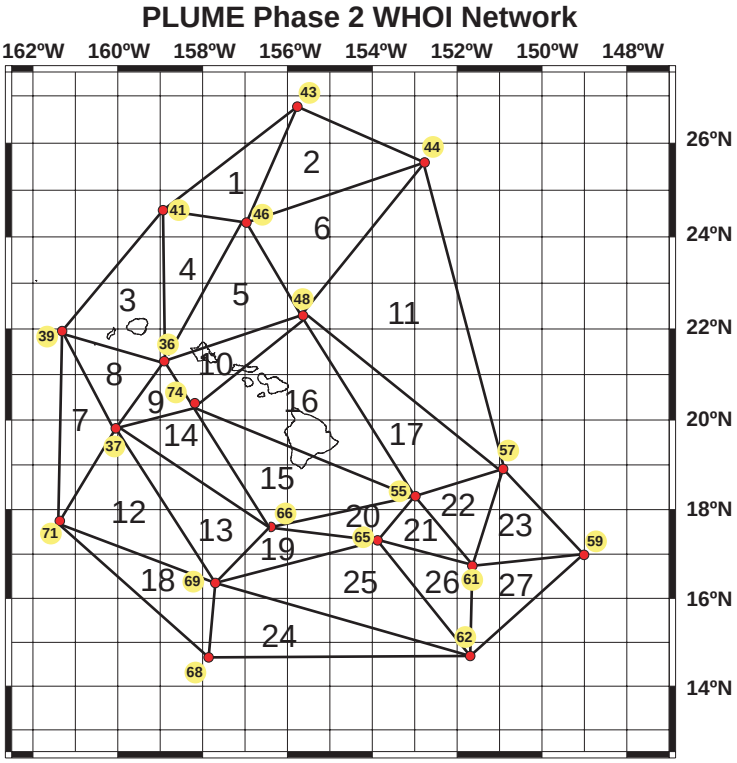

Figure 4.2: A map of 38 stations we are using, the stations are plotted with red dots and labeled with numbers. All these stations form 27 triangles just as labeled in the figure.(courtesy of Gabi Laske)

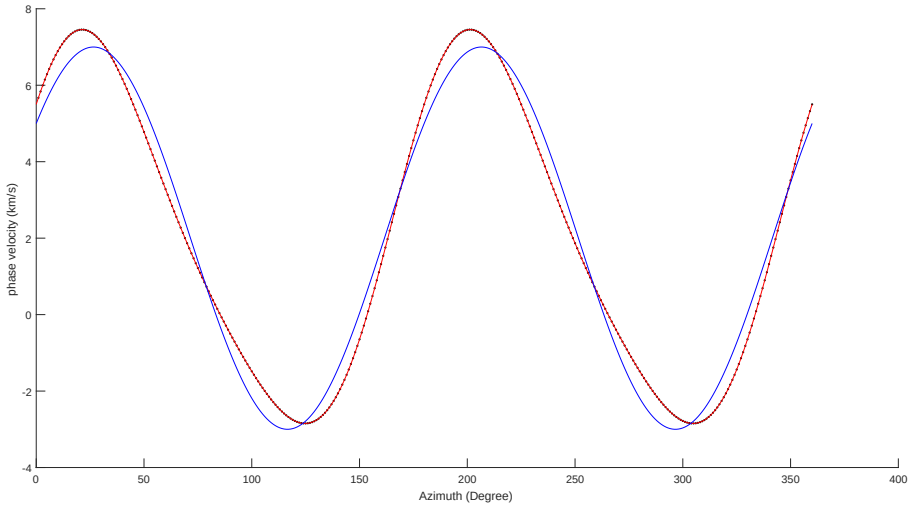

Figure 4.3: A plot of testing data: Black symbols show the synthetic data, red curve shows the 4ψ fit, blue curve shows the 2ψ fit. The curve for 4ψ fit (red line) is top of the symbols of synthetic data.

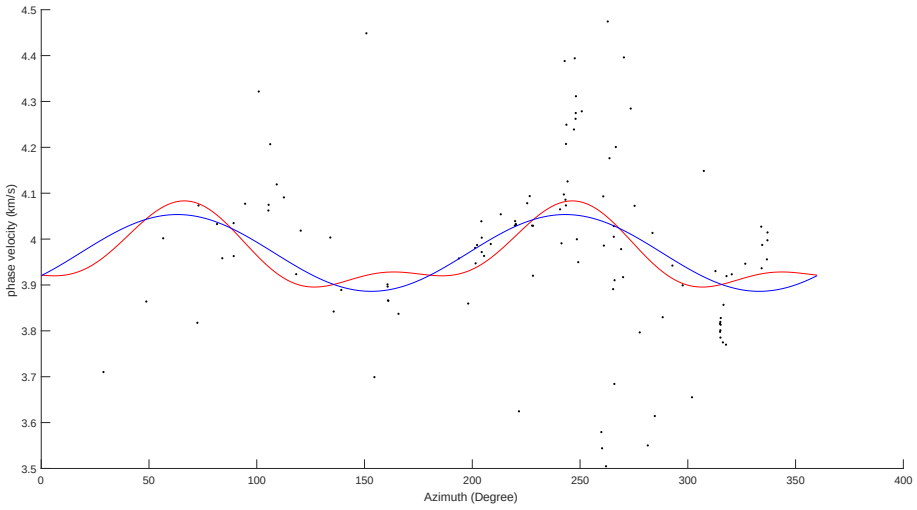

Figure 4.4: A plot of Azimuth-dependent phase velocity and a least square fit regardless of error bar: Black symbols shows the raw data, red curve shows the 4ψ fit, blue curve shows the 2ψ fit

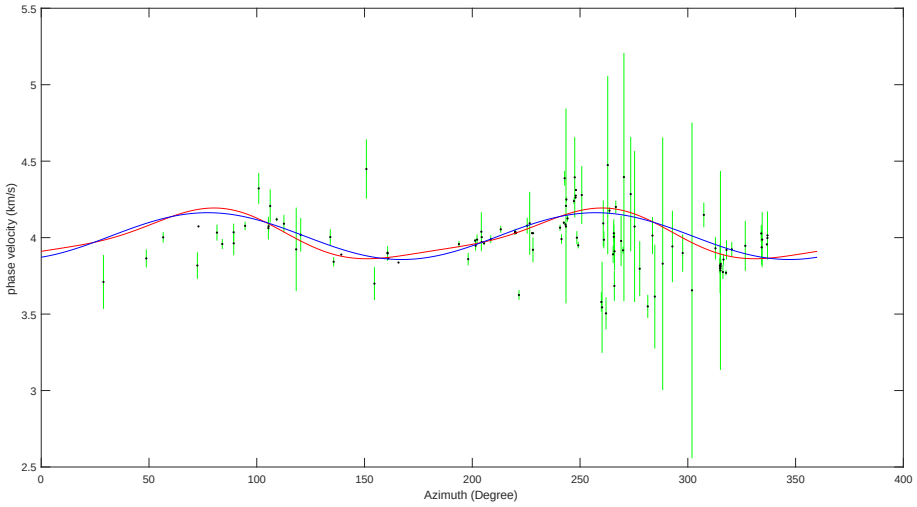

Figure 4.5: A plot of Azimuth-dependent phase velocity and a least square fit: Black symbols shows the raw data, red curve shows the 4ψ fit, blue curve shows the 2ψ fit

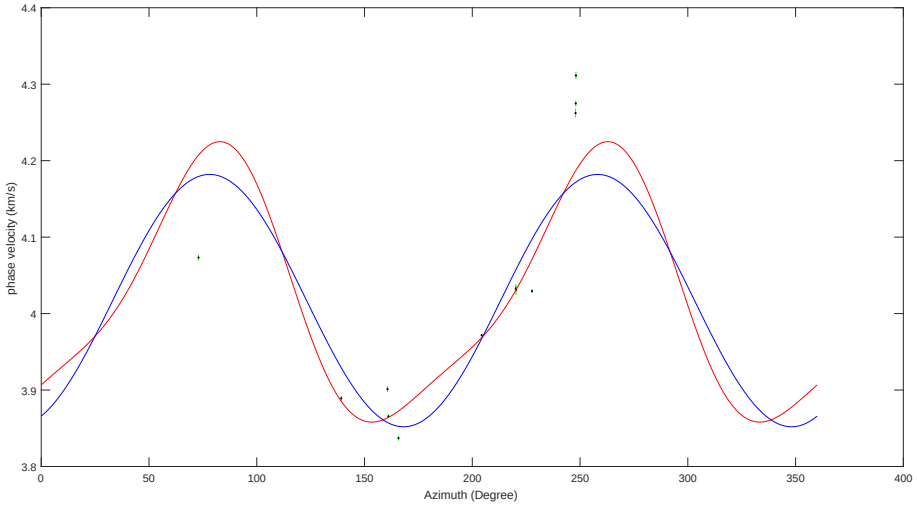

Figure 4.6: A plot of phase velocity as function of azimuth: Black symbols show the synthetic data, red curve shows the 4ψ fit, blue curve shows the 2ψ fit.

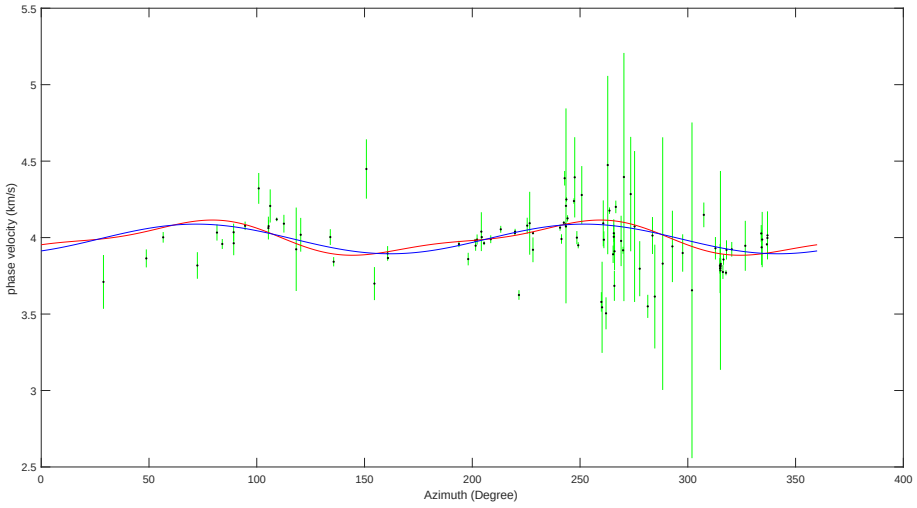

Figure 4.7: Phase velocity as function of azimuth: Black symbols show the synthetic data, red curve shows the 4ψ fit, blue curve shows the 2ψ fit.

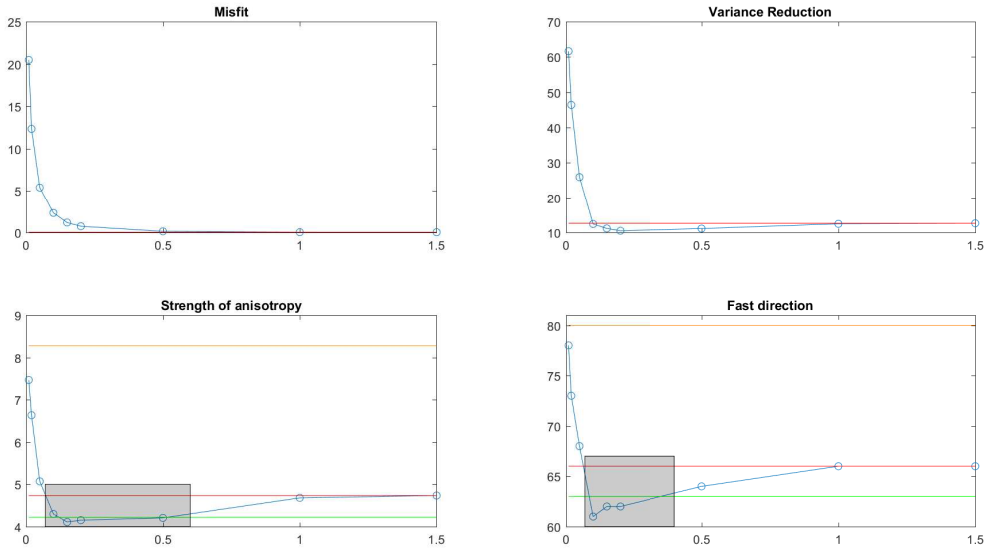

Figure 4.8: 4ψ fit: Plots of MF, VR, SA, DIR as functions of thresholds of data error(in blue line). 4ψ fit of non-weighted least square fit is plotted as horizontal red lines. 2ψ fit of non-weighted least square fit is plotted as horizontal green lines. Orange lines show the weighted least square fit without any error threshold. The shadowed box shows the practical range of error threshold.

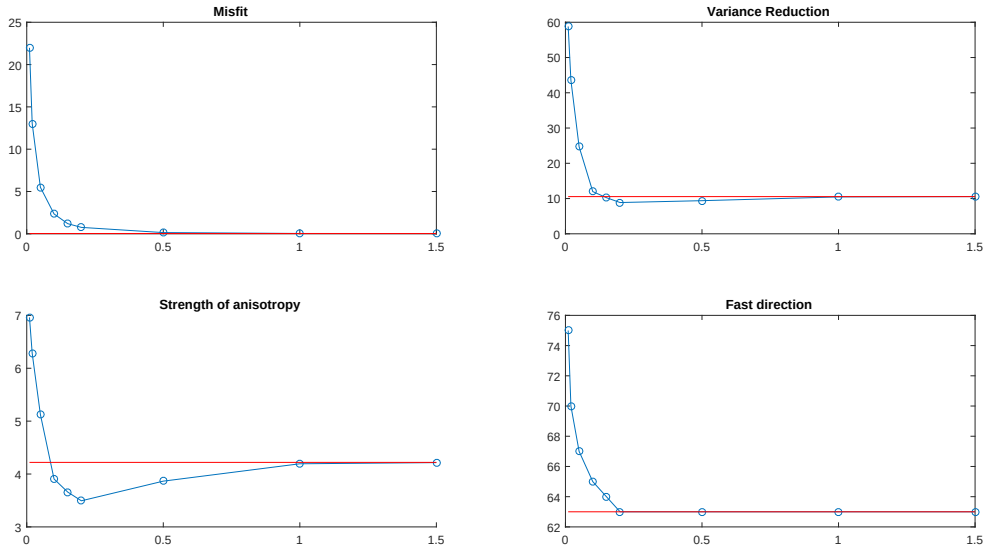

Figure 4.9: Same as figure 4.8 but for the 2ψ fit: Plots of MF, VR, SA, DIR as functions of thresholds of data error(in blue line). The results of non-weighted least square fit is plotted as horizontal red lines.

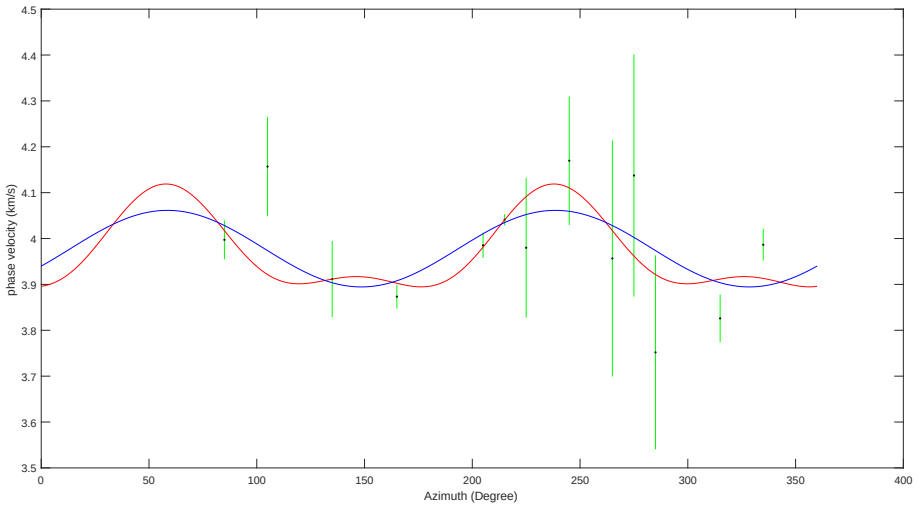

Figure 4.10: A plot of phase velocity as function of azimuth: Black symbols show the data points, red curve shows the 4ψ fit, blue curve shows the 2ψ fit.

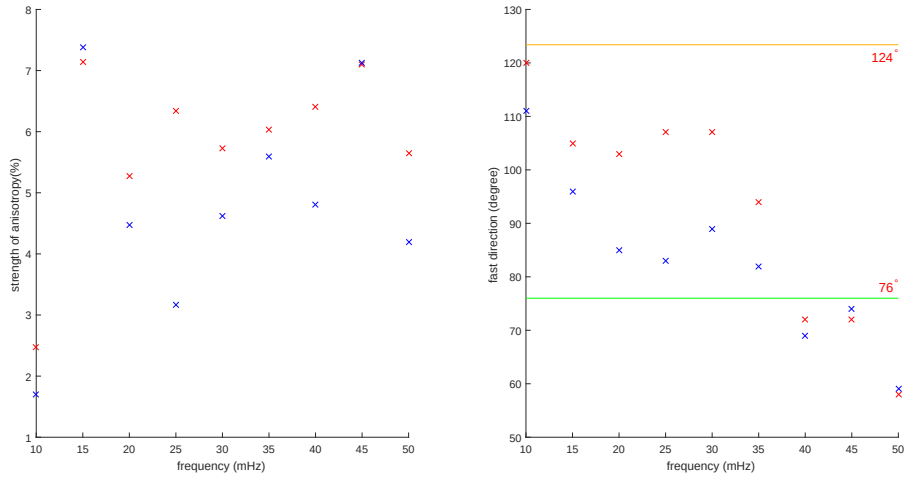

Figure 4.11: Final Data for Triangle 2: Strength of anisotropy(SA) as function of frequency is in the left panel, and Fast direction(DIR) as function of frequency is in the right panel. Red symbols show the 4ψ fit, blue symbols show the 2ψ fit. The orange horizontal line shows the present spreading direction(124°), the green line shows the fossil spreading direction(76°).

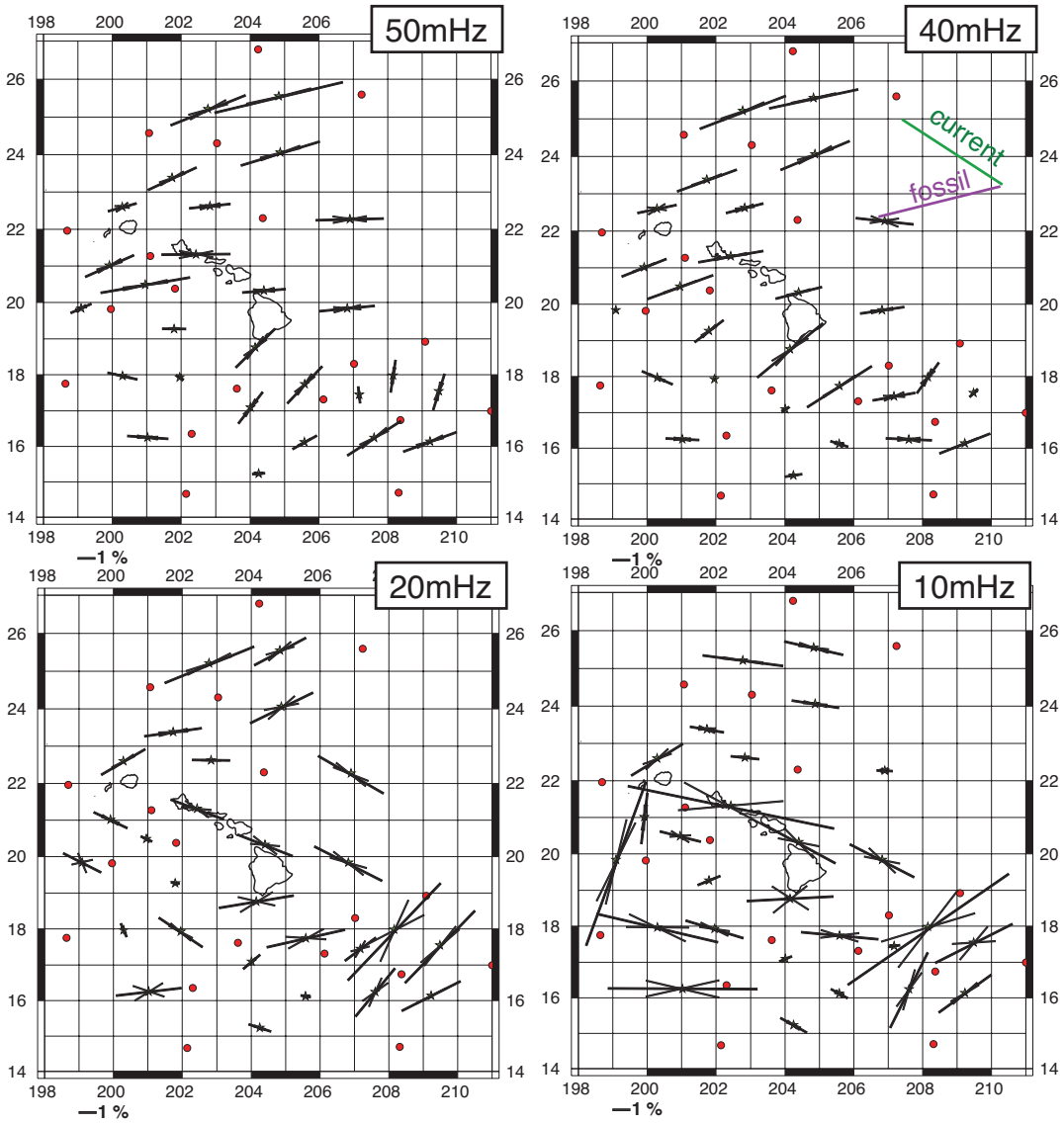

Figure 4.12: Results of the strength of anisotropy and the fast directions of all triangles with the frequencies of 10 mHz, 20 mHz, 40 mHz, 50 mHz. The current plate motion (123.4°) and the fossil plate motion (76°) are shown in the top right panel. The length of the black symbols shows the strength of anisotropy. The directions of this symbols show the fast directions. And the minor black lines on the symbols show the error of fast directions.

Chapter 5

Forward Modeling - 2-Layer Model

5.1 Test 1 - Vary the Boundaries

In chapter 5, we made the case for a six-layer model with two anisotropic layers that describes the seismological make up of the Pacific plate around Hawaii. Here, we take the anisotropic model to calculate the phase velocity as function of azimuth using a Fortran forward-modeling program. For each run, we call the Fortran program with one specific frequency to compute azimuthal anisotropy. The frequency varies from 10 mHz to 60 mHz with a step of 5 mHz. I wrote a c-shell script to streamline the computations. We will perform a number of tests to explore the impact of changing model parameters on the frequency-dependent azimuthal anisotropy of Rayleigh waves. In table 5.1, we list all the parameters in test 1a as well as the following tests. In the first test, we will explore how the frequency-dependent azimuthal anisotropy changes when we change the thickness of anisotropic layers. In the first run, test 1a, we change the bottom of the lower layer 1(present-day mantle flow). In test 1b, we change the top of layer 2(fossil spreading direction). Anisotropy at different frequencies are shown in different panels in figure 5.1 and figure 5.3.

In test 1a, the bottom of layer 1(the present-day's anisotropic layer) varies from 71 km to 251 km with a step of 30 km. At its greatest thickness, this layer includes the bottom of the lithosphere as well as part of the asthenosphere. The upper boundary of the fossil anisotropic layer(layer 2) is fixed at 21 km. The boundary between the two layers is fixed at 71 km. We keep ϕ fixed of 45° in both layers. In figure 5.1, the curves of different depths are shown with different colors. In the first panel(10 mHz), the curve of varying depths of the bottom of layer 1 has the most obvious differences. The curve with the deepest bottom of layer 1 appears to be the most anisotropic. The anisotropy gets weaker as the depth declines. Thus, Rayleigh waves of 10 mHz are very sensitive to deep structure. In contrast, for the frequency of 60 mHz in the last panel, the curves of varying depths of layer 1 are almost the same. Azimuthal anisotropy at 60 mHz is not affected by structures below a depth of 71 km. Figure 5.2 shows a plot of strength of anisotropy as a function of frequency. For each frequency, the strength of anisotropy increases as the bottom of layer 1 gets deeper. However, at frequencies 50 mHz and greater, the strength of anisotropy does not change when the bottom of layer 1 is of depths greater than 101 km. The strength of anisotropy changes more with frequency as the depth of the bottom of layer 1 is shallower. This is because the low-frequency waves depend on the integral of anisotropy anisotropic structure for a larger and deeper depth range in order to build up significant azimuthal anisotropy. When the bottom of layer 1 is 251 km and 221 km, the strength of anisotropy does not change significantly with frequency (varying from 6.8% to 8.2%). It shows that the strength of anisotropy of Rayleigh waves with high frequency is less sensitive to the depth of the bottom of the present-day's anisotropic layer. That indicates surface waves with higher frequencies are less likely be influenced by deeper media. Moreover, the curves of the bottom depth at 251 km, 221 km and 191 km even have a summit at 20 mHz.

Table 5.1: A list of all the parameters in each test

test	fixed parameters	variable parameters
test 1a	top of layer 2, boundary between layer 1 and 2, $\theta_1, \theta_2, \phi_1, \phi_2$	bottom of layer 1
test 1b	bottom of layer 1, boundary between layer 1 and 2, $\theta_1, \theta_2, \phi_1, \phi_2$	top of layer 2
test 2	top of layer 2, boundary between layer 1 and 2, bottom of layer 1, $\phi_1 = \phi_2$	θ_1, θ_2
test 3	top of layer 2, boundary between layer 1 and 2, bottom of layer 1, $\theta_1 = \theta_2, \phi_1$	ϕ_2
test 4	top of layer 2, boundary between layer 1 and 2, bottom of layer 1, $\theta_1 = \theta_2, \phi_2$	ϕ_1
test 5	top of layer 2, boundary between layer 1 and 2, bottom of layer 1, $\theta_1 = \theta_2, \phi_1$	ϕ_2
test 6	top of layer 2, boundary between layer 1 and 2, bottom of layer 1, θ_1, ϕ_1, ϕ_2	θ_2
test 7a	top of layer 2, bottom of layer 1, $\theta_1, \phi_1, \phi_2, \theta 2$	boundary between layer 1 and 2
test 7b	top of layer 2, bottom of layer 1, $\theta_1, \phi_1, \phi_2, \theta 2$	boundary between layer 1 and 2

As for test 1b, figure 5.3 also has eleven panels for different frequencies from 10 mHz to 60 mHz with a step of 5 mHz. The upper boundary of layer 2 varies from 21 km to 71 km with a increment of 10 km. The boundary between the two layers is always fixed at 71 km. The bottom of the lower layer(layer 1) is fixed at 251 km. In contrast to figure 5.1, in figure 5.3, the curves in the first panel shows the smallest differences among panels of all the frequencies. The curve for the top of layer 2 at 21 km has the strongest resulting azimuthal anisotropy and the curve for 71 km has the smallest. However, as the frequency increases, the difference between curves of different tops of layer 2 becomes greater. In the last panel at the frequency of 60 Hz, the curve of 21 km has the strongest anisotropy while the curve turns less anisotropic when the depth increases to 71 km. This is because 60 mHz waves are no longer sensitive to structure at that depth. Similarly strength of anisotropy as a function of frequency is plotted in figure 5.4. Here, the

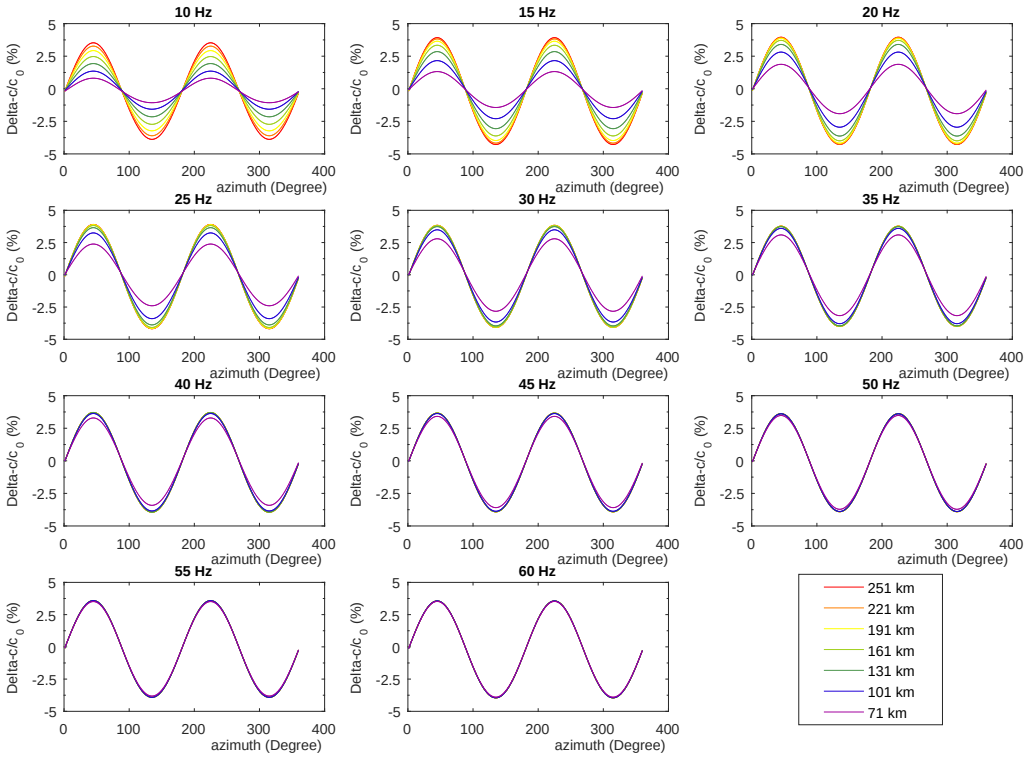

Figure 5.1: Test 1a, result of forward modeling. The lower boundary of the lower anisotropic layer (layer 1) varies from 71 km to 251 km, the upper boundary of layer 2 is set to 21 km. Colors mark resulting azimuthal anisotropy curves for varying the bottom of layer 1. The frequency varies from 10 mHz to 60 mHz.

anisotropy changes the most for the highest frequencies while that for low frequencies changes only moderately. Note that the anisotropy at 60 mHz does not change much once the upper bound of layer 2 is 51 km or deeper. This is because the sensitivity of high frequency waves to changes in structure concentrates to a depth range of shallower depths, up to about 50 km. When the depth of the upper boundary is 21 km, it has the highest strength of anisotropy. For all the other depths except 21 km, the strength of anisotropy have an over all trend that declines with increasing frequency. That means 21 km is a depth that all the frequencies from 10 mHz to 60 mHz can penetrate. Rayleigh waves with higher frequency are more likely to be influenced by the upper boundary of

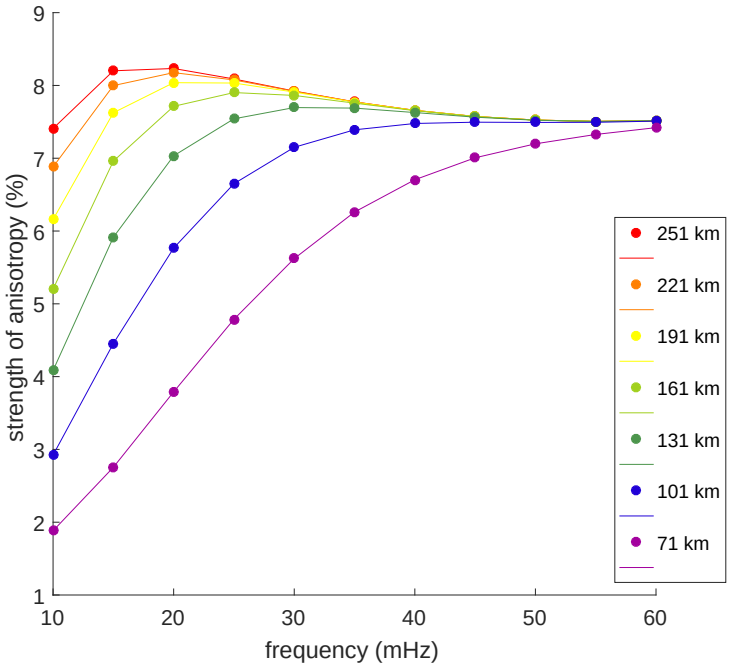

Figure 5.2: Test 1a, strength of anisotropy as a function of frequency: Layer 1 varies from 71 km to 251 km. Colors mark the strength of anisotropy for varying the bottom of layer 1.

the fossil anisotropic layer. That means surface waves with higher frequencies are more likely to be influenced by shallow media.

The result of forward modeling are generally consistent with our expectation in Chapter 2. The sensitivity kernels of Rayleigh waves in figure 8 and 9 of Chapter 2 show that Rayleigh waves with high frequencies are more sensitive to shallow media while Rayleigh waves with low frequencies are more sensitive to deep media.

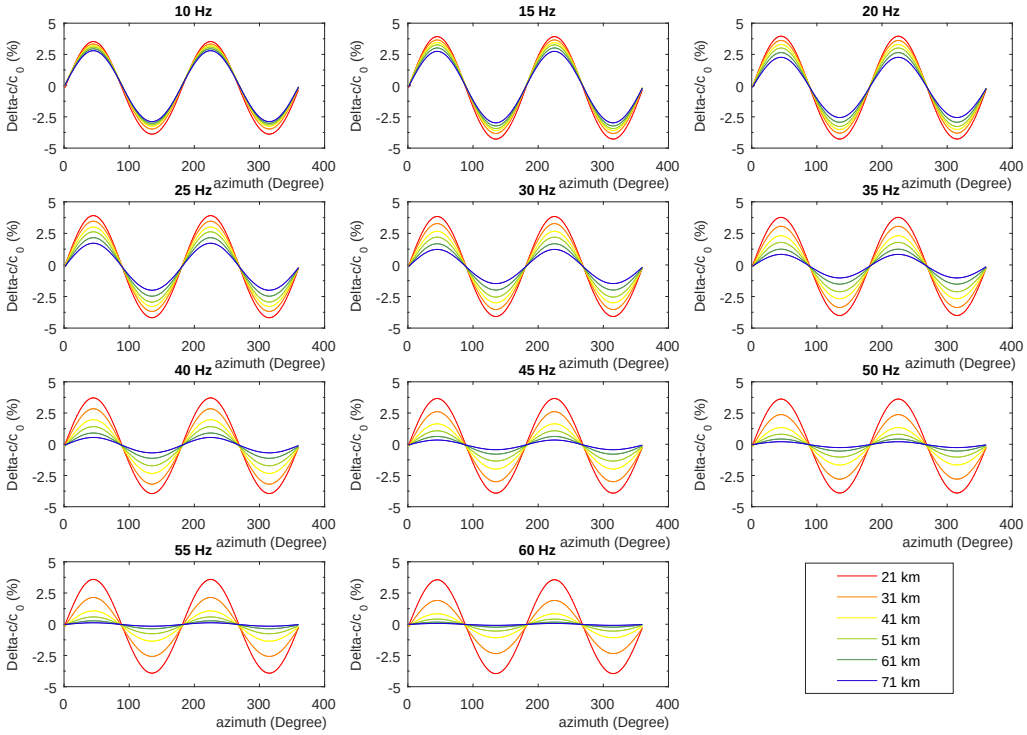

Figure 5.3: Test 1b, result of forward modeling: The upper boundary of layer 2 varies from 21 km to 71 km, the lower boundary of layer 1 is now set to 251 km. Colors mark resulting azimuthal anisotropy curves for varying the top of layer 2. The frequency varies from 10 mHz to 60 mHz.

5.2 Test 2 - Vary Inclination

In test 2, we will now change θ, the angles of the symmetry axis of the anisotropic medium with respect to the vertical direction. θ_1 and θ_2 are changed from 0° to 90° with a increment of 5°, where $\theta_1 = \theta_2$. The boundaries of the bottom layer(layer 1) and the top layer(layer 2) are all fixed. The bottom of layer 1 is 251 km. The boundary between layer 1 and layer 2 is 71 km. The top boundary of layer 2 is 21 km. $\phi_1 = \phi_2$ are fixed at 45°(see in chapter 1, figure 1.5). We still use the same Fortran program to calculate the azimuthal anisotropy as in test 1. But I wrote a new C-shell script. In figure 5.5, we plot the strength of anisotropy as function of frequency. Different colors show the strength of

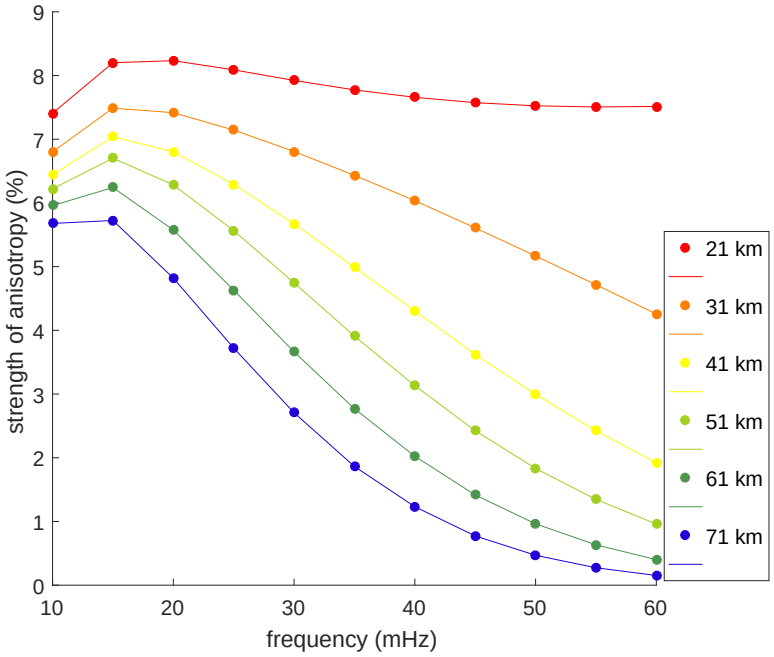

Figure 5.4: Test 1b, strength of anisotropy as a function of frequency: The upper boundary of layer 1 varies from 21 km to 71 km. Colors mark the strength of anisotropy for varying the upper boundary of layer 1. All other modeling parameters are the same as in test 1a.

anisotropy as a function of frequency with varying θ_1 and θ_2.

Figure 5.5 is a plot of the strength of anisotropy as a function of frequency. First of all, at each frequency, the strength of anisotropy increase with θ(when θ is small than 70°). Also, we can clearly see that the strength of anisotropy is 0% when θ is 0°. That is because the symmetric axis is vertical and the medium is transversely isotropic(TI) and so does not cause azimuthal anisotropy. Moreover, the strength of anisotropy is not obviously affected by frequency when θ is smaller than 25°. For θ smaller than 50°, it shows no frequency dependency in the strength of anisotropy. When frequency is larger than 20 mHz, the curves decline slightly as the frequency increases. When θ is larger than 70°, the curves of the strength of anisotropy have peaks at the frequency of 15 mHz.

As θ gets larger, the strength of anisotropy declines more significantly with increasing frequency.

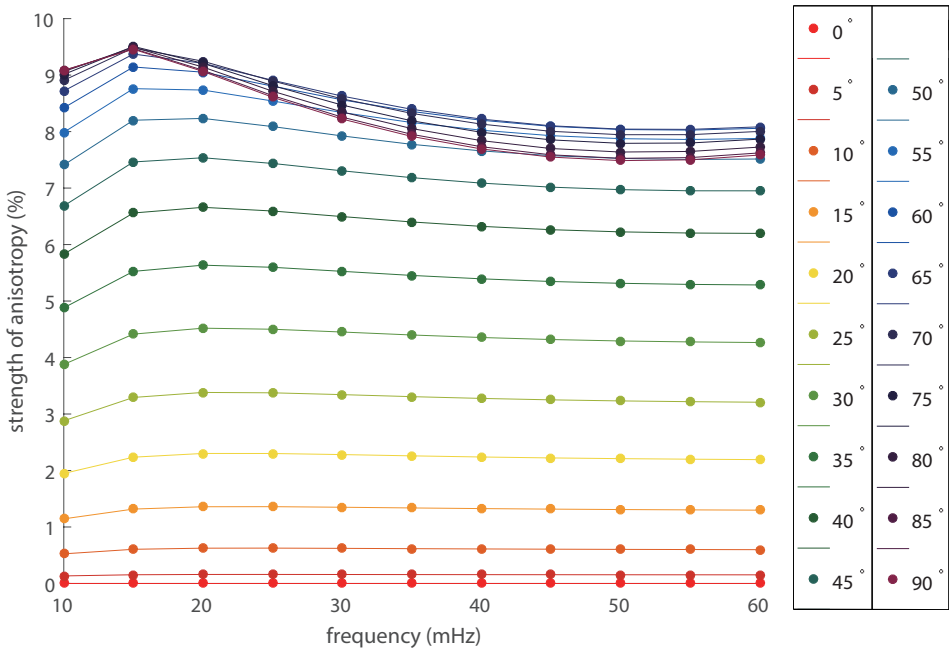

Figure 5.5: Test 2, Strength of anisotropy: Colors mark strength of anisotropy for varying input of θ's from 0° to 90° with a step of 5°. Frequency varies from 10 mHz to 60 mHz.

5.3 Test 3 - Vary Upper Azimuth ϕ_2

In test 3, we examine how the azimuthal anisotropy changes when we change ϕ_2, the azimuth in the shallower layer 2. We set the upper boundary of layer 2 at 21 km, the boundary between layer 1 and layer 2 at 71 km, the lower boundary of layer 2 at 251 km. All of the θ_1 and θ_2 are fixed at 50°. ϕ_1 of layer 1 is fixed at 15° while ϕ_2 of layer 2 varies from 0° to 170° with a increment of 10°. The same Fortran program is used to produce one curve of azimuthal anisotropy with every input. But I wrote a new C-shell

script that varies ϕ_2 on input.

We expect that the fast directions for low frequencies will be determined mainly by ϕ_1 while the fast direction for high frequencies will depend more on ϕ_2.

The left panel of figure 5.6 is a plot of fast direction as a function of frequency and the right panel is the strength of anisotropy as a function of frequency. In the left panel, the fast directions varies from 5° to 25° at the frequency of 10 mHz. But actually ϕ_1 is 15°. Thus, the fast direction at the frequency of 10 mHz is determined by both ϕ_1 and ϕ_2. When the frequency is larger than 30 mHz, the fast direction tends to stay in consistency with ϕ_2, which indicates that Rayleigh waves with a frequency higher than 30 mHz can not penetrate the lower anisotropic layer(layer 1). When the frequency is from 20 mHz to 25 mHz, the fast direction shifts significantly. We expect this range of frequency would be related to the depth of the boundary between layer 1 and layer 2. This will be explored in test 5.

In the right panel of strength of anisotropy, when ϕ_1 and ϕ_2 have the smallest difference (where $\phi_2 = 10°$ or 20° and the curve is red), the strength of anisotropy is the strongest(8.2%). As the angle between ϕ_1 and ϕ_2 gets larger, the strength of anisotropy gets smaller. But this is relevant only at low frequencies that have sensitivity to structure at depths greater than 50 km. When the angle between ϕ_1 and ϕ_2 exceeds 55°(on the legend, the curve for 70° or 140° and below), there is a minimum at the frequency of 20 mHz. When the angle between ϕ_1 and ϕ_2 continues to get larger, the curve of strength of anisotropy declines at any frequency. Such effects are strongest for frequencies at 20 mHz. When the angle between ϕ_1 and ϕ_2 gets to its maximum(on the legend, the curve for 100° or 110°), the curve's minimum is 1% at the frequency of 20 mHz. It is inferred

that if ϕ_1 and ϕ_2 of both layers are 15°, the anisotropy of the lithosphere as a whole can be maximized. When the angle between ϕ_1 and ϕ_2 is close to 90°, the strength of anisotropy declines to nearly 0%(at 20 mHz). The strength of anisotropy at a frequency as high as 60 mHz is equal to 7.5% and simply affected by ϕ_2 of the shallower layer. But at a frequency of 10 mHz, the azimuthal anisotropy are controlled by both ϕ_1 and ϕ_2, which ranges from 3.6% to 7.4%. That confirms what we have found in the plot of the fast direction. At last, we find the greatest varying in the strength of anisotropy between 1% and 8% at the frequency of 20 mHz. One possible reason is that the azimuthal anisotropy partially caused by layer 1 cancels out that caused by layer 2. Even though both layers have the same θ, i.e., the media have the same anisotropic strength. So 20 mHz is very close to a frequency at which both layers have equivalent contributions to azimuthal anisotropy. According to the sensitivity kernel in figure 1.5 of chapter 1, Rayleigh waves with the frequency of 20 mHz shows the greatest sensitivity to the media at the depths between 60 and 80 km, which is near our boundary at 71 km. If the boundary between the two layers are at a different depth, then the minimum of the curves should be at a different frequency.

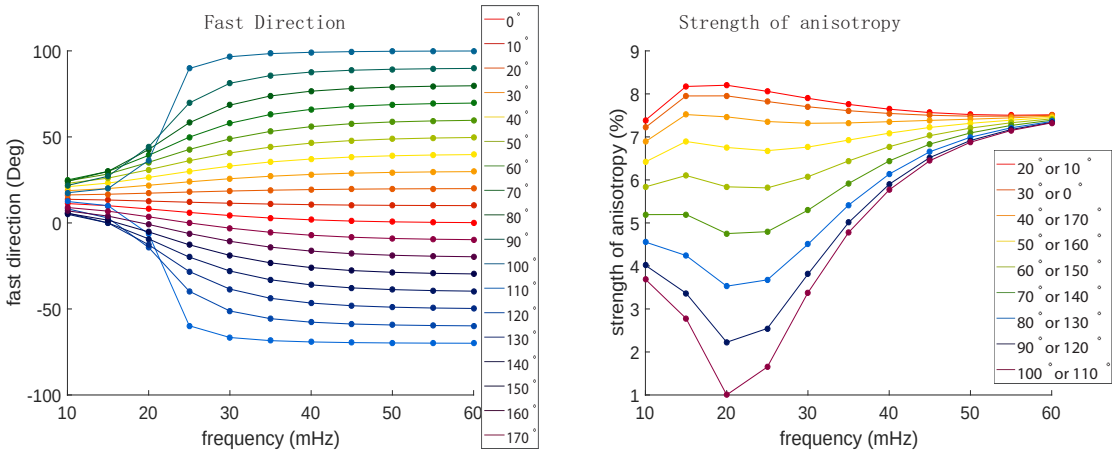

Figure 5.6: Test 3: The left panel is the fast direction as a function of frequency. The right panel is the Strength of anisotropy as a function of frequency. Colors mark varying input of ϕ_2. Since the strength of anisotropy is symmetric about 15°, each curve stands for two values of ϕ_2.

5.4 Test 4 - Vary Lower Azimuth ϕ_1

In test 4, ϕ_1 varies instead of ϕ_2. We would expect that the biggest effects are that the fast direction and the strength of anisotropy at high frequencies are mainly controlled by ϕ_2 and they change less as the frequency gets higher. ϕ_1 varies from 0° to 170° with a increment of 10° while ϕ_2 is fixed at 15°. We also set the upper boundary of layer 2 at 21 km, the boundary between layer 1 and layer 2 at 71 km, the lower boundary of layer 2 at 251 km. All of the θ_1 and θ_2 are fixed at 50°.

The left panel of figure 5.7 shows the fast direction as a function of frequency. At the highest frequency of 60 mHz, the fast direction is totally determined by ϕ_2 while it is mostly affected by ϕ_1 at 10 mHz though at a frequency of 10 mHz, Rayleigh waves still have a little sensitivity to the top layer(layer 2). 20 mHz to 25 mHz is a range of frequency where all curves of the fast direction shift from a value near ϕ_1 to ϕ_2. It is the same range with that of test 3. Note that the frequency of this transition depends on where we position the boundary between layer 1 and layer 2.

The right panel of figure 5.7 is a plot of strength of anisotropy as a function of frequency. The plot is totally identical with test 3 because it is the angle between ϕ_1 and ϕ_2 that really affects the strength of anisotropy. It does not matter if we fixed ϕ_2 instead of ϕ_1. We keep θ_1 and θ_2 the same and also the depths of all boundaries but only change ϕ_1 or ϕ_2.

5.5 Test 5 - Vary Upper ϕ_2 With Different Boundary d_{12}

In test 5, we repeat test 3 but now change the position of the boundary between the two layers. This should have an impact on the frequency range at which the transition

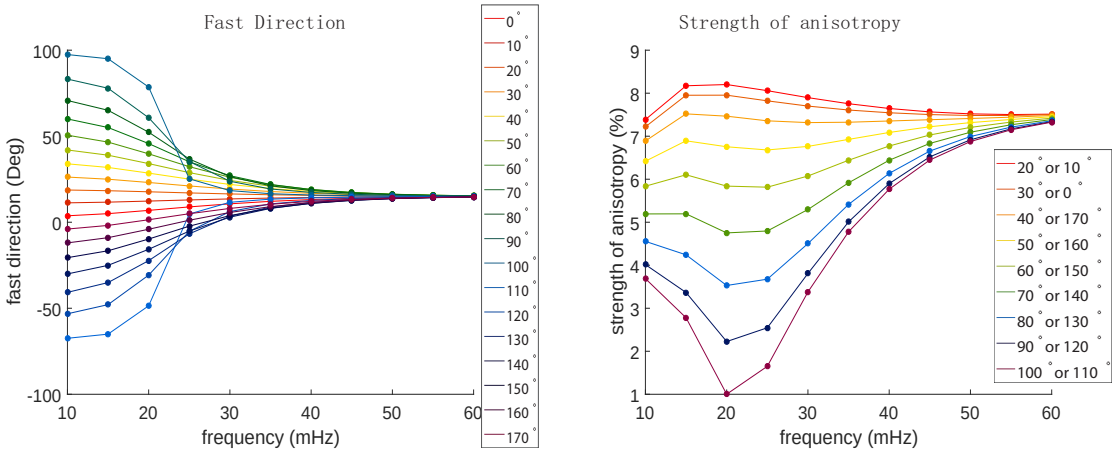

Figure 5.7: Test 4: The left panel is the fast direction as a function of frequency. The right panel is the Strength of anisotropy as a function of frequency. Colors mark varying input of ϕ_1. Since the strength of anisotropy is symmetric about 15°, each curve stands for two values of ϕ_1.

occurs in the fast direction and the frequency at which the strength of anisotropy gets to the minimum. We set the upper boundary of layer 2 at 21 km, the boundary between layer 1 and layer 2 at 41 km, the lower boundary of layer 2 at 251 km. All of the θ_1 and θ_2 are fixed at 50°. ϕ_1 of layer 1 is fixed at 15° while ϕ_2 of layer 2 varies from 0° to 170° with a increment of 10°. The only difference from test 3 is that the boundary between layer 1 and layer 2 is fixed to 41 km instead of 71 km. We will compare the result of test 3 and test 5. It is expected that the "shifting range" of the fast direction can move to a higher frequency.

The left panel of figure 5.8 shows the fast direction as a function of frequency. At the frequency of 10 mHz, the fast direction is around 10° to 20°. And when the frequency is larger than 45 mHz, the fast direction is close to ϕ_2. When the frequency is in the range from 35 mHz to 45 mHz, the curves of fast direction shift from a value near ϕ_1 to a value near ϕ_2. Note that for test 3, this transition occurs at lower frequencies. However, compared with test 3, the fast direction at the frequency of 60 Hz can still be affected by ϕ_1. Because the boundary between layer 1 and layer 2 is much shallower than that in test 3, Rayleigh waves of 60 mHz still have a little sensitivity to the bottom layer 1.

In the right panel of figure 5.8, the strength of anisotropy varies from 0.6% to 8.1%. The curves of strength of anisotropy still decrease with increasing angle between ϕ_1 and ϕ_2. The minimums of the curves with ϕ_2 at 100°, 110°, 90°, 120°, 80°, 130°, 70°, 140°, 60°, 150° appear to be moved to 40 mHz while it is 20 mHz in test 3. Because the boundary between layer 1 and layer 2 is changed from 71 km to 41 km. The frequency at which the effects from both layers cancel each other out also increases accordingly.

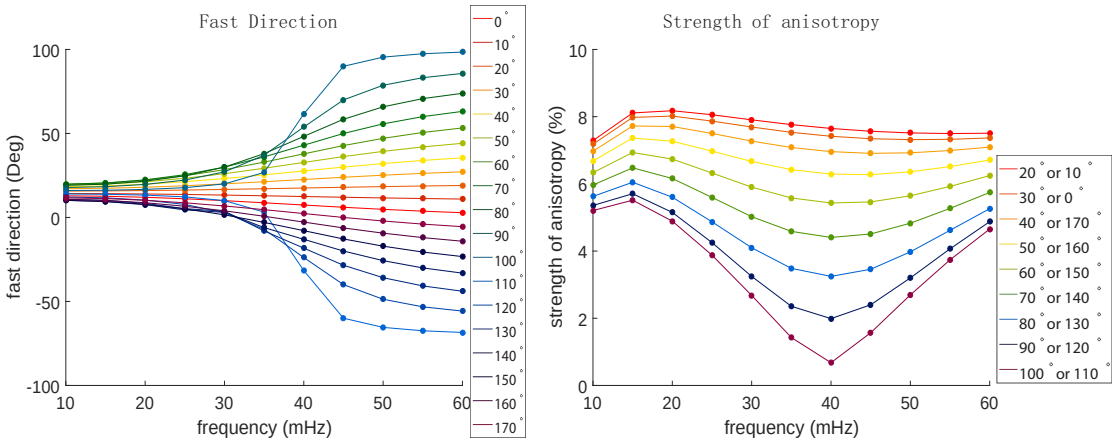

Figure 5.8: Test 5, a repeat of test 3, but new $d_{12} = 41$ km instead of 71 km: Colors mark varying input of ϕ_2. The left panel is the fast direction as a function of frequency. The right panel is the strength of anisotropy as a function of frequency. Since the strength of anisotropy is symmetric about 15°, each curve stands for two values of ϕ_2.

5.6 Test 6 - Vary the Inclination θ_2

In test 6, we examine in more detail how a changing θ_2 of layer 2 can influence both the fast direction and the strength of anisotropy when $\phi_1 \neq \phi_2$. We set the upper boundary of layer 2 at 21 km, the boundary between layer 1 and layer 2 at 71 km, the lower boundary of layer 2 at 251 km. ϕ_1 is fixed at 15° and ϕ_2 is fixed at 60°. θ_1 is fixed at 50°. θ_2 varies from 0° to 90° with an increment of 5°. The fast direction and

the strength of anisotropy are expected to be changed as θ_2 increases from 0° to 90°. Also, they should have a frequency dependency because the two layers have different θ's and Rayleigh waves with different frequencies are sensitive to media at different depth. Because we change θ of layer 2, we expect the most dramatic changes at high frequencies.

The left panel of figure 5.9 shows the fast direction as a function of frequency. When θ_2 is 0°, layer 2 does not contribute to azimuthal anisotropy. The fast direction is therefore ϕ_1 for all frequencies. We also see in the panel on the right that the strength of anisotropy declines with increasing frequency to nearly zero at 60 mHz. For each frequency, as θ_2 increases, the fast direction also increases towards ϕ_2 though ϕ_2 is reached only at high frequencies. For all θ_2 larger than 10°, the fast direction at 60 mHz are all very close to ϕ_2. This means that θ_2 does not have to be far from the vertical to contribute significant anisotropy.

In the right panel of figure 5.9, the strength of anisotropy varies from 5.5% to 6.2% at the frequency of 10 mHz. Such amount of anisotropy is mainly caused by layer 1. Once θ_2 reaches 35° degrees, only small changes occur for both the fast direction and the strength of anisotropy, even at low frequencies.

5.7 Test 7 - Vary Boundary d_{12}

In test 7a and test 7b, we explore how azimuthal anisotropy changes with varying the depth of the boundary between layer 1 and layer 2 (denoted as d_{12}). In test 7a, d_{12} varies from 31 km to 171 km with a step of 10 km. The bottom of layer 1 is fixed at 251 km and the top of layer 2 is fixed at 21 km. θ_1 and θ_2 are both fixed at 80°, as a realistic

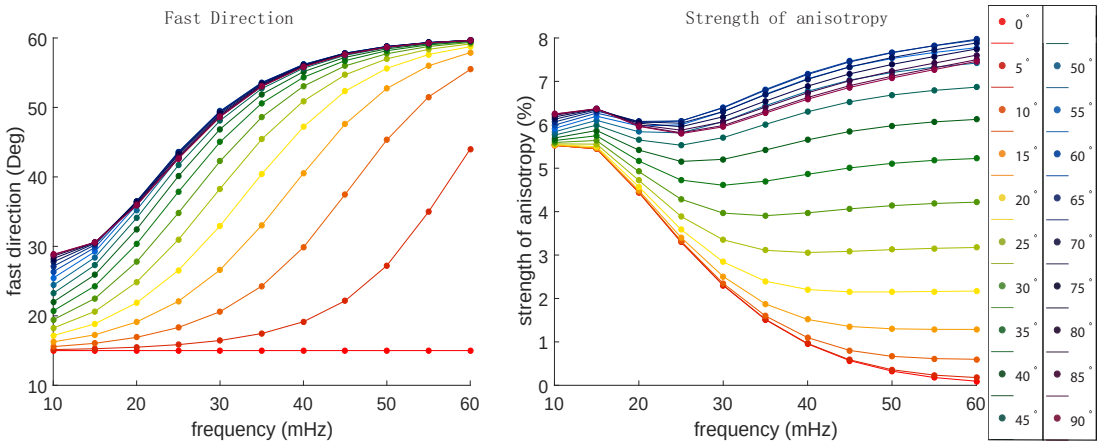

Figure 5.9: Test 6: The left panel is the fast direction as a function of frequency. The right panel is the Strength of anisotropy as a function of frequency. Colors mark varying input of θ_2

value. ϕ_1 is 123°(the present day plate motion). ϕ_2 is 76°(the fossil plate motion). We expect to see that at high frequencies, the fast direction changes greatly with d_{12} when d_{12} is relatively shallow. Otherwise, when d_{12} is deeper, the fast direction is mainly determined by the fossil direction of motion in layer 2. So the fast direction no longer changes at high frequencies. At low frequencies, the azimuthal anisotropy has a larger sensitivity to deeper media so we expect changes to greater depths of d_{12}.

The left panel in figure 5.10 shows the fast direction resulting from the forward modeling. At a frequency of 10 Hz, the fast direction decreases steadily from 117° to 86° as d_{12} increases. When d_{12} is as shallow as 31 km to 61 km, the result shows that Rayleigh wave with 10 mHz is less impacted by layer 2 because it is thinner. At frequencies near 35 mHz, the fast direction remains near the fossil spreading direction as long as d_{12} is about 91 km or deeper. This indicates that Rayleigh waves with 35 mHz are sensitive to structure up to this depth but not much beyond that(see sensitivity kernels in Figure 1.5 in Chapter 1). At the frequency of 60 mHz, when d_{12} is deeper than 51 km, the fast directions are all very close to 76°, the direction of fossil plate motion. However,

when d_{12} is 31 km or 41 km, the fast direction will tend towards the present-day direction but will not reach it. The reason for this is because 60 mHz Rayleigh waves are sensitive primarily to shallow structure.

The right panel of figure 5.10 shows the strength of anisotropy as a function of frequency. First, we can compare the curve of $d_{12} = 71$ km with another curve in test 4(when $\phi_2 = 60^\circ$). The angle between ϕ_1 and ϕ_2 are similar. So the overall shape of the two curves are identical. While in test 4, θ_1 and θ_2 are fixed at 50°, which is smaller than a real case. The curve of strength of anisotropy in test 4 is obviously smaller than that in this test. Secondly, take the curve of $d_{12} = 41$ km for example. The curve has a minimum at the frequency of 45 mHz. That is the depth of d_{12} at which the contribution from both layers partially cancel out with each other. As d_{12} gets larger, the frequencies of the minimums get smaller. When d_{12} is deeper than 101 km, its minimum even gets smaller than 10 mHz and can not be seen in the plot. Moreover, at the frequency of 60 mHz, the strength of anisotropy for d_{12} varying from 71 km to 171 km have little differences from each other for this particular frequency. That means Rayleigh waves with a frequency of 60 mHz are not sensitive to media deeper than 61 km. At lower frequencies, more symbols with higher and higher depths are not distributed in a close range. Thus the depth of sensitivity gets larger.

In test 7b, d_{12} varies from 41 km to 151 km with a step of 10 km. The bottom of layer 1 is fixed at 201 km and the top of layer 2 is fixed at 31 km. So essentially, both anisotropic layers are thinner. θ_1 and θ_2 are all fixed at 80°. ϕ_1 is 123°(the present day plate motion). ϕ_2 is 76°(the fossil plate motion). Because the anisotropic layers are now thinner, we expect that the strength of anisotropy is diminished for all frequencies.

The left panel of figure 5.11 shows the fast direction as a function of frequency.

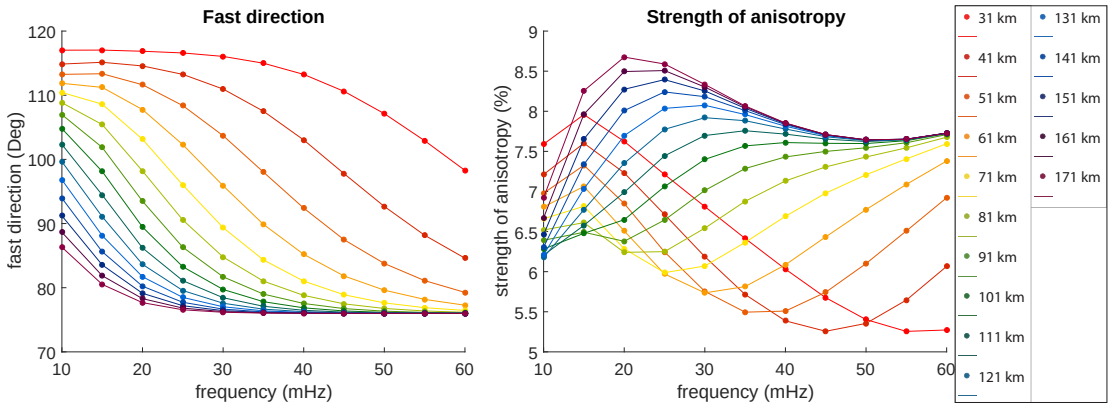

Figure 5.10: Test7a: The left panel is the fast direction as a function of frequency. The right panel is the Strength of anisotropy as a function of frequency. Colors mark varying depths of the boundary between layer 1 and layer 2 (d_{12})

Generally the figure looks similar to that of test 7a. Unlike the plot of fast direction in test 7a, only when $d_{12} = 41$ km, the fast direction at the frequency of 60 mHz appears to be far from 76°(the fossil plate motion). Because the top of layer 2 is deeper and the thickness of layer 2 is thinner than that in test 7a, layer 1 now has more contributions to the fast direction. When d_{12} is ranging from 81 km to 151 km and the frequency is larger than 35 mHz, layer 2 has much stronger impact on the fast direction than that of layer 1. At small frequencies, the fast direction varies greatly because the both layers have considerable contributions to it.

The right panel shows the strength of anisotropy as a function of frequency. The most important difference from test 7a is that the strength of anisotropy at every conditions is generally smaller than that of test 7a because both layer 1 and layer 2 gets thinner. At high frequencies, now the symbols are distributed closer to each other comparing to that of test 7a.

A summary of all the tests is shown in table **??**.

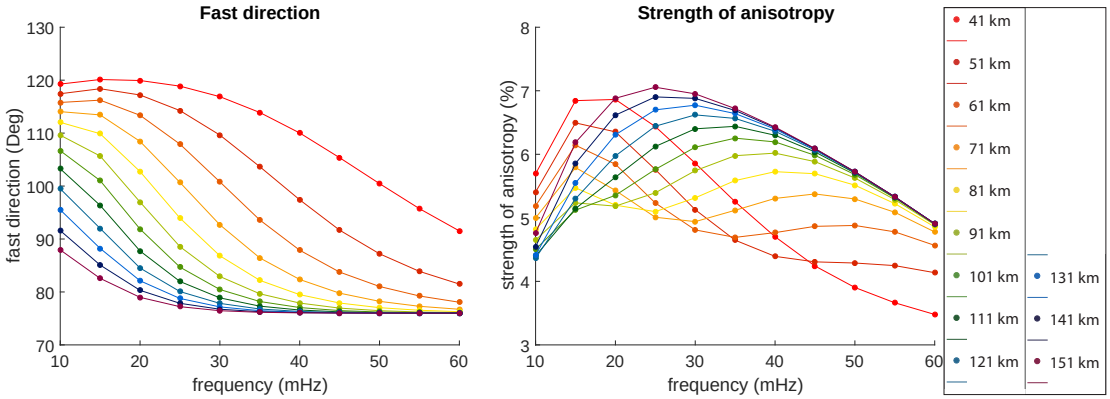

Figure 5.11: Test7b: The left panel is the fast direction as a function of frequency. The right panel is the Strength of anisotropy as a function of frequency. Colors mark varying input of the boundary between layer 1 and layer 2

Table 5.2: A summary of all the tests

test number	variable parameter	figure number	most important result
test 1a	bottom of layer 1	5.2	The bottom of layer 1 has larger influence on azimuthal anisotropy as the frequency gets lower. SA is dramatically reduced if the bottom of layer 1 is at 101 km.
test 1b	top of layer 2	5.4	The top of layer 2 has larger influence on azimuthal anisotropy as the frequency gets higher. SA is dramatically reduced for 60 mHz if the top of layer 2 is at 61 km.
test 2	$\theta_1 = \theta_2$	5.5	θ controls the strength of anisotropy of a medium. The larger θ is, the stronger anisotropy occurs. SA is dramatically reduced if θ is less than 40°.
test 3	ϕ_2	5.6	For $\Delta\phi$ ($\phi_1 - \phi_2$) ranging from 65° to 95°, SA is dramatically reduced at a certain frequency.
test 4	ϕ_1	5.7	SA is the same with that in test 3 but the fast direction is different.
test 5	like test 3 but $d_{12} =$ 41 km instead of 71 km	5.8	Comparing to test 3, a shallower d_{12} shifts the minimum in SA to a higher frequency.
test 6	θ_2	5.9	θ_2 We compare this test to test 2 but now $\phi_1 \neq \phi_2$ and $\theta_1 \neq \theta_2$. SA drops dramatically at high frequencies when θ_2 is smaller than 35°.
test 7a	d_{12}	5.10	Now we are using realistic ϕ_1 and ϕ_2. A d_{12} shallower than 81 km dramatically impact the fast direction and SA, particularly at high frequencies.
test 7b	d_{12} but the top of layer 2 is deeper and the bottom of layer 1 is shallower. The anisotropic layers get thinner.	5.11	SA is dramatically reduced at all frequencies but particularly at high frequencies.

Chapter 6

Grid Search Modeling of Real Data

6.1 Grid Search For Bottom of Layer 1 And Top of Layer 2 by Strength of Anisotropy

Triangle 4 consists of 3 stations including PL48(22.2986° N 155.6336° W), PL44(25.5928° N 152.7643° W), PL46(24.3082° N 156.9659° W). We get the centroid of triangle 4 by taking the average of the coordinates of these three stations. The coordinate of the centroid is (24.0665° N 155.1213° W). Figure 6.1 is a map of triangle 4.

Figure 6.2 shows the observed results of triangle 4. A plot of the fast direction is shown in the left panel and the plot of the strength of anisotropy is shown in the right panel.

In the first step of inversion, we use a grid search to find out which 2-layer anisotropic model fits the observed strength of anisotropy best. The bottom of layer 1 is varied from 71 km to 251 km with a step of 10 km and the top of layer 2 is varied from 21 km to 71 km with a step of 10 km. The boundary between layer 1 and layer 2 is fixed at

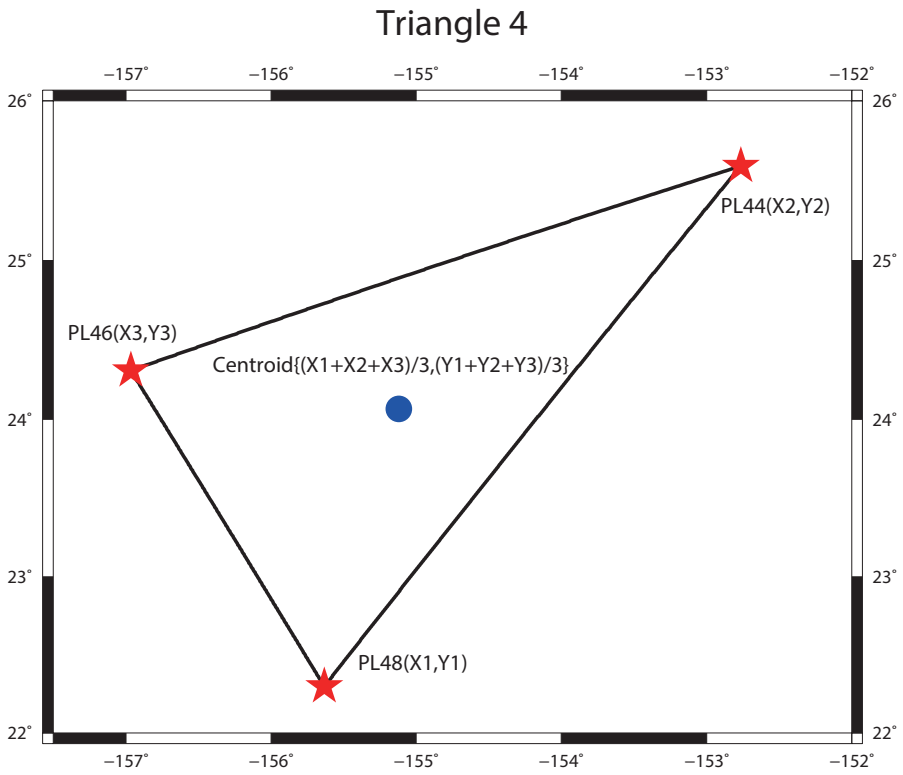

Figure 6.1: A map of triangle 4 and its centroid: the coordinate of the centroid is determined as the average of the coordinates of stations PL48, PL44 and PL46.

71 km. $\theta_1 = \theta_2 = 80°$, $\phi_1 = 123°$ and $\phi_2 = 76°$. The strength of anisotropy with respect to frequency is calculated at each grid point using a forward modeling program pyro2 provided by Gabi. I wrote a Fortran program to calculate the misfit between the observed data and the forward modeling data. In the following parts, we will discuss the way the frequency-dependent data points are weighted and how we get the best fitting model.

Case 1: all the data points are equally weighted.

The misfit(MF) and the variance(VR) are calculated by:

$$MF = \frac{1}{N}\sum_{N}(d_{oi} - d_{pi})^2 \tag{6.1}$$

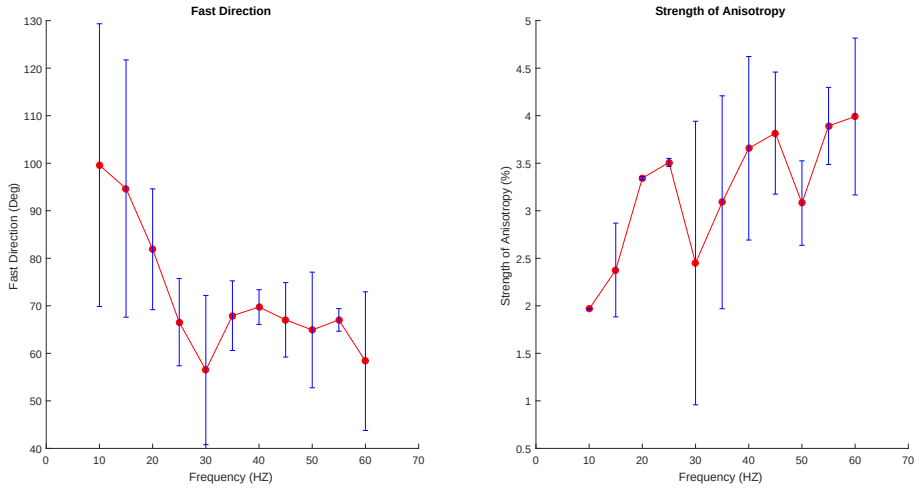

Figure 6.2: Result of triangle 4: the left panel shows the fast direction as a function of frequency and the right panel shows the strength of anisotropy as a function of frequency.

$$
\begin{aligned}
VR &= (1 - \frac{Var_2}{Var_1}) \times 100\% \\
Var_2 &= \frac{1}{N-1} \sum_i (d_{oi} - d_{pi})^2 \\
Var_1 &= \frac{1}{N-1} \sum_i (d_{oi} - \bar{d})^2
\end{aligned} \tag{6.2}
$$

d_{oi} is the observed datum, d_{pi} is the predicted datum, σ_i is the error, N is number of data, Var_1 is initial variance, Var_2 is modeled variance, $\bar{d}$ is the mean value of the observed datum.

During a grid search, we calculate the misfit at every value of top of layer 1 and every value of bottom of layer 2. Then we get a matrix of misfit. Figure 6.4 shows a matrix of misfit. We find the best fitting model when the bottom of layer 1 is at 111 km and the top of layer 2 is at 41 km. Misfit in the matrix varies from nearly 1 to 12. The smallest misfit doesn't show up at the edge of the matrix, so the best fitting model is obtained. Figure 6.3 shows a data fit plot. The green curve represents the predicted

data by forward modeling. The red curve shows the observed data. At frequencies from 10 mHz to 50 mHz, the difference between the predicted data and the observed data are acceptable. At 30 mHz and 35 mHz, the predicted data are much bigger than the observed data, but they are still in the range of error bar. The observed data at 55 mHz and 60 mHz can't be fitted with our predictions. The variance reduction(VR) for this case is -64.83%. The last two data points contribute to most of the negative variance reduction. In this case, all the data are equally weighted and we haven't pay attention to errors at different data points. It is possible that some data with large error may add too much uncertainty to the inversion.

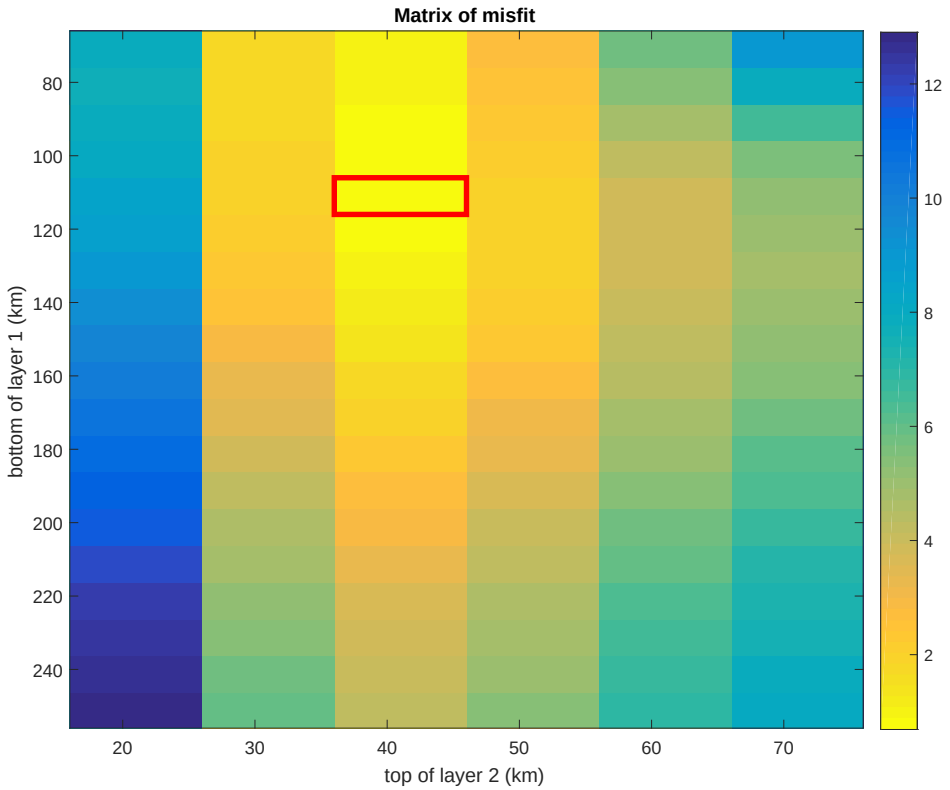

Figure 6.3: A matrix of misfit in case 1: All data are equally weighted. The red box shows the best fitting model.

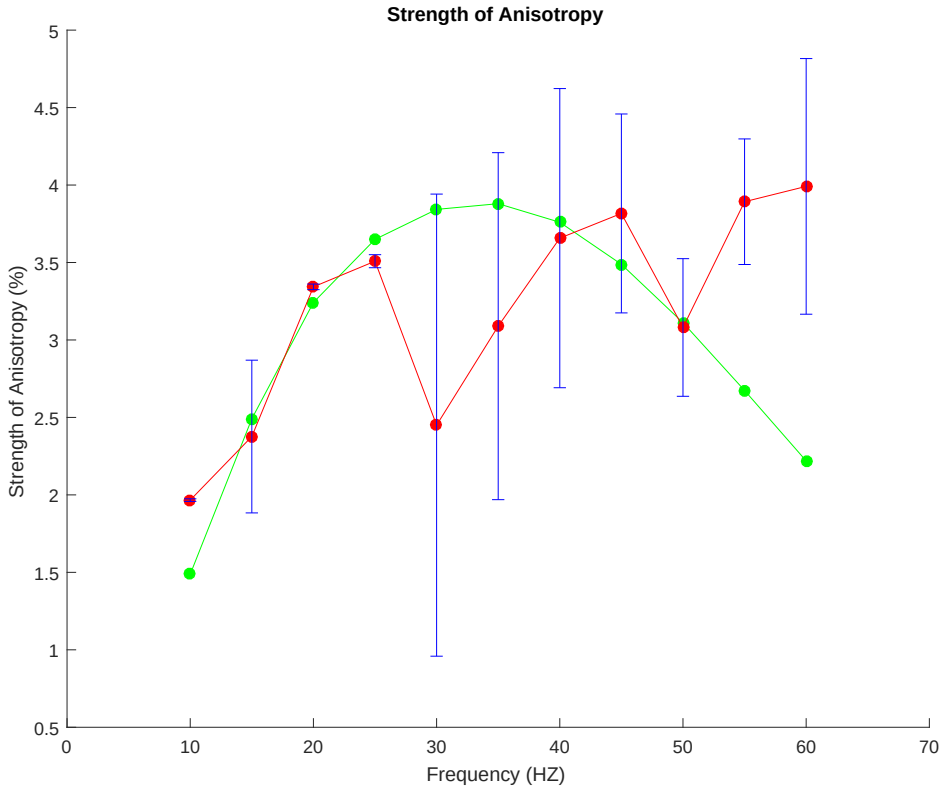

Figure 6.4: A fit plot of triangle 4: All data are equally weighted. The strength of anisotropy predicted by the best fitting model is showed by the green curve. The observed strength of anisotropy of triangle 4 is showed by the red curve with error bars.

Case 2: the data points are weighted by their error bars.

The misfit(MF) and the variance(VR) are calculated by:

$$MF = \frac{1}{N}\sum_{N}\left(\frac{d_{oi} - d_{pi}}{\sigma_i}\right)^2 \tag{6.3}$$

$$VR = (1 - \frac{Var_2}{Var_1}) \times 100\%$$
$$Var_2 = \sum_N (\frac{d_{oi} - d_{pi}}{\sigma_i})^2 / (\sum_N \frac{1}{\sigma_i^2})$$
$$Var_1 = \sum_N (\frac{d_{oi} - \bar{d}}{\sigma_i})^2 / (\sum_N \frac{1}{\sigma_i^2}) \quad (6.4)$$

d_{oi} is the observed datum, d_{pi} is the predicted datum, σ_i is the error, N is number of data, Var_1 is initial variance, Var_2 is modeled variance, $\bar{d}$ is the mean value of the observed datum.

Figure 6.5 shows a matrix of misfit for which all the data are weighted by errors. Since the best fitting model is lying on the edge of the matrix, this result may not be the correct answer we are looking for. Figure 6.6 shows the fit to the data. It is obvious that the observed data can not be fitted by the predicted curve when the frequency is larger than 30 mHz. Since we have 3 errors (out of 11) that are extremely small, these 3 data points dominate the inversion. Some extremely small errors are regarded as mistakes in the observation. The consequence of this is that the top of layer 2 is pushed from 41 km to 71 km, effectively eliminating the layer. In figure 6.6, we can see the strength of anisotropy nearly vanishes at high frequencies. Thus, we should apply a minimum error threshold to down weight data with extremely small error bars.

Case 3: Set a threshold for error.

Since small values of error can dominate the inversion. It is practical to set a specific threshold for error. In this case, we will find out the best threshold from 0.1, 0.15, 0.25, 0.4 and 0.8. Figure 6.7 shows the matrix of misfit for all the thresholds. When the threshold is 0.1, the misfits at most matrix components are relative large. The figure of

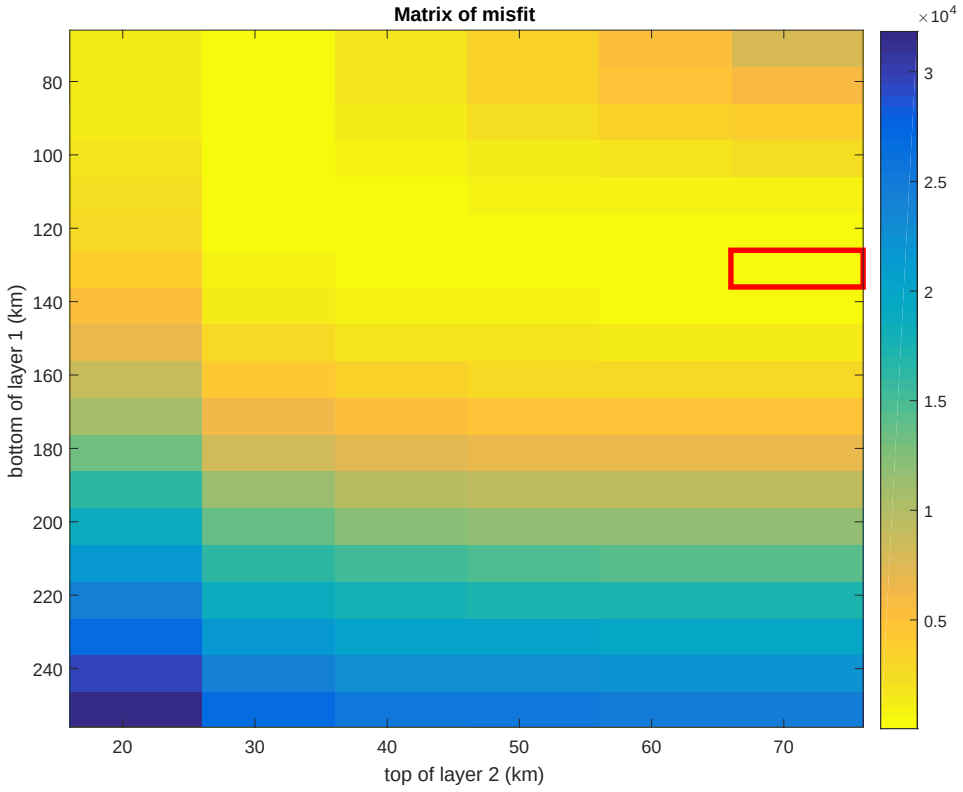

Figure 6.5: A matrix of misfit when data are weighted by their errors, case 2: The red box shows the best fitting model.

matrix looks similar with Case 2 but the best fitting model is different. As the threshold increases, the matrix changes to a pattern like case 1 and the misfit also decreases.

For all of the different thresholds, the best fitting model is always 111 km (bottom of layer 1) and 41 km (top of layer 2). So the fit plot should be the same with case 1 (shown in figure 6.8). We choose 0.4 as a preferred value because a regular data of error is usually larger than 0.4 if we don't take the 3 small error into consideration.

Table 6.1 shows all the results of case 1, case 2, case 3. When the error threshold gets larger, the misfit(MF) gets smaller while the variance reduction(VR) is reduced

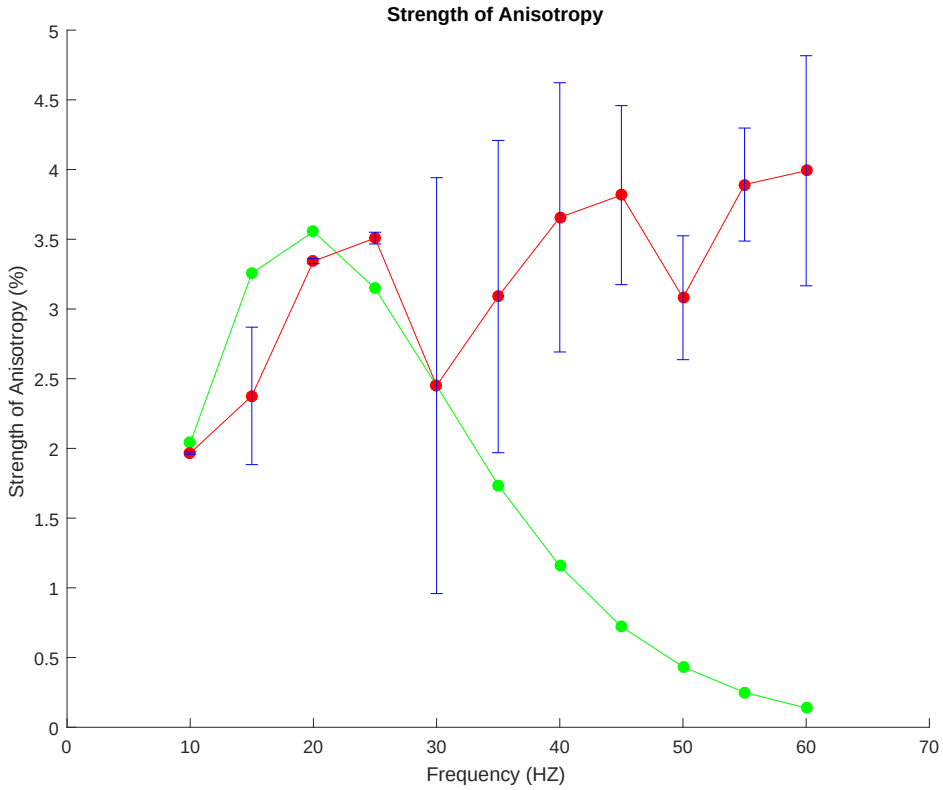

Figure 6.6: A fit plot of triangle 4 when data are weighted with their errors. The strength of anisotropy predicted by the best fitting model is showed by the green curve. The observed strength of anisotropy of triangle 4 is showed by the red curve with error bars.

significantly. When the error threshold is 0.8 or equally weighted, the variance reduction become a negative number. However, the best fitting model does not change with various threshold, so we can not judge which fit is the best only by comparing MF and VR.

6.2 Grid Search for ϕ_1 and ϕ_2 by Fast Direction

In this part, We use a grid search to find out the best ϕ_1 and ϕ_2 to fit the observed fast direction. The present day plate motion direction is 123°, we set a range of ϕ_1 which

Table 6.1: Result of various fit for the strength of anisotropy

Test number	error threshold	MF	VR	best fit(top of layer 2, bottom of layer 1)
Test 1, case 3	0.1	3.75	73.23%	41 (km), 111 (km)
Test 2, case 3	0.15	2.44	63.85%	41 (km), 111 (km)
Test 3, case 3	0.2	1.77	52.73%	41 (km), 111 (km)
Test 4, case 3	0.4	1.54	7.00%	41 (km), 111 (km)
Test 5, case 3	0.8	0.81	-39.91%	41 (km), 111 (km)
case 2	weighted with errors(no threshold)	42.15	91.98%	71 (km), 131 (km)
case 1	equally weighted	0.69	-64.83%	41 (km), 111 (km)

contains 123°. We assume that ϕ_1 is varied from 70° to 150° with the step of 10°. The fossil plate motion direction is 76°. ϕ_2 is assumed to be varied from 40° to 100° with the step of 5°. Then we use two parameters of best fitting model found in section 7.2. The top of layer 2 is fixed at 41 km and the bottom of layer 1 is fixed at 111 km. The boundary between layer 1 and layer 2 is fixed at 71 km. $\theta_1 = \theta_2 = 80°$. As with fitting the SA. We apply our search search to 3 cases: equal weight, raw error weight, error weight with minimum threshold.

Case 1: all the data points are equally weighted.

We find the best fitting model when $\phi_1 = 110°$ and $\phi_2 = 55°$. Figure 6.10 shows a fit plot of fast direction as a function of frequency. The green curve shows the predicted data and the red curve with error bars shows the observed data. Figure 6.9 shows a matrix of misfit. Since all the data points are equally weighted, we expect the misfit is significantly dominated by small errors. According to 6.10, however, the observed data can not be fitted with the predicted curve. Since the error bar at 40 mHz and 55 mHz

are too small to fit the observed curve, these difference are acceptable. But the predicted data are lying out of the error bar at 25 mHz and 30 mHz. The fitting model still needs some optimizations.

Case 2: the data points are weighted by error.

We find the best fitting model when $\phi_1 = 80^\circ$ and $\phi_2 = 65^\circ$. Figure 6.12 shows a fit plot of fast direction as a function of frequency. The green curve shows the predicted data and the red curve with error bars shows the observed data. Figure 6.11 is a map of misfit. Compared with case 1, the misfit of case 2 are much more smaller. ϕ_1 decreases a lot from 110° to 80° while ϕ_2 changes from 55° to 65°. The fit plot looks better than Case 1. Every predicted point lies in the range of error bar. At low frequencies, though the predicted data are obviously smaller than the observed ones, the error bars are also larger.

Case 3: Set a threshold for error.

Like the previous test for strength of anisotropy, we will find out the best threshold among 2.5, 5, 10, 15 and 20. Figure 6.13 shows all the matrix when different thresholds are applied. For threshold equals to 2.5 and 2, the fit plot is the same with figure 6.12. For threshold equals to 10 and 15, the fit plot is shown in figure 6.14. When threshold is 20, the fit plot is the same with figure 6.10. Considering the 5 matrix plots, when the threshold gets larger, ϕ_1 gets larger but ϕ_2 gets smaller. The misfit also gets smaller with increasing threshold. When threshold equals to 10 and 15, we get a new fit plot that haven't appeared before (see figure 6.14). The observed data are almost fitted by the predicted data, but this fit is no better than Case 2. Here we choose a threshold as 5 to be

our best fit when $\phi_1 = 80^\circ$ and $\phi_2 = 65^\circ$.

Table 6.2: Result of various fit for the fast direction

Test number	error threshold	MF	VR	best fit(ϕ_1, ϕ_2)
Test 1, case 3	2.5	0.32	25.06%	80°, 65°
Test 2, case 3	5	0.31	25.29%	80°, 65°
Test 3, case 3	10	0.27	31.81%	90°, 60°
Test 4, case 3	15	0.22	40.39%	90°, 60°
Test 5, case 3	20	0.19	37.67%	110°, 55°
case 2	weighted with errors(no threshold)	0.32	24.98%	80°, 65°
case 1	equally weighted	76.94	56.60%	110°, 55°

Table 6.2 shows the result for all the tests in section 7.3. As it shows, the misfit decreases with the threshold while VR increases with the threshold.

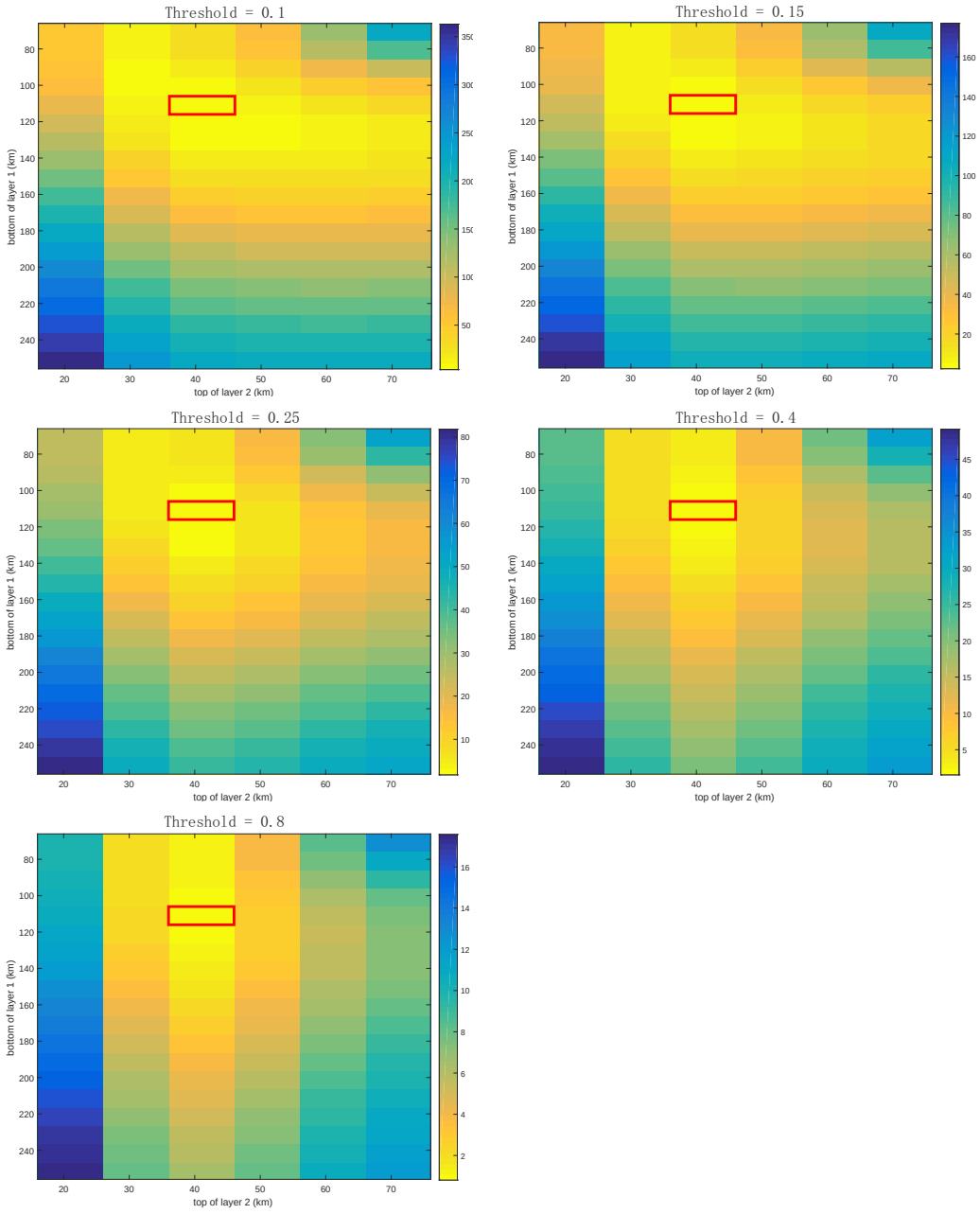

Figure 6.7: A matrix of misfit in case 3: The thresholds are 0.1, 0.15, 0.2, 0.4, 0.8. The red box shows the best fitting model.

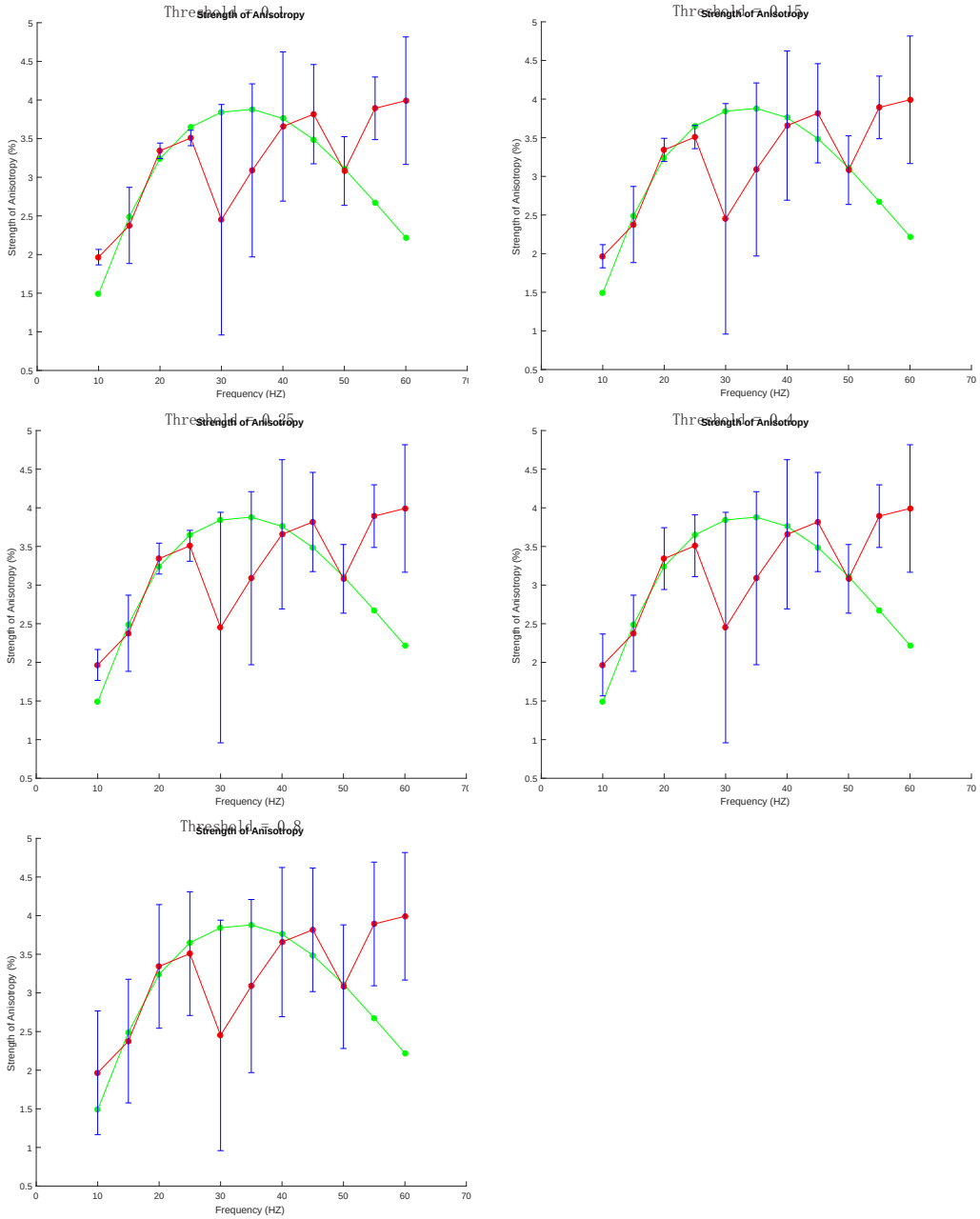

Figure 6.8: A fit plot of case 3: The thresholds are 0.1, 0.15, 0.2, 0.4, 0.8 respectively.

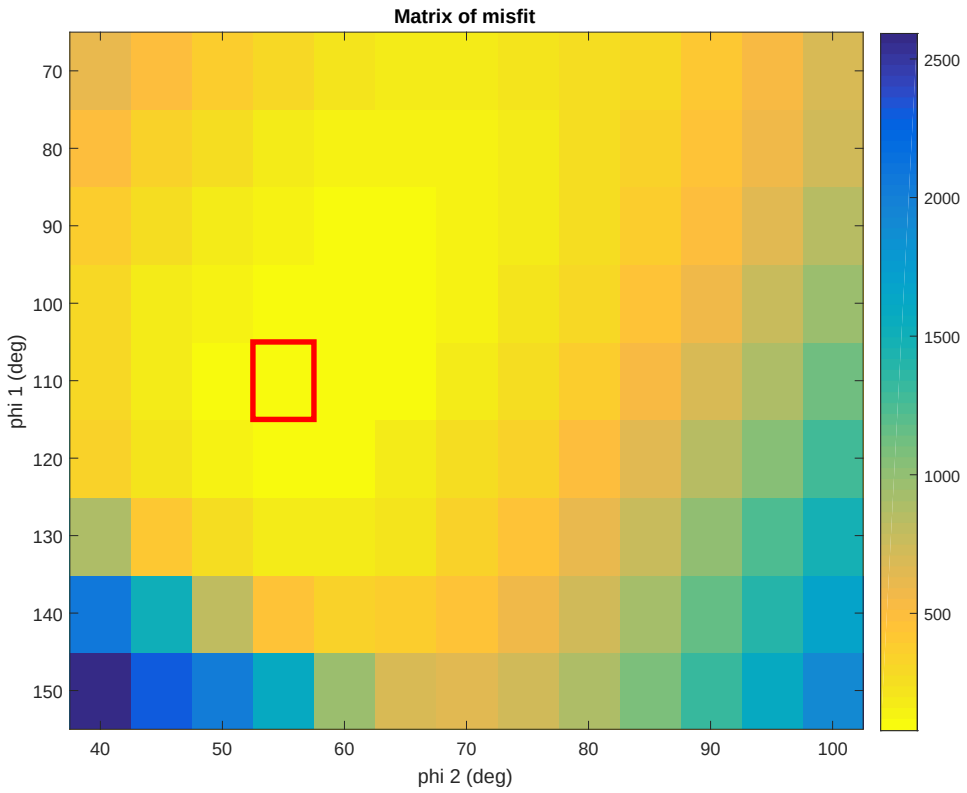

Figure 6.9: Case 1: a matrix of misfit equally weighted. ϕ_1 is varied from 70° to 150°. ϕ_2 is varied from 40° to 100°. The red box shows the best fitting model.

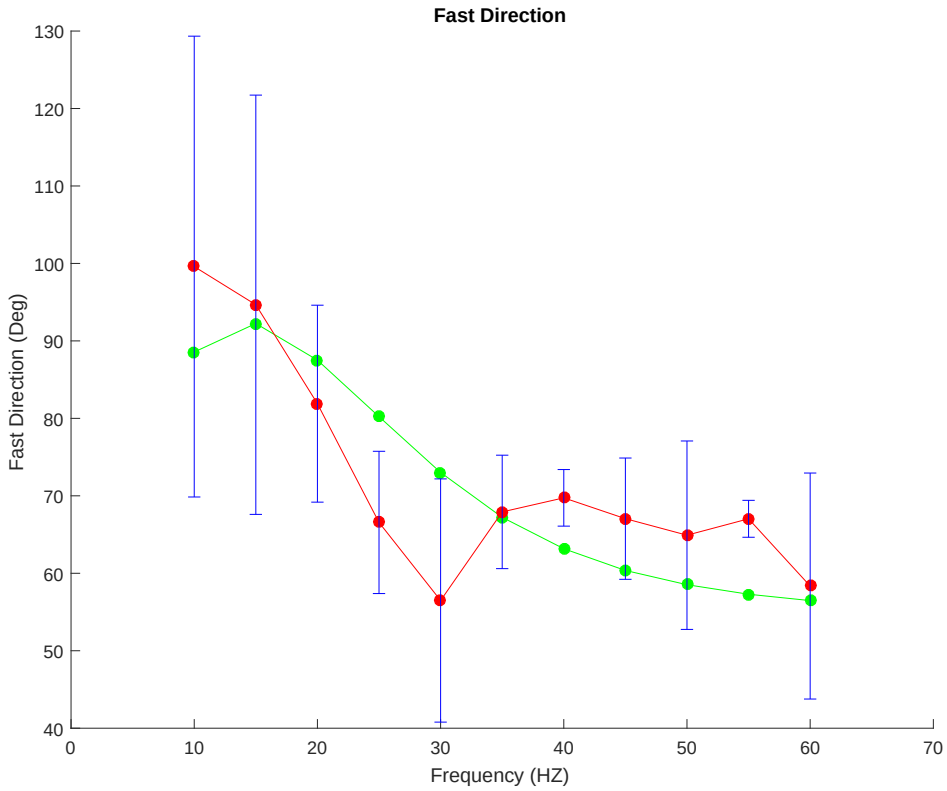

Figure 6.10: Case 1: a fit plot of fast directions. The fast direction predicted by the best fitting model is showed by the green curve. The observed fast direction is showed by the red curve with error bars. $\phi_1 = 110^\circ$ and $\phi_2 = 55^\circ$

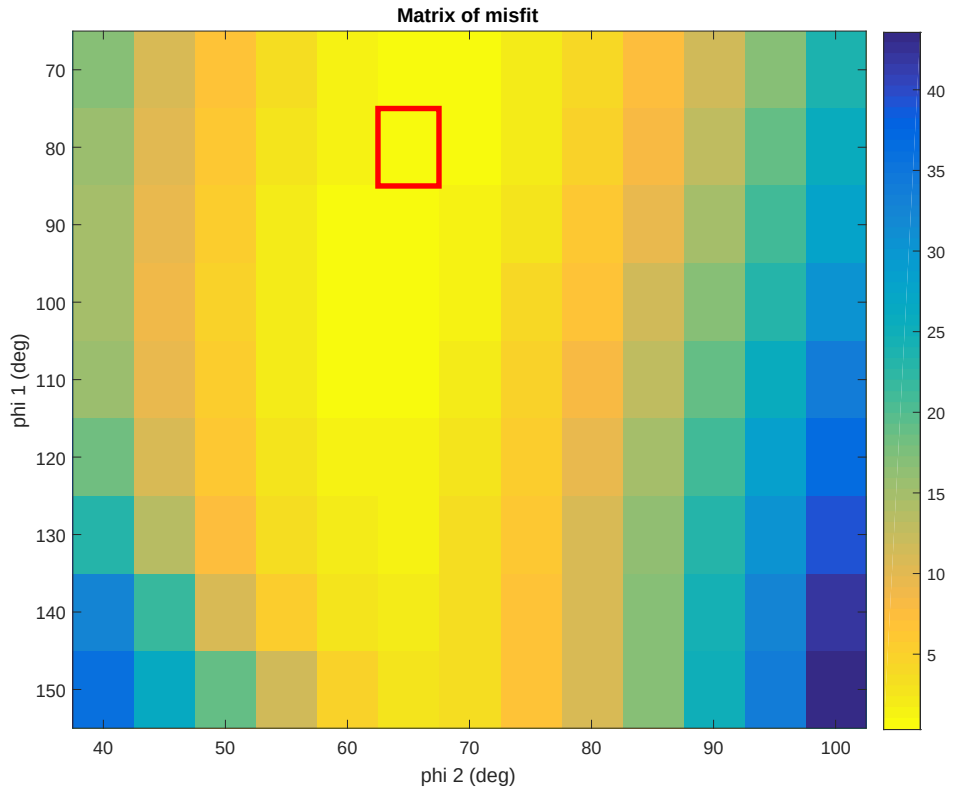

Figure 6.11: Case 2: A matrix of misfit when data are equally weighted: ϕ_1 is varied from 70° to 150°. ϕ_2 is varied from 40° to 100°.The red box shows the best fitting model.

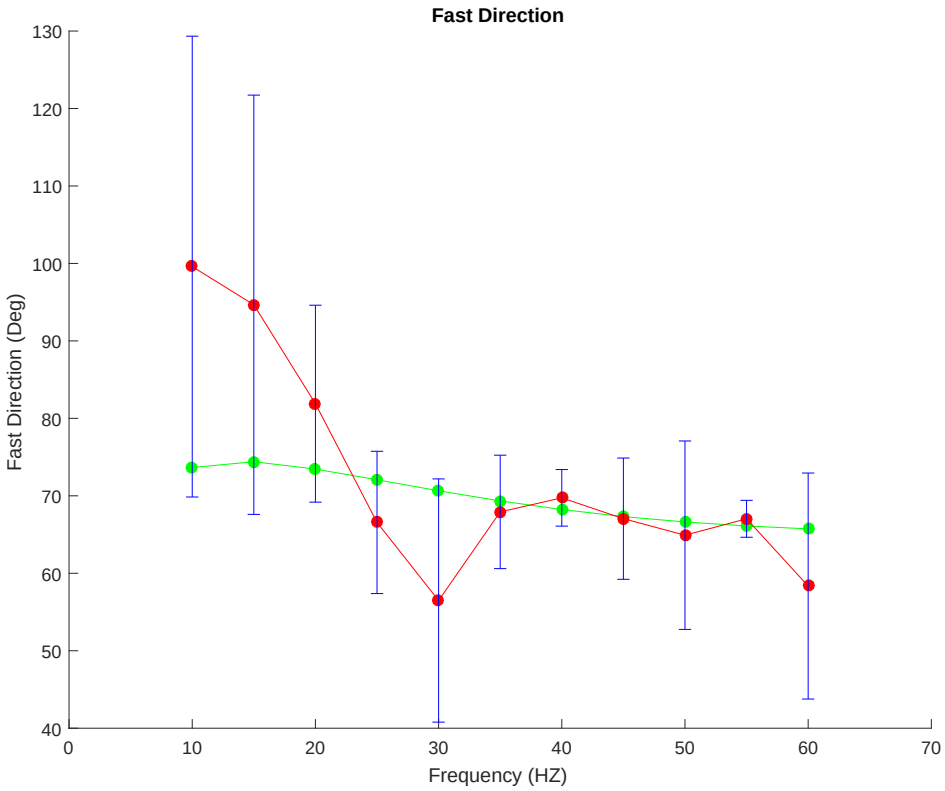

Figure 6.12: Case 2: A fit plot of fast directions: The fast direction predicted by the best fitting model is showed by the green curve. The observed fast direction is showed by the red curve with error bars. $\phi_1 = 80^\circ$ and $\phi_2 = 65^\circ$

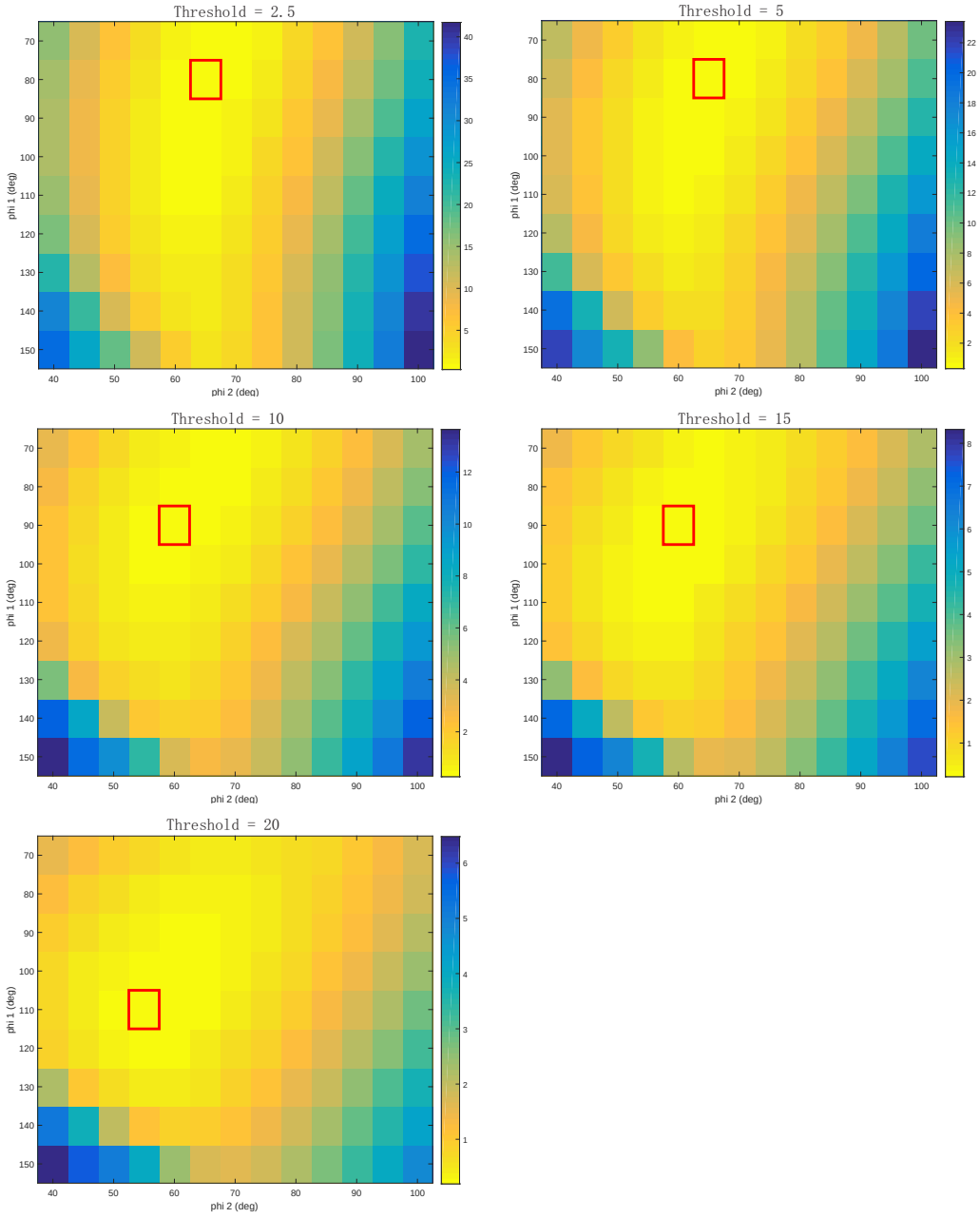

Figure 6.13: Case 3: A matrix of misfit equally weighted. The thresholds are 2.5, 5, 10, 15 and 20. The red box shows the best fitting model.

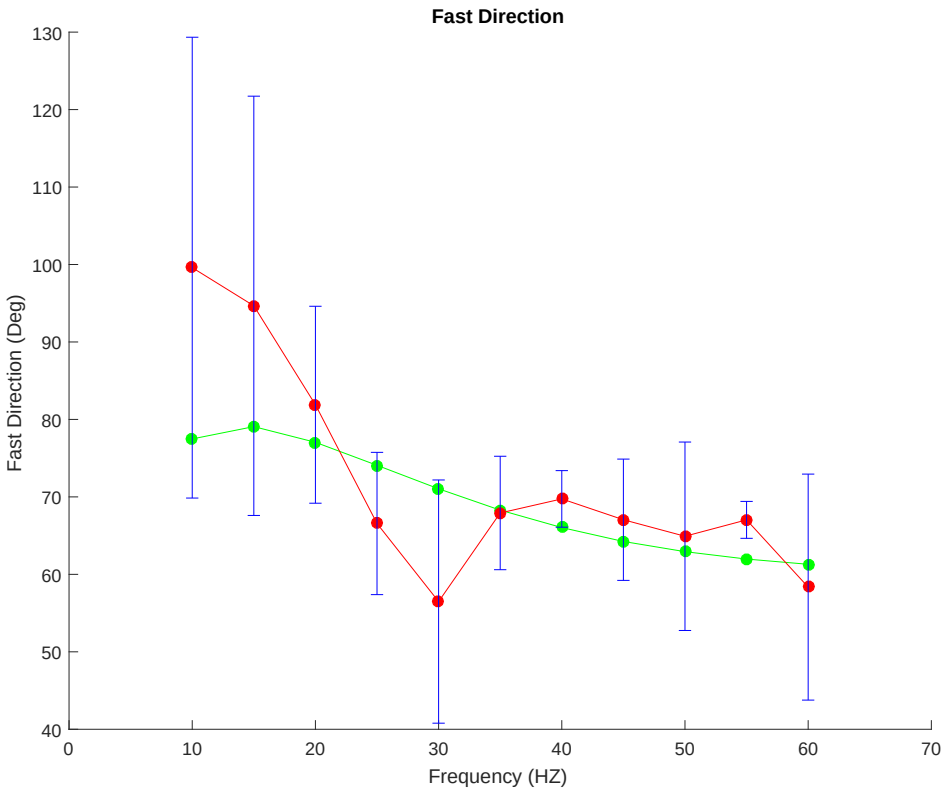

Figure 6.14: A map of misfit when data are weighted by their errors: The threshold is 10 and 15.

6.3 Calculate The Weighted Average of The Misfit of Fast Direction And The Misfit of Strength of Anisotropy

The minimum error threshold for SA is 0.4 and the minimum error threshold for DIR is 5°. In this case, $d_{12} = 71$ km. The top of layer 2 is varied from 21 km to 71 km with the step of 10 km. The bottom of layer 1 is varied from 51 km to 251 km with the step of 10 km. $\phi_1 = 80^\circ$ and $\phi_2 = 65^\circ$(these are best fitting model from section 7.3). $\theta_1 = \theta_2 = 80^\circ$. In this case, the misfit of strength of anisotropy and the misfit of fast direction are calculated separately. Then our objective function is a weighted average of these both misfits. We do a grid search for best fitting model just like the previous tests. All of the different weight are shown in table 6.3. And this how we calculate the weighted misfit:

$$MF = MF_{SA} \cdot \eta + MF_{DIR} \cdot \mu \tag{6.5}$$

in which $\eta + \mu = 100\%$

Table 6.3 shows five tests with different weights. Therefore, the results don't show obvious difference between various weight. All of the five tests get a best fitting model when the top of layer 2 is 41 km and the bottom of layer 1 is 91 km. Thus, in the following tests, we will use equal weights between the fast direction and the strength of anisotropy. Figure 6.13 shows the matrix plot. Figure 6.16 shows a fit plot for both the fast direction and the strength of anisotropy. The fast direction at frequencies higher than 15 mHz are fitted perfectly. But the fit for the strength of anisotropy is no very ideal. The predicted data are too large at the frequencies from 30 mHz to 35 mHz. And the

predicted data are too small when the frequency is higher than 50 mHz. So the next step can be exploring a change to d_{12}, the boundary between layer 1 and layer 2.

Table 6.3: Result of various fit for the fast direction

Test number	weight(η:μ)	MF	VR	best fit(top of layer 2, bottom of layer 1)
Test 0, case 3	10:1	1.73	15.01%	41 (km), 91 (km)
Test 1, case 3	4:1	1.57	11.66%	41 (km), 91 (km)
Test 2, case 3	2:1	1.36	7.56%	41 (km), 91 (km)
Test 3, case 3	1:1	1.11	2.44%	41 (km), 91 (km)
Test 4, case 3	1:2	0.85	-2.68%	41 (km), 91 (km)
Test 5, case 3	1:4	0.69	-6.77%	41 (km), 91 (km)

DIR, rather than SA, is better fitted to data even though we are using a 10:1 weight in case 0. We do not pay attention to VR. when the weight is 1:1, the misfit is relatively small. And we do not need a larger weight on DIR. So we choose an equal weight when calculating the average of the misfit of fast direction and the misfit of strength of anisotropy.

6.4 Triangle 2 in PLUME Phase 2 Network

The data set used in Chapter 4, section 4.2 is from triangle 2, provided by Gabi. Triangle 2 is formed by the stations: PL43(26.7781° N 155.7646° W), PL44(25.5928° N 152.7643° W), PL46(24.3082° N 156.9659° W). We get the centroid of triangle 2 by taking the average of the coordinates of these three stations. The coordinate of the centroid is (25.5597° N 155.1649° W). Figure 6.17 is a map of triangle 2.

Figure 6.18 shows the results of triangle 2. A plot of the fast direction is shown

in the left panel and the plot of the strength of anisotropy is shown in the right panel. The fast direction varies from 103° to 61.8°. At the frequency of 10 mHz, the fast direction is close to 123°(the present-day plate motion). And at the frequency from 30 mHz to 60 mHz, the fast directions are near 76°(the fossil plate motion). However, at the frequency of 20 mHz and 25 mHz, the results is out of our expectation. The strength of anisotropy varies from 3.36% to 8.65%. It stays constantly at around 3.5% when the frequency is from 10 mHz to 25 mHz. Then it has a maximum at 55 mHz.

Case 1: Do a grid search for the top of layer 2 and the bottom of layer 1, but $d_{12} = 51$ km. Only fit the strength of anisotropy. For all of the following fits, the error threshold for strength of anisotropy is 0.4, the error threshold for fast direction is 5.

In this case, $d_{12} = 51$ km. The top of layer 2 is varied from 11 km to 14 km with the step of 1 km. The bottom of layer 1 is varied from 51 km to 171 km with the step of 10 km. $\phi_1 = 123^\circ$ and $\phi_2 = 76^\circ$. $\theta_1 = \theta_2 = 80^\circ$

A matrix plot is shown in figure 6.19, the best fitting model is 81 km (bottom of layer 1), 21 km (top of layer 2). Although the best fitting model is shown at the edge of a matrix, the fit plot (figure 6.20) indicates a really good fit.

Case 2: Fit the fast direction.

ϕ_1 is varied from 70° to 150° with the step of 10°. ϕ_2 is varied from 40° to 100° with the step of 5°. Then we use the best fitting model from the last case. The top of layer 2 is 21 km, the bottom of layer 1 is 81 km. $d_{12} = 51$ km.

Figure 6.21 shows the matrix plot of the misfit. The best fitting model is $\phi_1 = 80°$, $\phi_2 = 75°$. Figure 6.22 shows the fit plot to data. This fit is acceptable though one data point at 10 mHz can not be fitted.

Case 3: Do the same with case 1 and 2 but fit the strength of anisotropy and the fast direction with equal weights.

The bottom of layer 1 is varied from 51 km to 251 km with the step of 10 km. The top of layer 2 is varied from 21 km to 51 km with the step of 1 km. $\phi_1 = 80°$, $\phi_2 = 75°$, $d_{12} = 51$ km.

Figure 6.23 shows the matrix plot of the misfit. The best fitting model is 21 km (top of layer 2), 61 km (bottom of layer 1). Figure 6.24 shows the fit plot to data. Both the fit to DIR data and the fit to SA data are acceptable.

6.5 Results of All The Other Triangles

We do other triangles with similar method, the results are shown in table 6.4.

Table 6.4: Result of the fit for SA and DIR with equal weight

Triangle number	MF	VR	best fit(top of layer 2, bottom of layer 1)
Triangle 1	0.97	26.48%	31 (km), 171 (km)
Triangle 2	0.49	36.62%	21 (km), 61 (km)
Triangle 3	0.85	41.47%	51 (km), 161 (km)
Triangle 4	0.73	2.44%	41 (km), 91 (km)
Triangle 5	3.96	-202.27%	41 (km), 101 (km)
Triangle 6	0.99	-46.94%	31 (km), 91 (km)
Triangle 11	1.84	-37.04%	41 (km), 161 (km)
Triangle 15	0.72	-6.77%	41 (km), 191 (km)

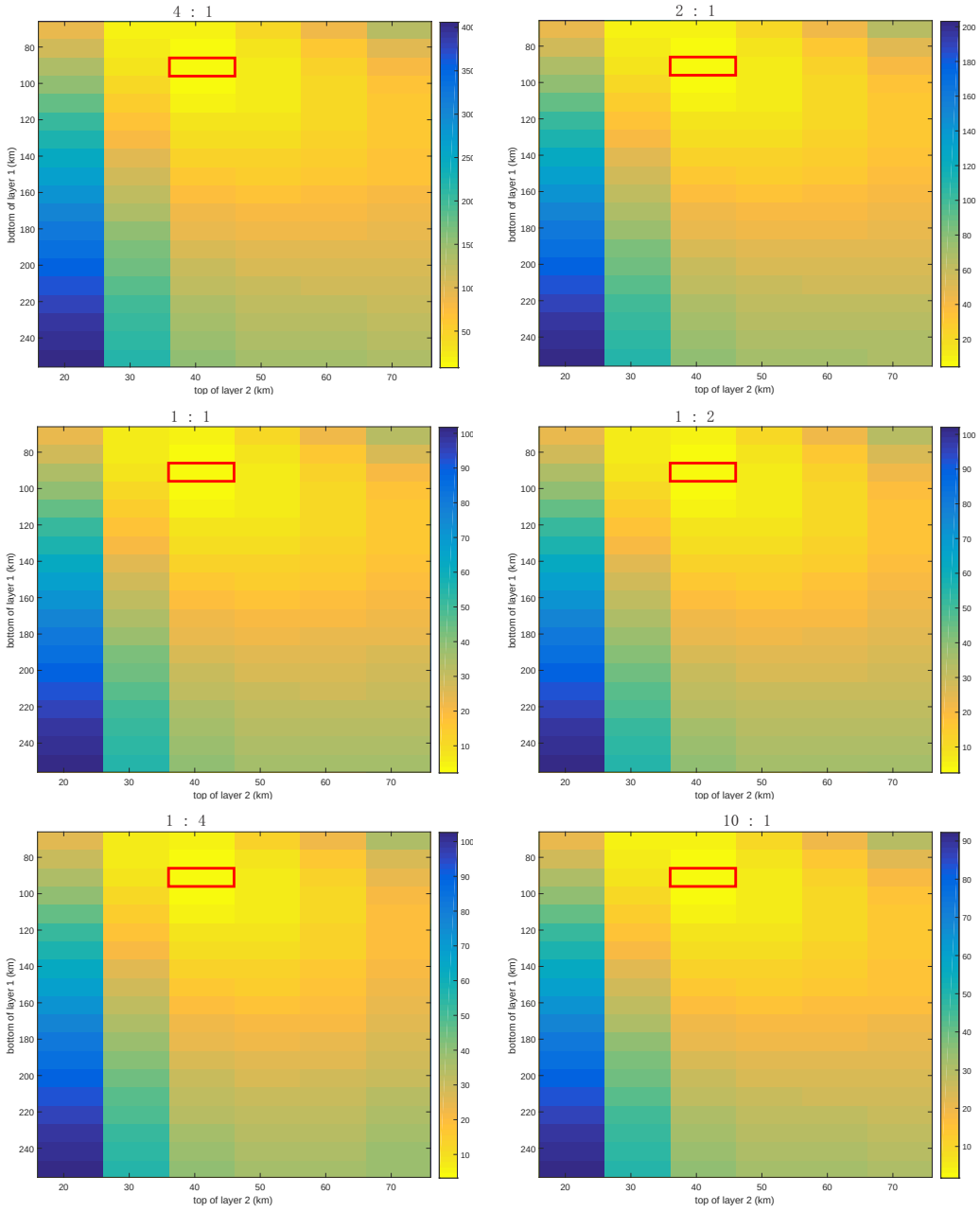

Figure 6.15: A matrix of misfit with different weights. The red box shows the best fitting model.

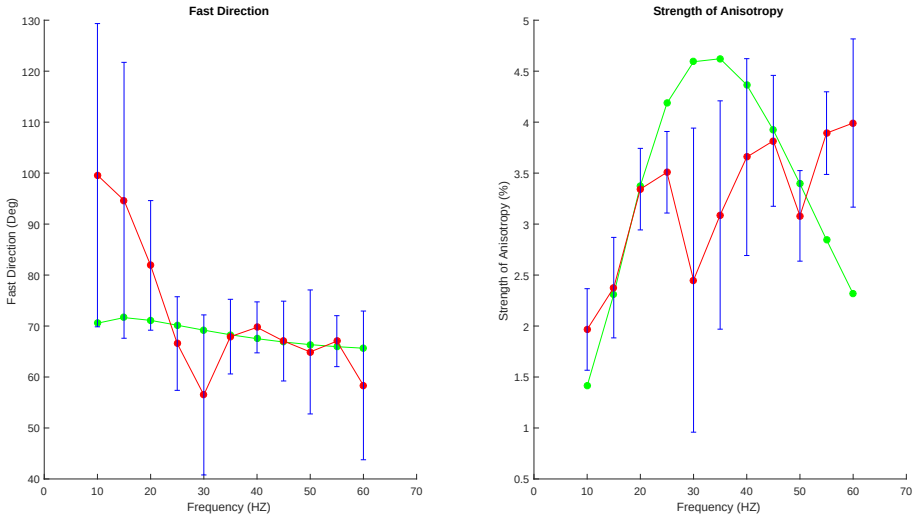

Figure 6.16: A fit plot of both the fast direction(left panel) and the strength of anisotropy(right panel). The red curves with error bars are the observed data and the green curves are predicted data. The top of layer 2 is 41 km and the bottom of layer 1 is 91 km

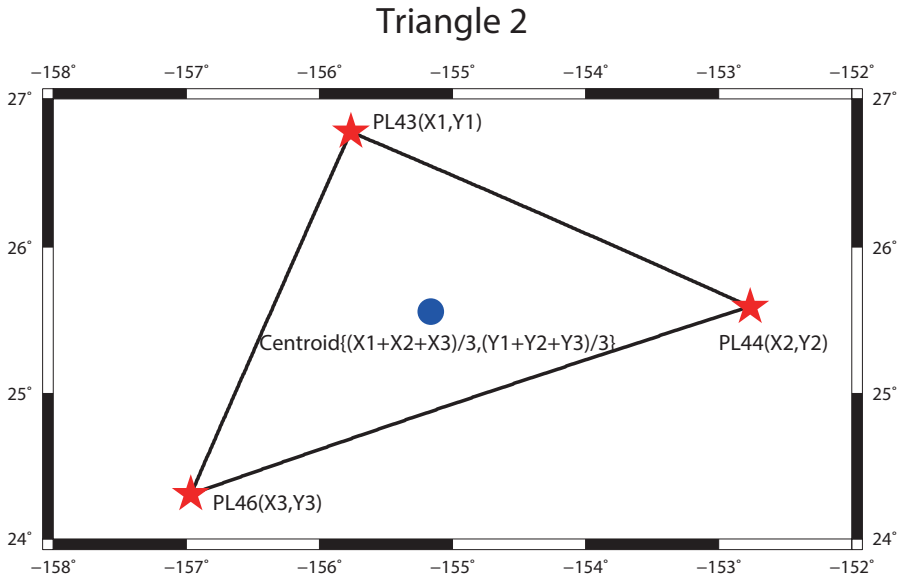

Figure 6.17: A map of triangle 2 and its centroid: the coordinate of the centroid is determined as the average of the coordinates of stations PL43, PL44 and PL46.

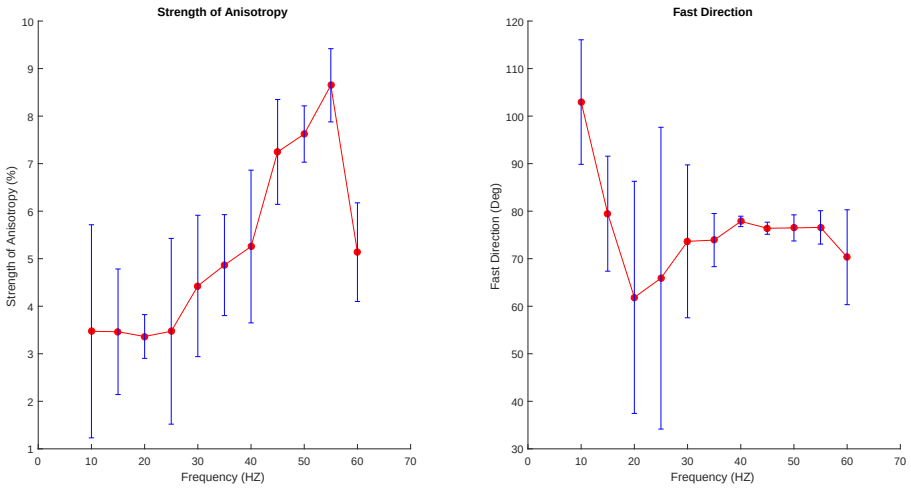

Figure 6.18: Result of triangle 2: the left panel shows the fast direction as a function of frequency and the right panel shows the strength of anisotropy as a function of frequency.

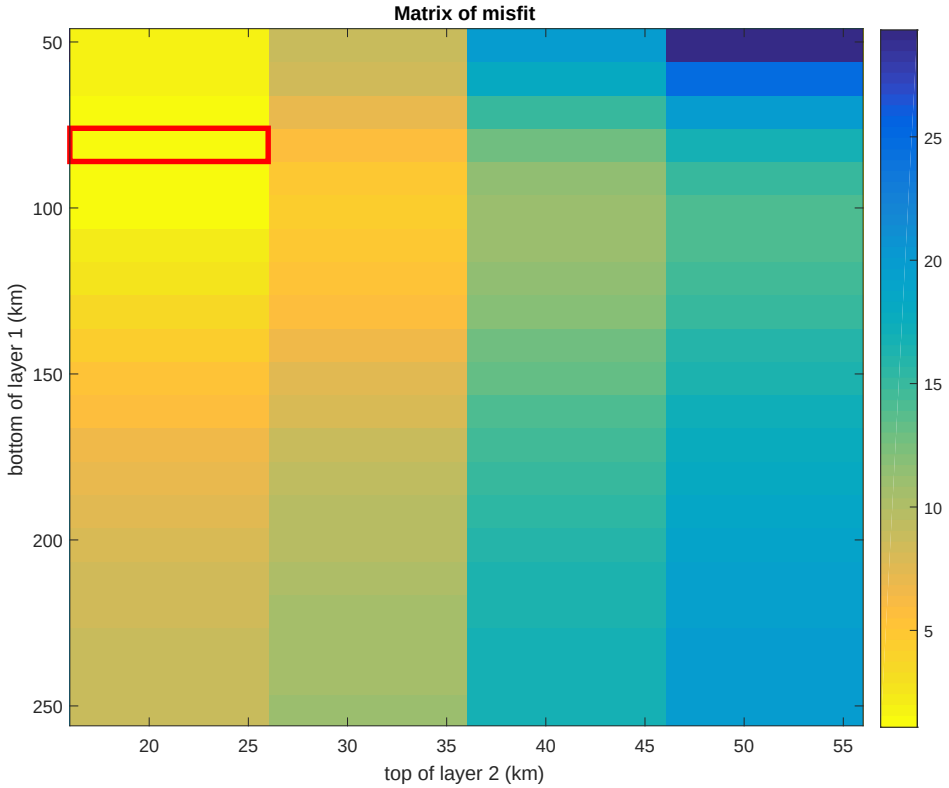

Figure 6.19: A matrix of misfit for triangle 2: The bottom of layer 1 is varied from 51 km to 251 km. The top of layer 2 is varied from 21 km to 51 km.

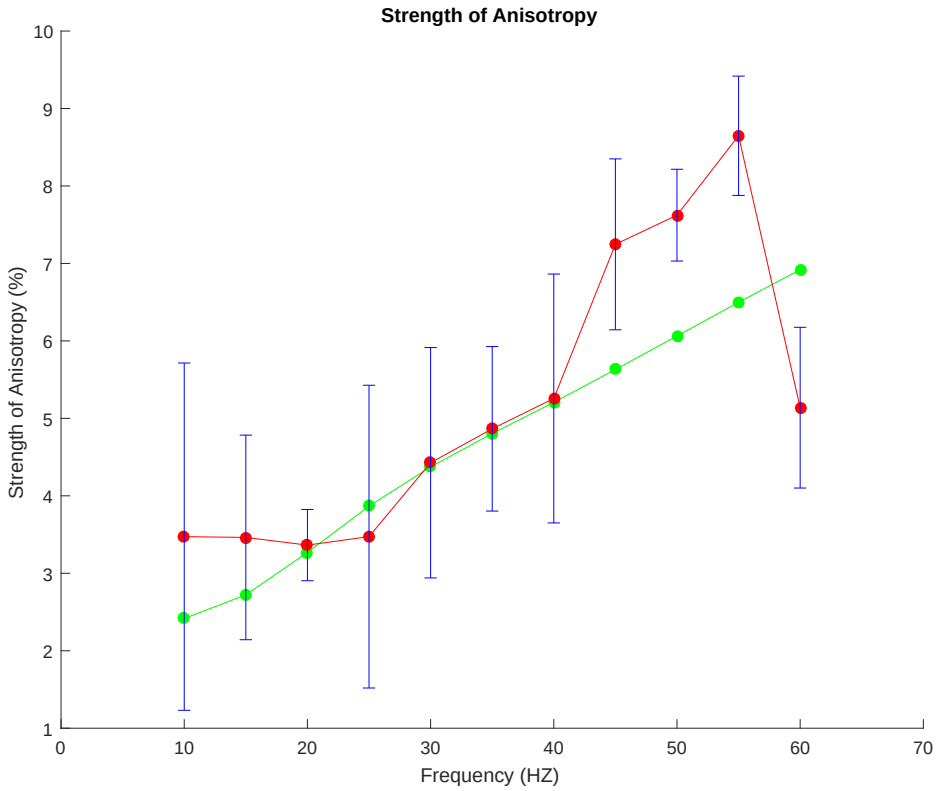

Figure 6.20: A fit plot of SA: The strength of anisotropy predicted by the best fitting model is showed by the green curve. The observed strength of anisotropy of triangle 2 is showed by the red curve with error bars.

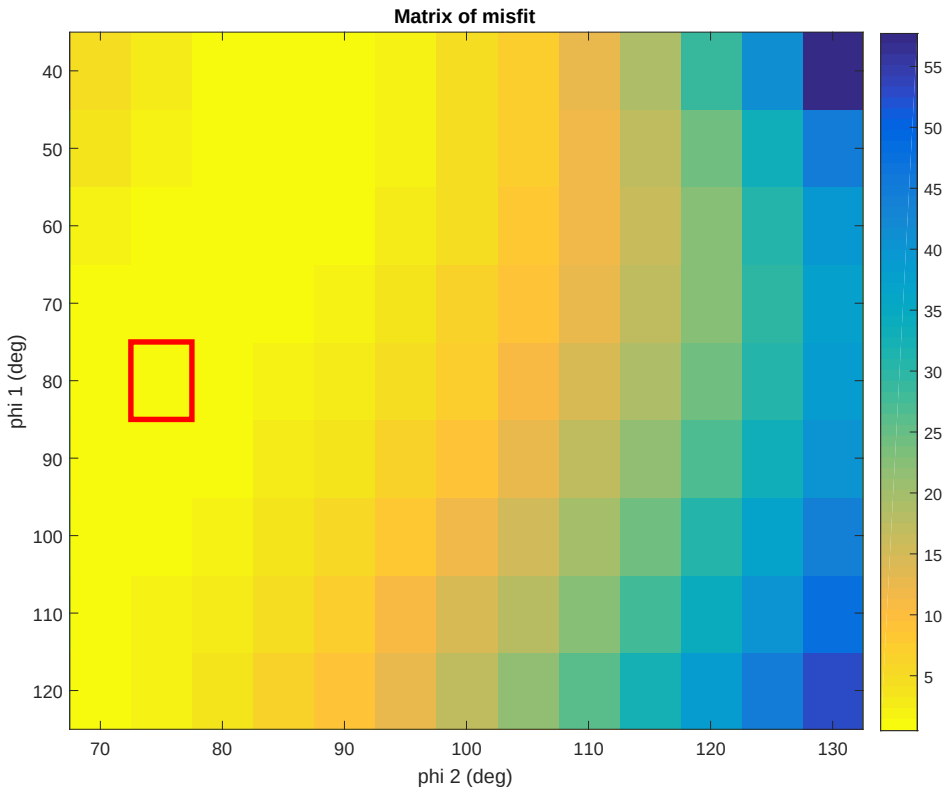

Figure 6.21: A matrix of misfit for triangle 2: The bottom of layer 1 is varied from 51 km to 171 km. The top of layer 2 is varied from 21 km to 51 km.

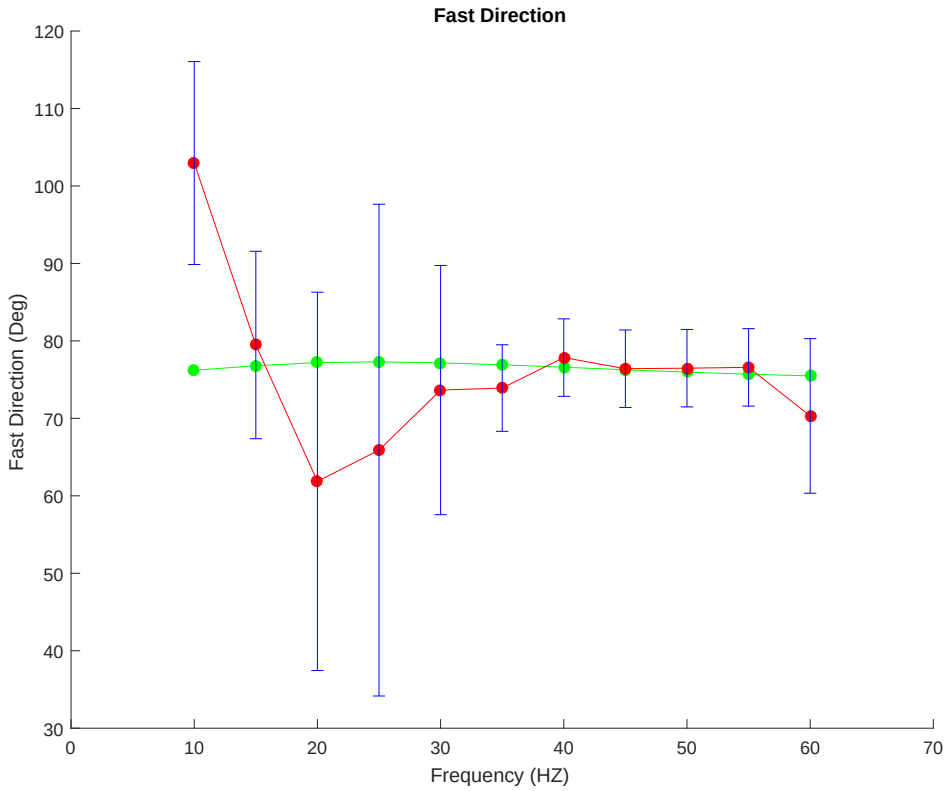

Figure 6.22: A fit plot of DIR: The predicted fast direction is showed by the green curve. The observed fast direction is showed by the red curve with error bars. $\phi_1 = 80^\circ$, $\phi_2 = 75^\circ$

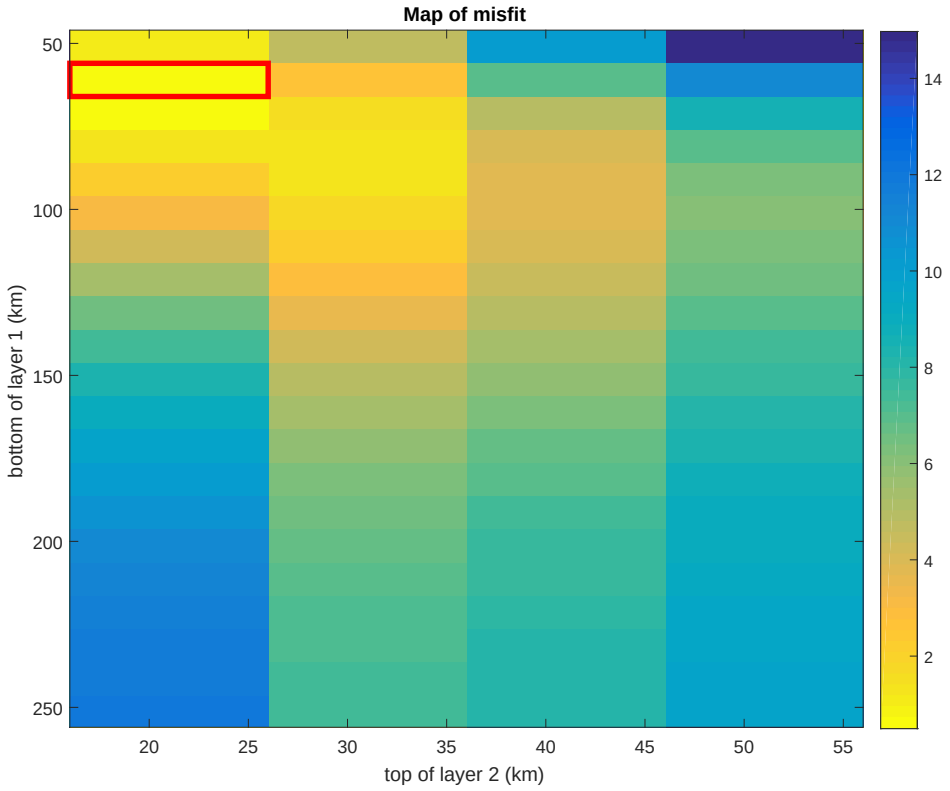

Figure 6.23: A matrix of misfit for triangle 2: The bottom of layer 1 is varied from 51 km to 171 km. The top of layer 2 is varied from 21 km to 51 km.

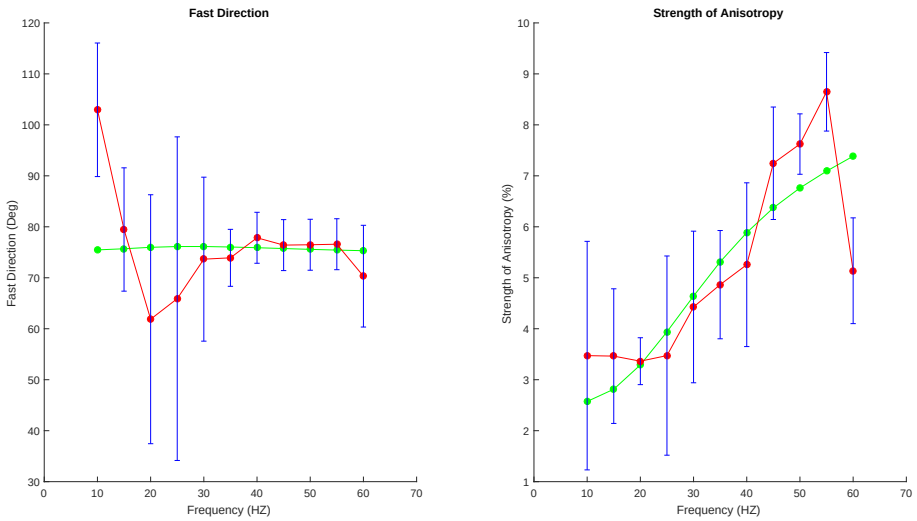

Figure 6.24: A fit plot of DIR: The predicted curve is showed by the green curve. The observed data is showed by the red curve with error bars. The top of layer 2 is 21 km, the bottom of layer 1 is 61 km

Chapter 7

Discussion of Results

In this chapter, I summarize the modeling results for all 27 triangles show in Figure 4.2.

For time-saving purposes my advisor automated the grid search an processed all 27 triangles. She used a slightly different approach though. Comparison of her and my results for triangle 4 and 2 and a few others indicate that results may vary a bit but are consistent when parameters are well-constrained. Gabi's approach had 4 main steps where she started in the same way I did:

- step 1: Grid search for SA with default $\phi_1 = 124^o$; $\phi_2 = 76^o$ to get best-fitting bottom of layer 1 and top of layer 2.

- step 2: Use result for bottom of layer 1 and top of layer 2 and do grid search for DIR to get best-fitting ϕ_1 and ϕ_2.

- step 3: stop if both SA and DIR data are fit to within error bars or iterate for

another grid search for SA using ϕ_1 and ϕ_2 obtained from Step 2.

- step 4: if there are obvious outliers in the data, edit data and repeat steps 1-3.

The final four model parameters, and the combined thickness of the two anisotropic layers are summarized for each triangles in table 7.1.

In Figure 7.1, I show the depth of the top of the upper layer (layer 2), i.e. the depth above which the mantle and crust beneath Hawaii is isotropic. Though local variations may occur, and overall coherent pattern emerges: to the south and southwest of the islands, anisotropy starts at a greater depth than along the islands and toward the north. In the north, this depth is between 20 km and 45 km. We assume that this area has normal oceanic crust so the Moho should be at a depth of about 12 km (5.5 km water plus 6.5 km solid crust). Near and beneath the islands, the Moho is at 25 km depth. We therefore conclude that the top of our layer 2 is in the mantle and not in the crust. In the other areas the top of anisotropy is much deeper, at about 70 km. This depth is already well in the lower lithosphere, maybe even close to the lithosphere-asthenosphere boundary.

While there is some obvious coherency in Figure 7.1, we are unable to draw a coherent picture for the combined thickness of anisotropy (Figure 7.2). It seems that in the south and west, anisotropy can be very thin (about 20 km or so). This is consistent with the data, i.e. small values of strength of anisotropy across all frequencies in the corresponding triangles. However, some of these triangles can be surrounded by triangles with very thick anisotropy (greater than 150 km). To refute one or the other, a very detailed quality analysis of the 2ψ and 4ψ fits would be required which is beyond the scope of this MS thesis. We find less extreme values toward the north where we would

expect unaltered, more typical oceanic lithosphere. Here, the total thickness of anisotropy is more in the range between 50 and 100 km.

We now turn our attention to the azimuth of the symmetry axis of the tilted transversely isotropic Pyrolite mantle model that we used in the modeling. Figure 7.3 shows the azimuth, ϕ of the upper layer (layer 2). Here we would expect to see an overall alignment with the fossil spreading direction because it froze into the younger and thinner oceanic mantle. This is essentially what we see. The azimuth is also quite coherent across the entire PLUME network, with a few exceptions. To the far west, the azimuth seems to align more with the current plate motion direction but we see no obvious systematic connection to the top of layer 2 or total thickness of anisotropy. Toward the south, the pattern is less coherent but azimuths tend to over-rotate, i.e. may have some component of the current plate-motion direction. Since both in the west and southeast of the islands, anisotropy starts at a greater depth, there appears to be less imprint from the fossil direction. Perhaps, this is an indication that an upwelling mantle plume removed some of this imprint. The area affected here would be much larger that what was imaged in the isotropic tomography by Laske et al. (2011) but would be consistent with the concept of broad-scale parabolic mantle flow in Figure 3.7.

The situation is much more incoherent for the lower layer (Figure 7.4). In the north, the fast direction still aligns with the fossil plate motion direction. But along the island chain, it aligns with the current plate motion. In the west, in some triangle the fast direction still aligns with the fossil spreading direction but some do not. Again, this inconsistency may result from vastly different thicknesses of anisotropy found between adjacent triangles, and we cannot fully explain this at this time. In the south of the islands, the fast directions show significant rotation away from the fossil spreading direction, and

is perhaps perpendicular to the present-day plate motion. Again, this would be consistent with the plume-related parabolic mantle flow.

To summarize, we find a more coherent pattern of the azimuth of anisotropy in the upper layer than in the lower layer that broadly aligns with the fossil spreading direction. In the layer beneath, the picture is less coherent but there are indications that suggest that we image a deeper plume-related parabolic mantle flow. This is also consistent with the patterns in the 'raw' maps in Figure 4.12 where patterns are more coherent for higher frequencies that sense shallower structure than at lower frequencies. If this was the case, that flow may be narrower than expected because our results to the far north of the islands show no deviation from the expected motion of the spreading Pacific plate.

The results for the lower layer may have to be taken with some caution. As Figure 4.12 indicates, some results at the lower frequencies are less certain than at high frequencies. Consequently, our results in chapter 7 may be less certain for layer 1 than they are for layer 2. Nevertheless, it seems that even the upper layers exhibits some form of deviation of anisotropy expected for a uniformly spreading Pacific plate.

The results are shown in table 7.1 :

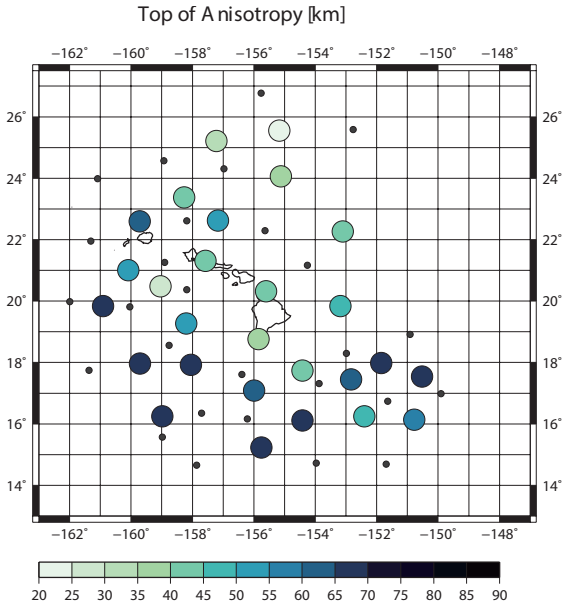

Figure 7.1: Depth of the top of the upper layer (layer 2). Color-coded symbols are plotted at the centroid location of each of the 27 triangles.

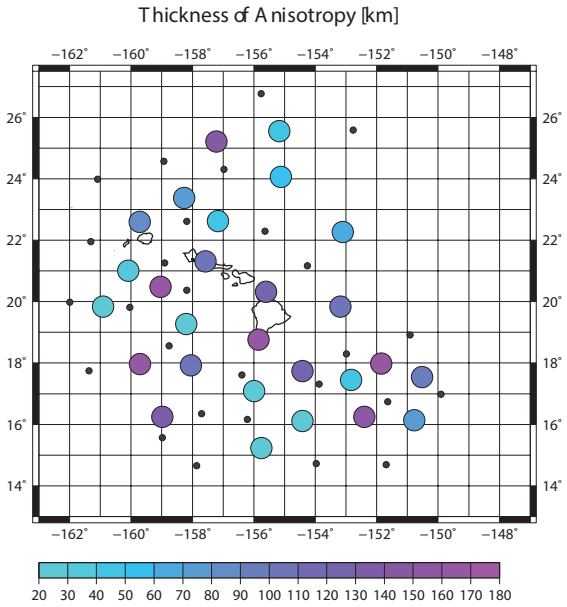

Figure 7.2: Combined thickness of both anisotropic layers. See Figure 7.1 for details.

Table 7.1: Result of all 27 triangles

Triangle number	centroid longitude	centroid latitude	total thickness (km)	bottom of layer 1 (km)	top of layer 2 (km)	fast direction of layer 1 (°)	fast direction layer 2 (°)
1	−157.2206°	22.2210°	145	175	30	85	65
2	−155.1649°	25.5597°	40	60	20	80	75
3	−159.7157°	22.5997°	60	120	60	55	85
4	−158.2665°	23.3839°	70	110	40	110	55
5	−157.1672°	22.6245°	45	95	50	125	65
6	−155.1213°	24.0665°	55	90	35	80	65
7	−160.9089°	19.8413°	20	85	65	85	115
8	−160.0869°	21.0137°	35	85	50	50	65
9	−159.0415°	20.4869°	165	190	25	140	60
10	−157.5711°	21.3135°	105	150	45	105	75
11	−153.1042°	22.2685°	65	105	40	125	90
12	−159.7050°	17.9728°	160	225	65	115	110
13	−158.0444°	17.9286°	105	170	65	85	115
14	−158.2030°	19.2703°	25	75	50	30	55
15	−155.8491°	18.7644°	160	195	35	80	40
16	−155.5981°	20.3250°	125	165	40	135	70
17	−153.1772°	19.8379°	100	145	45	130	75
18	−158.9765°	16.2531°	130	195	65	90	90
19	−155.9858°	17.0936°	15	75	60	55	45
20	−154.4130°	17.7440°	120	160	40	85	45
21	−152.8300°	17.4512°	45	105	60	70	75
22	−151.8452°	17.9846°	160	225	65	50	30
23	−150.5182°	17.5468°	95	160	65	40	140
24	−155.7490°	15.2337°	25	90	65	110	50
25	−154.4188°	16.1184°	15	80	65	130	55
26	−152.3975°	16.2480°	155	200	45	30	90
27	−150.7752°	16.1392°	70	125	55	60	70

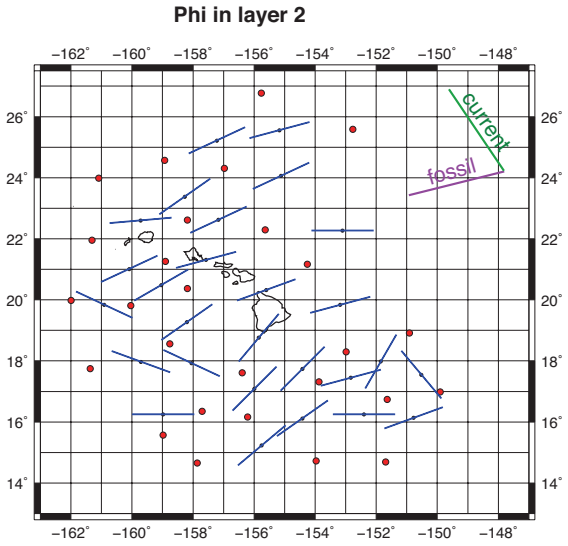

Figure 7.3: Azimuth of the symmetry axis of anisotropy, ϕ_2, in the upper layer (layer 2). Arrows have the same length so do NOT indicate the strength of horizontal anisotropy is in that layer. Also marked are the fossil (purple) and current (green) plate motion directions.

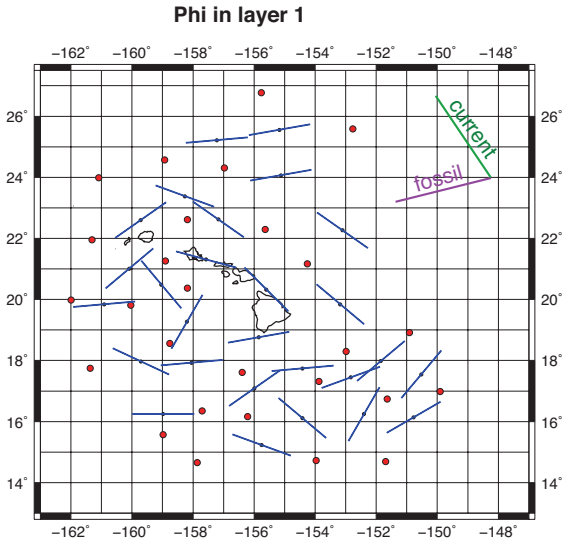

Figure 7.4: Azimuth of the symmetry axis of anisotropy, ϕ_1, in the lower layer(layer 1). See Figure 7.3 for details.

Bibliography

Crampin, S., 1977, A review of the effects of anisotropic layering on the propagation of seismic waves, Geophysical Journal of the Royal astronomical Society, 49, 9-27.

Dziewonski, A.M. and D.L. Anderson, 1981, Preliminary reference Earth model. Physics of the Earth and Planetary Interiors, 25, 297-356.

Chojnacki, P., Laske, G., Orcutt, J.A., Wolfe, C.J., Collins, J.A., Solomon, S.C., Detrick, R.S., Bercovici, D and Erik H. Hauri, 2011, Rayleigh Wave Azimuthal anisotropy Observed During the Hawaiian PLUME Project, unfinished manuscript.

Gripp, A E. and R, G. Gordon, 2001, Young tracks of hotspots and current plate velocities. Geophysical Journal International, 150, 231-361.

Jackson, E.D. and H.R. Shaw, 1975, Stress fields in central portions of the Pacific plate: Delineated in time by linear volcanic chains, Journal of Geophysical Research, 80, 1861-1874.

Laske, G. "Probing the Hawaiian Hot Spot With New Broadband Ocean Bottom Instruments." Eos 13 Oct. 2009: 362-63.

Laske, G. ”The Hawaiian PLUME Project.” U.C. San Diego. (http://igppweb.ucsd.edu/∼ gabi/plume.html)

Laske, G., Markee, A., Orcutt, J.A., Wolfe, C.J., Collins, J.A., Solomon, S.C., Detrick, R.S., Bercovici, D and Erik H. Hauri, 2011, Asymmetric shallow mantle structure beneath the Hawaiian Swell - evidence from Rayleigh waves recorded by the PLUME network, Geophysical Journal International, 187, 1725-1742.

Montagner, J.P. and H.C. Nataf, 1986, A simple method for inverting the azimuthal anisotropy of surface waves, Journal of Geophysical Research, 91, 511 - 520.

Montagner, J.P. and H.C. Nataf, 1988, Vectorial tomography - I. theory, Geophysical Journal, 94, 295-07.

Morgan, W.J., 1971, Convection plumes in the lower mantle, Nature, 230, 42-3.

Searle, R.C., Holcomb, R.T., Wilson, J.B., Holmes, M.L., Whittington, R.J., Kappel, E.S., McGregor, B.A. and A.N. Shor, 1993, The Molokai Fracture Zone near Hawaii, and the Late Cretaceous Change in Pacific/Farallon Spreading Direction. in: ”The Mesozoic Pacific: Geology, Tectonics, and Volcanism”, AGU Geophysical Monograph 77, 155-169.

Stein, S. and Wysession, M., 2002, An Introduction to Seismology, Earthquakes and Earth Structure, 1st edition, Wiley-Blackwell.

Shearer, P.M., 2009, Introduction to Seismology, 2nd edition, Cambridge University Press.

Smith, M.L. and F.A. Dahlen, 1973, The azimuthal dependence of Love and Rayleigh wave propagation in a slightly anisotropic medium, Journal of Geophysical Research, 78, 3321-3333.

Maupin, V. and Park, J., 2015, "Theory and Observations Wave Propagation in Anisotropic Media" in Schubert, G. (ed.) "Seismology and Structure of the Earth: Treatise on Geophysics(2nd edition)", Elsevier B.V.

Turcotte, D. L., and G. Schubert, 2014, Geodynamics, 3rd edition, Cambridge University Press.

Wilson, J.T., 1963, Evidence from islands on the spreading of ocean floors, Nature, 197, 536-538.

Walker, K.T., Bokelmann, G.H.R. and S.L. Klemperer, 2001, Shear-wave splitting to test mantle deformation models around Hawaii, Geophysical Research Letters, 28, 4319-4322.

Appendix A

Other triangles in PLUME Phase 2 Network

Table 1a, 1b, 1c show the results of fitting in 3 steps respectively. For all of the fits for triangles, the error threshold for strength of anisotropy is 0.4, the error threshold for fast direction is 5.

Table 1a: Step 1: Result of the fit for SA

Triangle number	MF	VR	best fit(top of layer 2, bottom of layer 1)
Triangle 1	0.59	10.00%	31 (km), 191 (km)
Triangle 3	2.76	-137.69%	51 (km), 131 (km)
Triangle 6	0.80	-14.21%	31 (km), 121 (km)
Triangle 11	2.84	-109.64%	41 (km), 131 (km)
Triangle 15	3.51	13.59%	41 (km), 201 (km)

A.1 Triangle 1

For step 1, the misfit is 0.59 which is much smaller than most of the other triangles. The data points from 10 mHz to 50 mHz can be fitted perfectly. For step 2, the prediction

Table 1b: Step 2: Result of the fit for DIR

Triangle number	MF	VR	best fit(ϕ_1, ϕ_2)
Triangle 1	1.27	43.33%	100°, 65°
Triangle 3	0.47	89.61%	50°, 120°
Triangle 6	0.38	38.08%	100°, 65°
Triangle 11	0.07	93.38%	140°, 80°
Triangle 15	0.36	48.22%	70°, 35°

Table 1c: Step 3: Result of the fit for SA and DIR with equal weight

Triangle number	MF	VR	best fit(top of layer 2, bottom of layer 1)
Triangle 1	0.97	26.48%	31 (km), 171 (km)
Triangle 2	0.49	36.62%	21 (km), 61 (km)
Triangle 3	0.85	41.47%	51 (km), 161 (km)
Triangle 4	0.73	2.44%	41 (km), 91 (km)
Triangle 5	3.96	-202.27%	41 (km), 101 (km)
Triangle 6	0.99	-46.94%	31 (km), 91 (km)
Triangle 11	1.84	-37.04%	41 (km), 161 (km)
Triangle 15	0.72	-6.77%	41 (km), 191 (km)

can not fit the data at 20 mHz and 55 mHz. The misfit a lot larger than other triangles. Variance reduction is 43.33%. For step 3, the bottom of layer 2 of best fitting model changes from 171 km to 191 km. The misfit is acceptable but the variance reduction is negative.

A.2 Triangle 3

In step 1, SA is perfectly fitted. In step 2, the prediction is a lot larger than DIR data, but they almost lie in the range of the error bars. The variance reduction is 89.61%, relative it is a better than others. In step 3, the fit plot does not change obviously but the best fitting model has been changed.

A.3 Triangle 6

In step 1, it is a good fit and the misfit is 0.80. However, the variance reduction is negative. In step 2, only the first point can not be fitted. In step 3, the fit plot to DIR gets better than step 2. The misfit is good. But the variance reduction is negative.

A.4 Triangle 11

In step 1, the data 25 mHz, 45 mHz and 60 mHz can not be fitted. The misfit is large and the variance reduction is negative. In step 2, the fit to data is perfect. The misfit is as small as 0.07 and the variance reduction is 93.38%. In step 3, the misfit is large and the variance reduction is negative.

A.5 Triangle 15

For step 1, the misfit is relative large, but the variance reduction is positive. For step 2, only 15 mHz can not be fitted, the misfit is acceptable. For step 3, the misfit is 0.72 but the variance reduction is a small negative number.

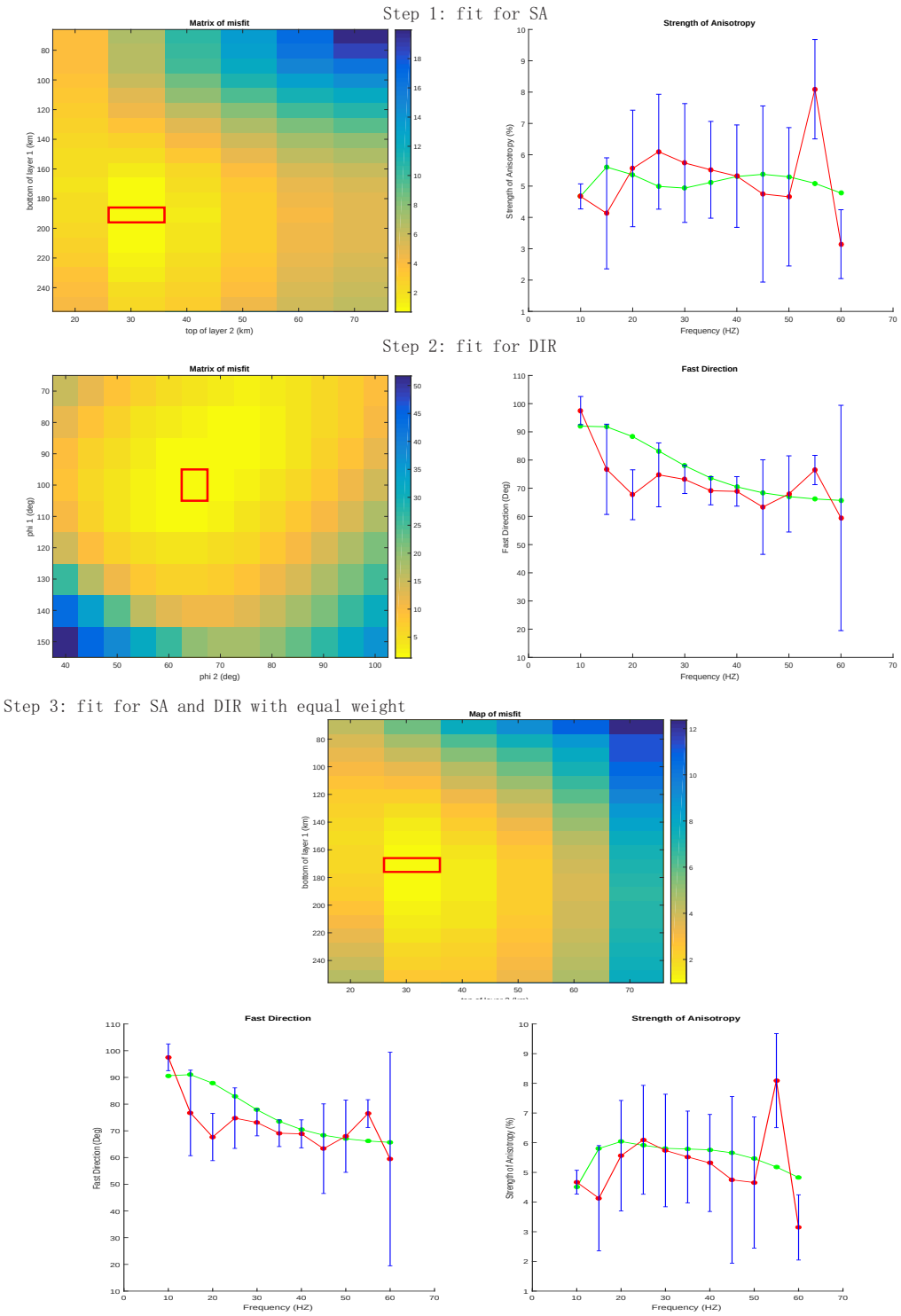

Figure A.1: Triangle 1: misfit matrices and fit plots.

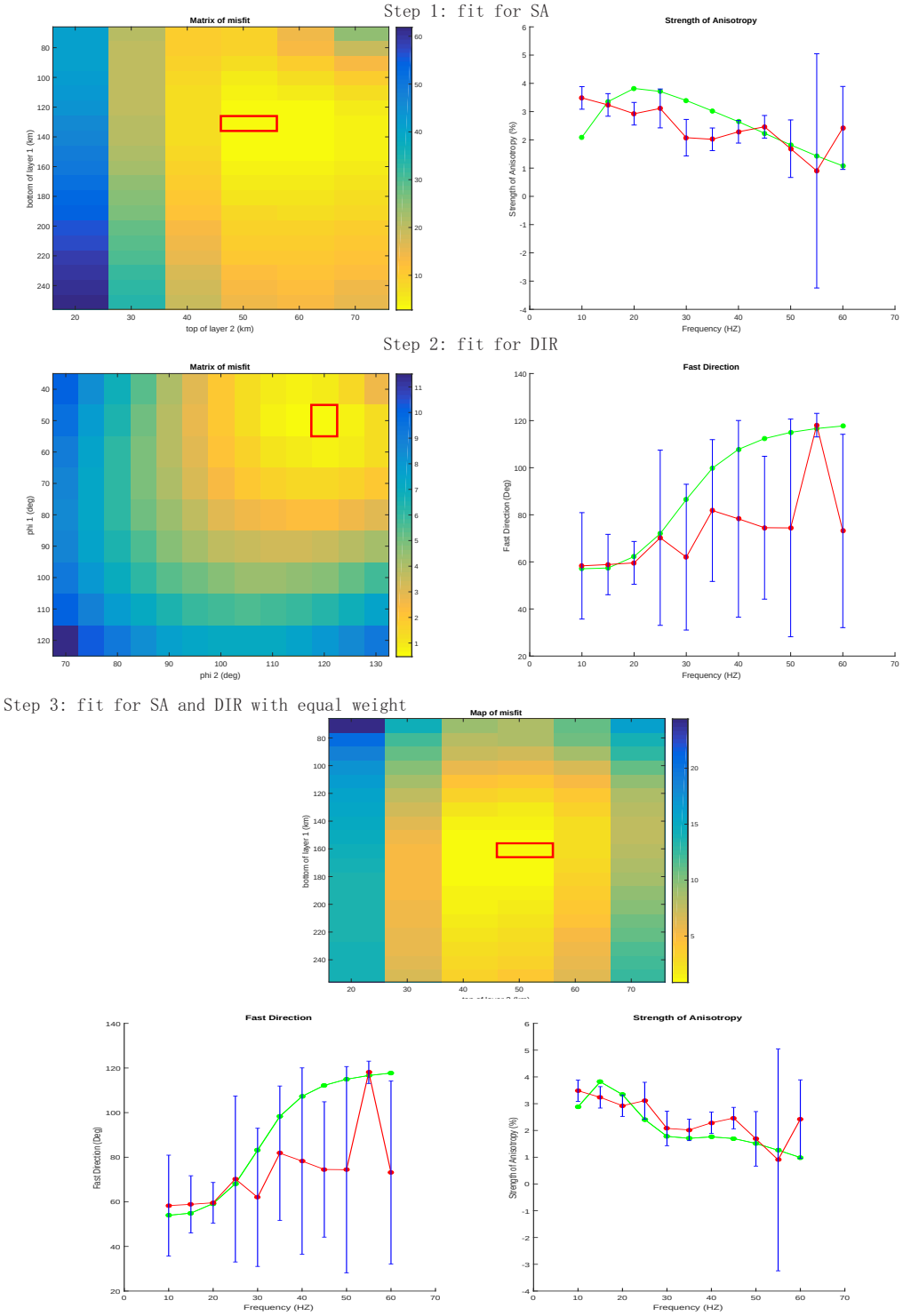

Figure A.2: Triangle 3: misfit matrices and fit plots.

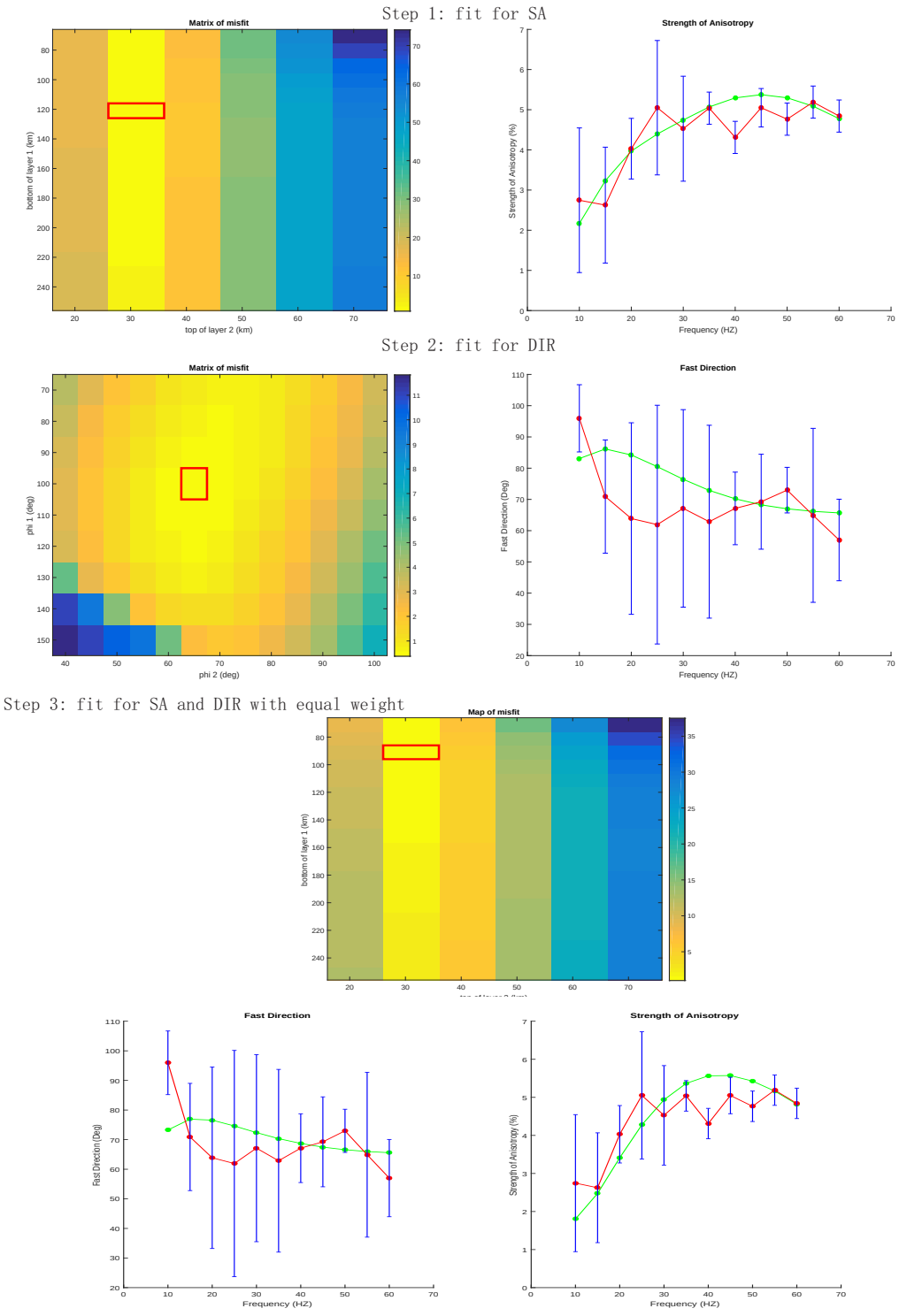

Figure A.3: Triangle 6: misfit matrices and fit plots.

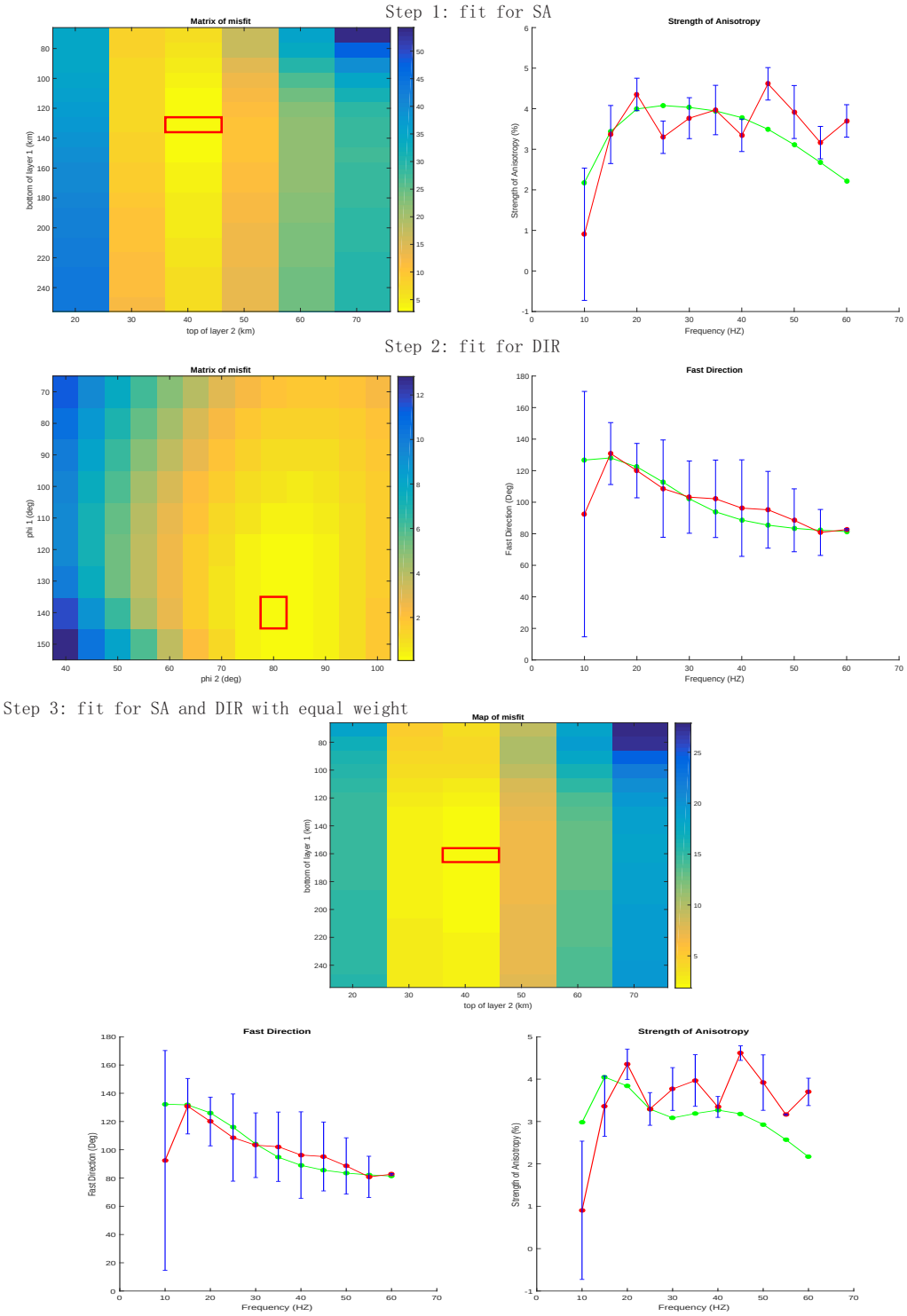

Figure A.4: Triangle 11: misfit matrices and fit plots.

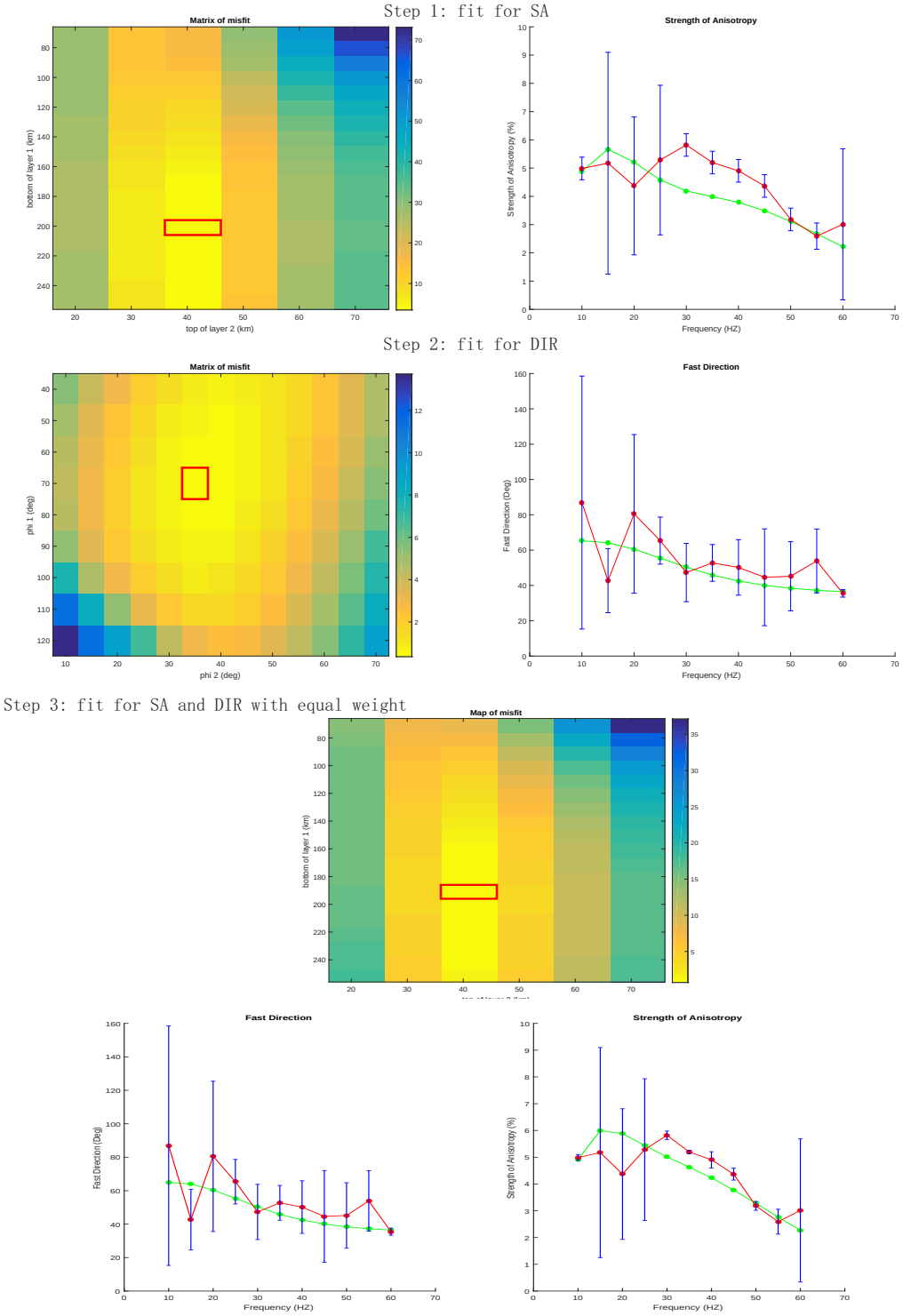

Figure A.5: Triangle 15: misfit matrices and fit plots.